

CHAPTER 1

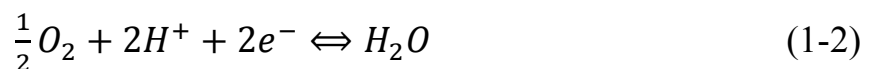
INTRODUCTION

1.1 Overview

Jules Verne, regarded as Father of science fiction, said “I believe that water will one day be employed as fuel that hydrogen and oxygen will furnish as inexhaustible source of heat and light”. Fuel Cells with hydrogen as the anode fuel have immense promise as a future power system because of its high efficiency and low level of pollutant generation, hence they show the distinguishing characteristics that are highly efficient for consumer electronic devices and transportation and stationary applications, which are commonly using heat engine. Therefore, fuel cells are expected to be the most widely applied energy conversion devices in the near future.

Fuel cells are electrochemical devices that convert the chemical energy of their reactants directly to electricity and heat without combustion process. They also behave like the green generator that continues to generate electricity as long as fuel is kept supplying. That’s the difference between fuel cells and batteries.

In a fuel cell, the hydrogen reaction is split into two electrochemical half reactions:



By spatially separating these reactions, the electrons transferred from the fuel are forced to flow through an external circuit and do the useful work before they can complete the reaction. Eventually, the hydrogen and oxygen are

recombined, and an electric current is being produced.

1.2 Fuel Cell Types

There are five major types of fuel cells (Fig. 1.1), which are listed as follows. Their differences are mainly from the electrolytes used.

1. Solid Oxide Fuel Cell (SOFC)
2. Molten Carbonate Fuel Cell (MCFC)
3. Phosphoric Acid Fuel Cell (PAFC)
4. Alkaline Fuel Cell (AFC)
5. Proton Exchange Membrane Fuel Cell (PEMFC)

While all five fuel cell types are based upon the same underlying electrochemical principles, however, they operate at different temperature regimes, incorporate different materials, and often differ in terms of their fuel tolerance and performance characteristics. These are summarized in Table 1.1.

1.2.1 SOFC

Solid oxide fuel cell (SOFC) is a complete solid-state device that uses an oxide ion-conducting ceramic material as the electrolyte, and includes a lanthanum manganate cathode and a nickel zirconia anode. SOFC works in the temperature region of 800 to 1100°C, indicating that high reaction rates can be achieved without expensive catalysts, and that gas, such as natural gas and “internally reformed” one within the fuel cell, can be used directly without a need for a separate unit. Such type of fuel cell addresses all the problems and takes full advantage of the inherent simplicity of the fuel cell concept. Therefore, it is a promising option for high-powered applications, such as industrial uses or

central electricity generating stations.

Planar SOFC systems have received much attention lately because of ease of manufacturing and higher performance as compared to tubular types. Planar SOFC is generally manufactured in three different configurations according to their operating temperatures. For optimal design and operation of a SOFC, a fundamental and detailed understanding of transport and electrochemical kinetics is indispensable. Efforts are presently underway to understand the multiphysics and obtain the optimal design for SOFC.

1.2.2 MCFC

The electrolyte of the molten carbonate fuel cell (MCFC) is a binary molten mixture of lithium and potassium, or lithium and sodium carbonates. It has the potential to be fueled with coal-derived fuel gases or natural gas. Unlike the others, carbon dioxide must be supplied to the cathode, and thus converted to carbonate ions. The high temperature achieves a good reaction rate by using a comparatively inexpensive catalyst-nickel. Therefore, MCFC is also a high-temperature fuel cell like SOFC.

1.2.3 PAFC

The phosphoric acid fuel cell (PAFC) uses a phosphoric acid as an electrolyte to conduct proton which like Nafion membrane in the PEMFC. In the PAFC, the electrochemical reactions take place on highly dispersed electro-catalyst particles supported on carbon black. Phosphoric acid is the inorganic acid that has high thermal, chemical and electrochemical stability. It also contains high volatility (above 150°C) to be adopted as an electrolyte for fuel cells. Due to its low freezing point (42°C) of the pure phosphoric acid, PAFC is

usually maintained above such temperature. Unlike PEMFC, the operating temperature of PAFC is normally around 180 to 200°C, and it has a greater tolerance of CO (up to 1%). PAFC is the first fuel cell for commercial production and enjoys widespread terrestrial use.

1.2.4 AFC

The electrolyte of alkaline fuel cell (AFC) is an alkaline solution, such as potassium hydroxide, and is operated at about 200°C. It is used by NASA on space craft, and is now searching for applications in hydrogen-powered vehicles.

1.2.5 PEMFC

The proton exchange membrane fuel cell (PEMFC) capitalizes on the essential simplicity of fuel cell. The electrolyte is an ion conduction polymer to move H^+ ion passing through the supporting ionomer structure. PEMFC appears to be more adaptable to automobile use than PAFC. It works at low temperature that can start quickly. The thinness of the membrane electrode assembly (MEA) makes the design compact and without corrosive fluid in the fuel cell. Such fuel cell is the best candidate for light-duty vehicles, buildings, and much smaller applications. It is also highly attractive as power sources for mobile applications and portable electronic devices. A very desirable solution to the hydrogen supply problem is to use methanol as a fuel instead, this kind of cell is called direct methanol fuel cell (DMFC). It also uses a polymer membrane as an electrolyte. Unfortunately, this cell performs very low power.

The dissertation interests in state-of-the-art PEMFC science and technology due to its simple structure, which can operate at relatively low temperature, widely practicability and high efficiency.

1.3 PEMFC Fundamentals

1.3.1 Basic Structures

The power generated by PEMFC is affected by the reaction areas, where the gas reactants, electrode, and electrolyte meet together. Hydrogen fuel is fed into the one side (anode electrode), while the other side (cathode electrode) is provisioned with oxygen gas. The electrodes are generally highly porous to increase the reaction surface area further and ensure good gas access. A thin electrolyte layer spatially separates the hydrogen electrode from oxygen one, and ensures that the two individual half reactions occurs independently from one another. The polymer electrolytes operate at low temperature such that PEMFC can start quickly.

Figure 1.2 shows a schematic configuration of a typical PEMFC. The key component of the fuel cell is MEA, which is sandwiched between the anode and cathode electrodes.

When hydrogen gas is fed into anode, it reacts with a catalyst to form protons (H^+) and electrons. The electrolyte membrane is an ion conductor so it can allow the protons to pass across the electrolyte membrane to reach the cathode, but not the electrons. Instead, the electrons are forced to travel through an external circuit, where they can generate useful power before recombining with the protons and oxygen gas at the cathode to form water.

1.3.2 Thermodynamics

Fuel cell is more efficient than heat engines because they directly convert chemical energy to electrical one. Carnot cycle shows the possibly maximum efficiency of a heat engine as:

$$\eta = \frac{T_H - T_L}{T_H} \quad (1-3)$$

where T_H is the highest temperature and T_L is the rejection temperature of the heat engine, respectively. The Carnot efficiency limit for a typical heat engine that operates at 675K and rejects heat at 325K is 52%.

The ideal efficiency of a fuel cell is given by a ratio of the thermodynamically extractable energy of the reaction to the total heat energy that would have been released by the reaction in combustion:

$$\eta = \frac{\Delta G}{\Delta H} \quad (1-4)$$

At standard conditions, ΔH^0 for the hydrogen/oxygen reaction is -285.83 KJ/mole and the ΔG^0 is -237.14 KJ/mole that give a theoretical efficiency limit of 83%.

Although ΔG^0 represents the energy potential that can be extracted by a fuel cell at standard condition, in a fuel cell this energy is expressed as an electrical potential, or voltage (E_0):

$$E_0 = \frac{\Delta G^0}{2F} \quad (1-5)$$

At standard conditions, it is 1.23 V, referred as the fuel cell open circuit voltage (OCV). ΔG is a function of temperature and pressure, therefore, the fuel cell open circuit voltage depends on the operating conditions. The dependencies are described by the Nernst equation as:

$$E_{Nernst} = E_0 + \frac{RT}{2F} \ln \frac{P_{H_2} P_{O_2}^{\frac{1}{2}}}{P_{H_2O}} \quad (1-6)$$

Figure 1.3 shows the dependence of ideal fuel cell voltage on temperature. The ideal fuel cell voltage decreases with increasing temperature, but usually the opposite is true for the actual fuel cell efficiency due to accelerated electrochemical reaction kinetics at higher temperatures. In particular, the initial

fall in voltage as current is drawn from the cell is a markedly loss.

1.3.3 Kinetics

An ideal fuel cell would supply an infinite current while maintaining the constant voltage determined by the Nernst equation. But in fact, the actual voltage output of a real fuel cell is less than the ideal thermodynamically predicted voltage. Furthermore, the more current is drawn from a real fuel cell, the more the voltage output of the cell declines, limiting the total power that the fuel cell can deliver. The performance of a real fuel cell device can be summarized into a graph by showing its current versus voltage characteristics. This graph, called a polarization curve, shows the real voltage output of the fuel cell under a given current output. An example of a typical polarization curve is illustrated in Fig. 1.4.

Note that the current has been normalized by the area of the fuel cell (this gives a current density, mA/cm²). Because a larger area fuel cell can produce more electricity than that of a smaller area fuel cell, the polarization curves are normalized by fuel cell area to make results comparable.

The voltage output of a real fuel cell is less than the thermodynamically predicted voltage output due to irreversible kinetic losses. The more current is drawn from the cell, the greater these losses.

There are three major types of fuel cell losses, which appear in the different regions along a fuel cell polarization curve, and they are:

1. Activation losses
2. Ohmic losses
3. Concentration losses

An equation for the true fuel cell polarization behavior can thus be written

by starting with the thermodynamically predicted voltage output of the fuel cell and then subtracting off the various loss terms:

$$E_{real} = E_{Nernst} - \eta_{act} - IR - \eta_{conc} \quad (1-7)$$

These three categories of irreversibility are described one by one in the following sections.

1.3.3.1 Activation Losses

At low current density, the voltage of a fuel cell drops rapidly, because the sluggishness of the electrochemical half reactions occurs at the anode and cathode electrodes. The oxygen reduction reaction at cathode is especially sluggish, accounting for the most of activation losses. Although the final state of produced water is lower in energy than that of the initial reactants, an energy barrier impedes the conversion of reactants into products. A portion of fuel cell voltage is sacrificed to lower this barrier and thus increases the rate at which reactants are converted into product, allowing the fuel cell to output more current. The relationship between the applied activation overvoltage and current density output shows an exponential form in nature, and can be described by the Butler-Volmer equation, such as:

$$i = i_0 \left(\frac{C_O}{C_O^*} e^{-\frac{\alpha F \eta_{act}}{RT}} - \frac{C_R}{C_R^*} e^{-\frac{(1-\alpha) F \eta_{act}}{RT}} \right) \quad (1-8)$$

when the overvoltage is greater than 50 mV, the Butler-Volmer equation can be approximated by a much simpler form called the Tafel equation:

$$\eta_{act} = \frac{RT}{\alpha F} \ln \frac{i}{i_0} \quad (1-9)$$

Activation losses can be minimized by maximizing the exchange current density, a function of the catalyst material and the total reaction surface area. As mentioned earlier, the electrodes are highly porous such that it can maximize the

total reaction surface area. Highly dispersing, nano-scale particles of platinum (Pt) are mixed into the porous electrode so that they are in intimate contact with the gas phase pores, the electrically conductive electrode and ion conductive electrolyte. This can enlarge the amount of triple phase boundary, thus maximizing the exchange current density. Platinum is currently the best known catalyst for PEMFC.

1.3.3.2 Ohmic Losses

Ohmic losses arise due to the internal resistance of the materials in fuel cell to the flow of electrons and protons. These losses are called “Ohmic losses” because they generally follow Ohms law, $V=IR$. Both the electrically conductive electrodes and ion conductive electrolyte contribute to the resistance losses. Usually, ionic resistance is dominant in a well-designed fuel cell. The linear drop in the middle of the polarization curve in Fig. 1.4 distinctly manifests the Ohmic loss effects. In fuel cell systems, most of the Ohmic loss arises from the electrolyte.

1.3.3.3 Concentration Losses

At high current density, the voltage output of fuel cell once again drops rapidly, declining quickly to zero. The current density output at zero voltage is known as the short-circuit current, and represents the maximum current that can be produced by fuel cell. However, at this current level, the voltage output of the fuel cell is zero, consequently, the total power delivered by the fuel cell is also zero. Therefore, power peaks appear somewhere in the middle of polarization curve. The reason for the final steep decline in fuel cell voltage at high current density is due to mass transport limitations. At a high current density, the fuel or

oxidant gases are consumed faster on the reaction surfaces than that they can be replenished. At a certain limiting current density, the partial pressures of the reactant gases at the reaction surfaces plummet towards zero. From the Nernst equation, it is clear that this dramatic decline in the partial pressures of reactants causes a dramatic decline in output voltage. The voltage drop from this mass transportation limit is:

$$\eta_{conc} = A \ln \left(1 - \frac{i}{i_l} \right) , \quad (1-10)$$

where A is a fitting parameter (V). It is obvious that the concentration loss is dominant at high current density. Well-designed flow structures and thin, highly porous electrodes may reduce the concentration overvoltage.

The concentration overvoltage is particularly important in cases where the hydrogen is supplied from some kind of reformer, as there might be a difficulty in increasing the rate of supply of hydrogen quickly to respond to demand. Another important case is at the air cathode, if the air supply is not well circulated. A particular problem is that the nitrogen that is left behind after the oxygen is consumed can cause a mass transport problem at high current density- it effectively blocks the oxygen supply. In PEMFCs, the removal of water can also be a cause of concentration overvoltage.

1.4 Literature Survey

1.4.1 CO Poison of PEMFC

The best performance is realized in a PEMFC when the anode fuel is pure hydrogen and the cathode fuel is pure oxygen. However, directly storing hydrogen is difficult, so hydrocarbon fuels, such as methanol and methane, are adopted to pass through a fuel reformer to generate hydrogen. However, they

also produce undesired pollutants, such as carbon monoxide (CO), carbon dioxide (CO₂), and so on. The active adsorption of CO by the catalyst will cause the Tafel reaction to become the rate determining step, so it critically affects the cell performance; this phenomenon is referred as CO poisoning. In order to overcome the CO poisoning problem, many theoretical and experimental studies have addressed for the improvement of PEMFC CO tolerance. Various investigators have suggested techniques to reduce the effect of CO poisoning. These include increasing the ability to catalyze CO oxidation, weakening the adsorption of CO by these catalysts, adding an oxidant to the anode fuel stream to allow CO oxidation, increasing the anode potential to oxidize CO, and changing the thermodynamic operating conditions. The most effective solution is to use alloy catalysts. This method is to add a second or third precious metal to Pt catalyst to form a new alloy to improve CO tolerance. Pt-Ru alloy is the most frequently used in a PEMFC catalyst in commercial fuel cells because Pt-Ru catalyst increases CO tolerance. Some investigations have elucidated the mechanism of the CO reaction on the Pt-Ru catalyst.

Watanabe and Motoo [1] used the Ruthenium (Ru) surface to form Ru-OH to oxidize CO, which was adsorbed on the catalyst to form CO₂. CO is removed from the surface of the catalyst, whose reaction area thus increases and improves cell performance. Ru can promote the oxidation of CO, and so the Pt-Ru catalyst improves CO tolerance. Dhar *et al.* [2] experimentally studied the effect of CO poisoning on cell performance. They found that when the cell uses dispersed Pt as an anode catalyst, as little as 10 ppm CO in the anode fuel stream can halve the power. Hence, the problem of CO poisoning must be solved. Gastiger *et al.* [3] showed that the optimum ratio of Pt to Ru is 1:1. Oetjen *et al.* [4] evaluated the performance of PEMFC with Pt, Pt_{0.7}Ru_{0.3}, and Pt_{0.5}Ru_{0.5} anode

catalysts at 80°C in pure H₂ and H₂ containing CO between 25 ppm and 250 ppm. A significant improvement in the CO tolerance is observed for dispersed Pt-Ru anode catalysts compare to pure Pt. A Pt_{0.5}Ru_{0.5} anode catalyst showed the best performance in H₂/CO. Watanabe *et al.* [5] determined the power of Pt-Ru catalyst to adsorb CO. Pt-Ru increases CO tolerance in two ways. Ru-OH can oxidize CO, and Ru can reduce the ability of Pt to adsorb CO. These two effects occur simultaneously. Christoffersen *et al.* [6] used “density functional theory” to calculate the surface characteristics of every dual metal catalyst and their corresponding CO adsorptive powers. They considered that Ru of Pt-Ru adsorbs CO onto the surface of the catalyst, reducing the ability of Pt to absorb CO. Therefore, Ru can reduce the effect of CO poisoning. Yu *et al.* [7] studied the effect of CO on the performance of PEMFC. The results showed that the thin-film catalyst layer made by transfer method exhibits high electro-catalyst utilization and low CO tolerance with the same electro-catalyst, while it is different from the traditional method. The thin-film catalyst layer prepares the inner catalyst layer should be rich in Pt and the outer catalyst layer should be rich in Pt-Ru/C to tolerate CO. Papageorgopoulos *et al.* [8] prepared Pt-Ru (1:1)/C catalysts to against CO poison of PEMFC. The CV experiments indicated CO to be oxidized on Ru. The results showed an evident enhancement in the ability of the anode to tolerate CO above 100 ppm. Santiago *et al.* [9] investigated gas diffusion electrodes dispersed Pt/C, Pt-Ru/C and Pt-Mo/C. The results observed a significant decrease of the electro-catalyst activity based on Pt-Mo/C in the presence of CO₂, and this is associated to an increase of the CO concentration resulting from the occurrence of the reverse water gas shift reaction. Ham *et al.* [10] demonstrated that Pt supported on meso-porous tungsten carbide (WC phase) was an effective CO-tolerant electro-anode catalyst for hydrogen oxidation. A

Pt/nano-porous WC catalyst showed two-fold higher mass activity and much improved resistance to CO poisoning for hydrogen electro-oxidation compared to a commercial Pt/C catalyst.

Without adding a second or third precious metal, CO tolerance can also be improved by feeding oxidant into the anode. The bleeding oxidant can be air, oxygen or hydrogen peroxide. The methods for removing CO from the fuel cell are to feed the fuel with a small amount of air or oxygen (“air bleeding”). There are some literatures that study bleeding oxidant.

Gottesfeld and Pafford [11] injected a small amount of oxygen along with the fuel stream which was established in the late 1980s at Los Alamos. They found that the deleterious effect of 100 ppm CO could be completely eliminated by injecting a small amount of O₂ (2%). Rohland and Plzak [12] prepared several oxide Au-catalyst powders by co-precipitation and filled these powders into a Ni-foam-sheet by cold-pressing at 1 t/cm². They determined the selective CO oxidation rate in H₂ plus 1% O₂ at 80°C in an external reactor for differential flow. The results showed that the PEMFC tolerates 100-150 ppm CO at 5% air content in H₂ and 50 ppm CO at 1% air content. Without air content in H₂, the PEMFC tolerates no more than 30 ppm CO. Gubler *et al.* [13] showed that if Pt-Ru is used as anode catalyst, 1% of oxygen is sufficient to achieve full performance recovery, using H₂/100 ppm CO as fuel, whereas 2% O₂ is required using pure Pt. Haug *et al.* [14] worked a layer of carbon-supported Ru is placed between the Pt catalyst and the anode flow field to form a filter. The results showed that an anode feeds stream consisted of reformat (containing 50 ppm CO) and 1-2% oxygen, the Pt-Ru filter electrode performs better CO tolerance than the Pt-Ru alloy catalyst. The Pt-Ru filter anode with 2 vol% oxygen showed superior performance and CO concentration tolerance improved to 100 ppm.

Haug *et al.* [15] developed the sputter-deposited Ru filters on the anode catalyst layer. The results achieved twice the CO tolerance of the previous work under similar operating conditions. Murthy *et al.* [16] examined the effect of thermodynamic factors on CO tolerance. They used commercial MEA to perform test and changed the cell operation temperature and backpressure. Raising the cell temperature from 70 to 90°C might increase CO tolerance because the adsorption depended on temperature. Increasing the backpressure from 101 kPa to 202 kPa might have increased the permeability toward oxygen. When oxygen arrived at the anode side, CO was oxidized and cell performance improved. Transient measurements demonstrated that the poisoning rates fell by a factor of 4 as the pressure increased and by a factor of 14 as the temperature increased. Baschuk and Li [17] presented a mathematical model of a PEMFC that simulates CO poisoning and oxygen bleeding. The model considered the adsorption, desorption and electro-oxidation of CO and H₂ by the reactant-pair and Tefel-Volmer mechanism, respectively. Oxygen bleeding is modeled by the heterogeneous oxidation of CO and H₂ through a Langmuir-Hinshelwood mechanism. The results showed that CO poisoning is influenced by the relative concentration of H₂ to CO. Increasing temperature and pressure mitigate CO poisoning. The coverage of CO decreases at higher temperature due to an increased rate of CO desorption and a small amount of electro-oxidation. Increase in pressure improves the H₂ concentration more than the CO concentration. Feeding 2% oxygen allows for a significant performance recovery even though 100 ppm CO. Lee *et al.* [18] described a technique for analyzing data from the poisoning and recovery processes in a fuel cell exposed to transient CO concentrations. The technique, the “First Order Plus Dead Time” model, described the transient PEMFC responses to CO better than a value for the

slope. The technique is illustrated for the transient behavior of the fuel cell in the presence of 3000 ppm CO, with and without air-bleed (15% air-bleed). The results showed that the time constant for the poisoning process is extended from 4-48 s when 15% air is injected with an anode stream of 3000 ppm CO/H₂. For the recovery process, a 15% air-bleed reduces the dead time from 122-36 s and the time constant from 89-18 s. In addition, the gain is shown to be relatively independent of the high CO concentrations but it is affected by air bleeding. In order to enhance the efficiency of the oxygen, Uribe *et al.* [19] placed a composite film containing inexpensive materials onto the gas diffusion layer (GDL) and these materials were able to catalyze the oxidation of CO with O₂ to CO₂. Shi *et al.* [20] reported that a PEMFC with a novel diffusion layer exhibited better performance than a traditional cell for a feed gas containing 100 ppm CO/H₂ and 2% air. The results revealed that Au particles in the diffusion layer were active in the water gas shift reaction at low temperature. Chu *et al.* [21] used air bleeding to overcome CO poisoning and applied the technique in a PEMFC stack.

1.4.2 Micro PEMFC

In recent years, the size of fuel cells has been minimized. They have been adopted in portable electronic products, such as cellular phones and PDAs. The increasing demands for a portable and efficient electrical power supply leads to the development of micro fuel cell technology. Conventional fuel cells are manufactured using traditional Computer Numeric Control (CNC) technology, whereas micro fuel cells are fabricated using micro-electro-mechanical-systems (MEMS) technology. The potential applications of micro fuel cells have increased significantly since 2000, driven by a well-defined need of the consumer

electronics industry for micro PEMFCs that outperform secondary Lithium batteries [22].

Early in 2000, Lee *et al.* [23] applied micro fabrication techniques, such as deep silicon etching, photo-masked electroplating, physical vapor deposition, anodic bonding, and spin coating to silicon wafers to create flow channels. They produced milliwatt fuel cells using novel techniques and materials. Their micro fuel cells have an efficiency performance of 150 mA/cm². Kelley *et al.* [24] described a design for a miniaturized (active area, 0.25 cm²) methanol/air polymer electrolyte fuel cell. The electrodes for the micro PEMFC are constructed via standard MEMS and microelectronic fabrication techniques using silicon substrates. The design successfully miniaturizes a methanol/air PEMFC. The same procedures for fabrication can be used with little change to further miniaturize the system by up to three orders of magnitude.

Meyers and Maynard [25] miniaturized PEMFC for powering 0.5-20 W portable telecommunication and computing devices. Their design is implemented on a silicon substrate to take advantage of advanced silicon processing technology in order to minimize production costs. They also employ a mathematical model to quantify the effects of the secondary current distribution on two competing cell designs. The results solved some issues to optimizing the fuel cell stack operating performance. Muller *et al.* [26] investigated the miniaturization of the macroscopic flow fields in fuel cells in order to achieve higher energy densities. Three concepts of fuel cells with micro-structured flow fields were presented, amongst them one complete fuel cell system for the use in portable applications. Since different packaging and assembly techniques with flexible materials are being used, the form of the cell can be tailored for specific applications. The results showed that a stack of cells can be very flat resulting

in power densities as high as 1 W/cm^2 . O'Hayre *et al.* [27] used printed circuit board (PCB) technology to construct a portable hydrogen/oxygen fuel cell power sources. They explored several novel flow structure and gas routing designs. They demonstrated the fuel cell device voltages ranging from 1 V single cell to 16 V planar arrays with power output ranging from lower 1 W to higher 200 W. The lightweight laminate PCB technology allows the best prototypes to achieve higher 700 mW/cm^2 area power density and higher 400 mW/cm^3 volumetric power density. The results showed that the power of PCB-FC will be up around to 1 KW in the near future.

Hahn *et al.* [28] developed a planar PEMFC with a cross sectional area between 1 mm^2 and 1 cm^2 at the silicon wafer level. They analyzed various patterning technologies to fabricate micro flow fields, and achieved a power density of 80 mW/cm^2 during long-term operation. Yohtaro [29] applied micro fabrication technology to preparation processes for micro fuel cells. He showed that micro PEMFCs had higher output power than micro DMFCs. Hsieh *et al.* [30] developed a novel design and fabrication process for a micro fuel cell flow field plate with a cross sectional area of 5 cm^2 and thickness of $800 \mu\text{m}$. Their novel design had a power density of 25 mW/cm^2 at 0.65 V, and a reliable and stable output power at ambient temperature. Schmitz *et al.* [31] used PCB technology to make planar PEMFC. The planar PEMFC design consists of an open cathode side which allows a completely passive, self-breathing operation of the fuel cell. The performance achieved 100 mW/cm^2 at 500 mV with hydrogen as an anode fuel. Lu *et al.* [32] developed a silicon-based micro DMFC for portable applications and carried out its electrochemical. Anode and cathode flow fields with channel and rib width of $750 \mu\text{m}$ and channel depth of $400 \mu\text{m}$ are fabricated on Silicon wafers using the MEMS technology. The cell with the

active area of 1.625 cm^2 is assembled by sandwiching the MEA between two micro-fabricated Silicon wafers. Extensive cell polarization testing demonstrated a maximum power density of 50 mW/cm^2 using 2 M methanol feed at 60°C . When the cell is operated at room temperature, the maximum power density is shown to 16 mW/cm^2 with both 2 M and 4 M methanol be fed. Cha *et al.* [33] developed a novel design and the fabrication processes for micro DMFC. The MEA consists of two identical polymer chips positioned on both sides of the proton exchange membrane, which play the roles of current collector, fuel diffusion layer, and catalyst supporter. Each chip has $300 \mu\text{m}$ through holes for catalyst supporter and $400 \mu\text{m}$ through holes for fuel diffusion layer. The results showed the maximum power density of polymer micro DMFC is 8 mW/cm^2 . Luharuka *et al.* [34] presented the fuel delivery system for micro fuel cells and other micro fluidic devices. They provided a zero power solution for fuel storage and delivery. The results showed that these pumps can be used in micro fluidic devices to pump fluid continuously at near constant design pressure.

Hsieh *et al.* [35] used the SU-8 photoresist micro fabrication process to fabricate micro PEMFC flow structures. The polarization curve of performance shows a modest voltage drop over a very small range of currents. Their work contributed to the low-cost mass-production of small flat single fuel cells with a power density of 30 mW/cm^2 at 0.35 V. Chan *et al.* [36] developed a micro fuel cell using polymeric micromachining. The MEA was embedded in a gold-coated polymethyl methacrylate substrate. The operating conditions included dead-ending of hydrogen in the anode. The results revealed that the power output by the 3 cm^2 fuel cell was 0.947 W when pure hydrogen was fed to the anode and pure oxygen was supplied to the cathode at room temperature. When air was utilized on the cathode side, the power output reached 0.246 W.

The design of the base substrate and electrodes performed well. Hydrogen was set to be dead-ended; thus, the utilization of hydrogen was nearly 100%. Lu and Wang [37] fabricated a silicon-based micro DMFC. The cell with the active area of 1.625 cm^2 has a maximum power density of 50 mW/cm^2 at 60°C . Since silicon wafer is too fragile to compress for sealing, and a thicker layer of gold has to be coated on the silicon wafer to reduce contact resistance, further development of micro DMFCs for high power application is carried out using stainless steel plate as bipolar plate in which flow channels are fabricated by photochemical etching technology. The maximum power density of the micro DMFC with stainless steel reaches 62.5 mW/cm^2 at 40°C and 62.5 mW/cm^2 at 60°C with atmospheric pressure. An 8-cell air-breathing DMFC stack is developed. The DMFC stack produces a maximum output power of 1.33 W at 2.21 V at room temperature, corresponding to a power density of 33.3 mW/cm^2 . A passive DMFC using pure methanol is demonstrated with steady state output power of $20\text{-}25 \text{ mW/cm}^2$ over more than 10 hours without heat management. Aravamudhan *et al.* [38] presented a micro DMFC. They use macro-porous silicon technology to fabricate the electrodes of the fuel cell. The porous silicon structure serves to be a fuel storage reservoir and creates the electrodes and integrates with Nafion[®] 115 membrane to build the micro fuel cell stack. The cell performance tests indicate an open circuit voltage of 260 mV and a maximum power density is 8.1 mW/cm^2 at room temperature with a fuel supply of $5 \mu\text{L}$; 8.5 M ethanol solution. Jayashree *et al.* [39] reported the design, assembly, and performance of an air-breathing laminar flow-based micro fluidic fuel cell. The micro fluidic transport phenomenon of laminar flow can be utilized to create the necessary compartmentalization of the fuel and oxidant streams in a single channel without the need of a physical barrier such as a membrane while still

allowing ionic transport. For a formic acid concentration of 0.1 M, the potential drops sharply at a current density of about 20 mA/cm². The results showed that it is characteristic of a mass transfer limited cell. The best performance is observed for a formic acid concentration of 1 M; a maximum current density of about 130 mA/cm² and a maximum power density of 26 mW/cm².

In 2006, Cha *et al.* [40] studied transport phenomena in micro fuel cell flow channels. The channels were 500 μm, 100 μm and 20 μm wide and constructed using a structural photopolymer. The effects of channel size and the GDL thickness on performance were examined. A large pressure drop in very small channels improved the convection of air into the GDL and improved fuel cell performance at low current densities. The results indicated that using a thin GDL improved micro fuel cell performance. Kim *et al.* [41] investigated the fabrication process and electrochemical characterization of a miniaturized PEMFC with silicon separators. The micro channels on the silicon separator were created by a photolithographic process. The micro channels were 400 μm wide and 230 μm deep. The single cell with these silicon separators had a power density of 203 mW/cm² at 0.6 V, which was similar to that of a conventional non-silicon fuel cell. The results demonstrated that a silicon separator can be applied successfully as an alternative to conventional bipolar plates for a micro PEMFC. Hsieh *et al.* [42] investigated the operational parameters of an H₂/air micro PEMFC with different flow configurations by impedance spectroscopy. Their study considered a range of operating parameters, such as backpressure and cell temperature, to determine how flow configuration affected micro fuel cell performance. Optimal operating conditions were utilized to test the micro PEMFC stack [43]. The results demonstrate that the effects of operational parameters, including magnitude, on

stack performance are similar to those on a single cell. Xiao *et al.* [44], who developed a silicon-based PEMFC power system, indicated that the catalyst with a high active surface area was monolithically integrated with the major fuel cell components using the sputtering method. Yang *et al.* [45] presented a micro diaphragm air pump actuated by PZT bimorphs for air supply for micro fuel cells. The results showed that the diaphragm air pump has high efficiency and good performance. Yao *et al.* [46] described a high power density, silicon-based micro scale DMFC, under development at Carnegie Mellon. The proposed DMFC contains several unique features: a silicon wafer with arrays of etched holes selectively coated with a non-wetting agent for collecting water at the cathode; a silicon membrane micro pump for pumping the collected water back to the anode; and a passive liquid-gas separator for CO₂ removal. All of these silicon-based components are fabricated using MEMS based processes on the same silicon wafer, so that interconnections are eliminated, and integration efforts as well as post-fabrication costs are minimized. The results showed that the DMFC overall size of one cubic inch, produce a net output of 10 mW, and have an energy density three to five times higher than that of current lithium batteries. Ito *et al.* [47] proposed a novel design and fabrication technique for a micro DMFC. Ten μ -DMFCs are fabricated on a polymeric flexible substrate containing a micro-holes array. The results showed that with ten cells in series on the substrate, the voltage achieves an open circuit voltage of 5.6 V and an average cell power density of 3 mW/cm². Lim *et al.* [48] fabricated a DMFC on PCB substrates by means of a photolithography process. The effects of channel pattern, channel width and methanol flow rate on the performance of the fabricated DMFC are evaluated over a range of flow-channel widths from 200 μ m to 400 μ m and flow rates of methanol form 2 ml/min to 80 ml/min. A

micro-DMFC with a cross-stripe channel pattern gives superior performance compared with zigzag and serpentine types of pattern. The results showed that a single cell with a 200 μm wide channel delivers a maximum power density of 33 mW/cm^2 when using 2 M methanol fed at 80°C. An air-breathing multi-DMFC composed of eight single unit cells gives 180 mW/cm^2 by using a methanol reservoir. Nguyen and Chan [49] reported recent progress of the development of micro-machined membrane-based fuel cells. They first discuss the scaling law applied to this type of fuel cell. Impacts of miniaturization on the performance of membrane-based fuel cells are highlighted. Micro PEMFCs and micro DMFCs are considered and the active areas for these cells are less than one square inch. They only focus on the choice of material and the design consideration of the components in the miniature fuel cell. Next, they compare and discuss the performance of different micro fuel cells published recently in the literature. Finally, they give an outlook on possible future development of micro fuel cell research.

In 2007, Lee and Chuang [50] employed porous silicon as a GDL in a micro fuel cell. The Pt catalyst was deposited on the surface and inside, the porous silicon with Pt catalyst replaced the conventional GDL, and the Pt metal remaining on the rib was used to form a micro-thermal sensor in a single lithographic process. Experimental results demonstrated that temperature was almost linearly related to resistance. Feng *et al.* [51] developed a novel method of producing Silicon-based micro fabricated electrodes with high electrochemical active surface area and high catalyst utilization. They showed that the Si-based MEA system exhibited a power density of 23.4 mW/cm^2 . Seyfang *et al.* [52] developed a novel, simplified concept for polymer electrolyte micro fuel cells. For different flow fields, a maximum power density was $\sim 415 \text{ mW}/\text{cm}^2$ at a cell

voltage of 425 mV. Koc and Mahabunphachai [53] studied on conceptual design and feasibility experiments towards development of a novel hybrid manufacturing process to fabricate fuel cell bipolar plates that consists of multi-array micro-channels on a large surface area. The first investigation involves hydro-forming of micro-channels using thin sheet metals of SS304 with a thickness of 51 μm . The width of the channels range from 0.46 mm to 1.33 mm and the height range is between 0.15 mm and 0.98 mm. The second investigation is on the feasibility of mechanical bonding of thin sheet metal blanks. The experimental results from both investigations demonstrated the feasibility of the proposed manufacturing technique for making of the fuel cell bipolar plates. Hsieh and Chu [54] examined the effects of channel and rib widths with an aspect ratio (H/W) of 0.67 of rectangular cross-sections flow field plates on cell performance in terms of VI/PI curves versus flow field pressure drop of a micro PEMFC. A simple lumped capacitance model is used to predict the temperature evolution of the fuel cell system, and results showed this model performs quite well, and the channel-to-rib width ratio seems no significant influence on the fuel cell temperature evolution of the flow field plates.

In recent 2008, Zhang *et al.* [55] developed a novel porous gas diffusion medium with improved thermal and electrical conductivities and controllable porosity fabricated from a metal foil using micro/nano technology in a PEMFC. The performance of the novel GDL was enhanced by applying a microporous layer (MPL) to the GDL, and by enhancing in-plane transport. Renaud *et al.* [56] studied the hydrodynamic flow characteristics in micro fluidic devices. The 2-D model combined with Navier-Stokes equations and the no-slip condition were sufficient to describe and calculate flows in 20 μm deep micro channels etched in silicon; the derived flows were in good agreement with measured flows.

For small dimension of fuel cell, the influence on mass transport or electrical conductivity is significant. Chiang and Chu [57] resulted membrane electrical conductivity increases when the aspect ratio channel is low. Shimpalee and Van Zee [58] investigated how serpentine flow fields with different channel/rib cross-sectional areas affect performance and species distributions for both automotive and stationary conditions. Their simulation results indicated that for a stationary condition, a narrow channel with wide rib spacing improves performance; however, the opposite occurs when the automotive condition is applied. Matamoros and Bruggemann [59] adopted steady and three-dimensional models to determine the influence of geometrical parameters on the performance under different humidity conditions. According to their results, anode and cathode liquid water saturation may affect species transport and the polymer electrolyte water content. Thus, one must simultaneously calculate both water absorption and desorption via the polymer electrolyte and liquid water saturation in anode and cathode porous media to obtain an actual view of ohmic and concentration losses in PEMFC performance.

Shimpalee *et al.* [60] examined different channel path lengths to determine the impact of flow path length on temperature and current density distributions and PEMFC performance. According to their results, local temperature, water content and current density distributions become increasingly uniform under serpentine flow field designs with short path lengths or an increased number of channels. Liu *et al.* [61] developed an isothermal, steady state, three-dimensional multi-component transport model for a PEMFC. Their results revealed detailed distribution characteristics of oxygen concentration, local current density and cathode activation over-potential at different current densities.

1.5 Motivation and Objectives

Clearly, most of the previous papers dealt with PEMFC CO poisoning and micro PEMFC. The objective of this dissertation has two subjects. The first one is the investigation that simulates the fuel of anode from partial oxidation reforming, which produces gases relatively rich in hydrogen, carbon dioxide and carbon monoxide as the most important impurity. It is to define suitable CO poisoning test condition and the best air bleeding replying rate for PEMFC. The experiment observes a change in the current density, while the voltage is fixed at 0.6 V as the specific condition. In this experiment, the anode is fed pure hydrogen in the first 15 min and then H₂-CO mixtures as fuel gases of anode, which contains CO at different concentrations (25 ppm, 52.7 ppm, and 100 ppm). The cell performance is expected to be varied with time. The experimental results will determine which periodic of air bleeding has a better performance in CO poisoning test and find out the difference between these methods. Then, the contaminated polarization curves are determined as soon as the performance subjected to CO poisoning reaches a steady state.

The second subject develops a novel and simple method for manufacturing efficient micro PEMFCs. It focuses to apply MEMS technology on a silicon wafer to manufacture flow channels, and then tests the performance micro fuel cell, defined as the one that generates < 10 W of electricity, under different conditions. Various operational conditions are experimentally utilized to optimize the cell performance. In addition, there were a lot of papers discussed with the PEMFC flow channels configuration or water and thermal issues, but very few of them performed complete computational models for micro PEMFC to concern with its electrochemical phenomena. Therefore, this work not only

applies MEMS technology to manufacture flow channels, but also carries out a series of numerical simulations to validate the corresponding experimental results without considering the two-phase flow effect. The study concentrates on investigating two different stoichiometric flow ratios that affect the polarization curves, current density, water and operational cell temperature in the membrane. This would help a better understanding on the distributions of current density, water and temperature in the micro PEMFC and further to improve its performance.



Table 1.1 A description of the five major fuel cell types

	SOFC	MCFC	PAFC	AFC	PEMFC
Electrolyte	Yttria-stabilised ZrO ₂	Molten salt	Concertrated H ₃ PO ₄ solution (95-98%)	Concertrated KOH solution (35-40 wt%)	Ion exchange membranes
Operating temperature	600~1000°C	650°C	205°C	65~220°C	80°C
Charge carrier	O ²⁻	CO ₃ ²⁻	H ⁺	OH ⁻	H ⁺
Prime cell components	Ceramic	Stainless -based	Graphite -based	Carbon -based	Carbon -based
Catalyst	Perovskites	Nickel	Platinum	Platinum	Platinum
Product water management	Gaseous product	Gaseous product	Evaporative	Evaporative	Evaporative
Product heat management	Internal reforming process gas	Internal reforming process gas	Process gas independent cooling medium	Process gas electrolyte circulation	Process gas independent cooling medium

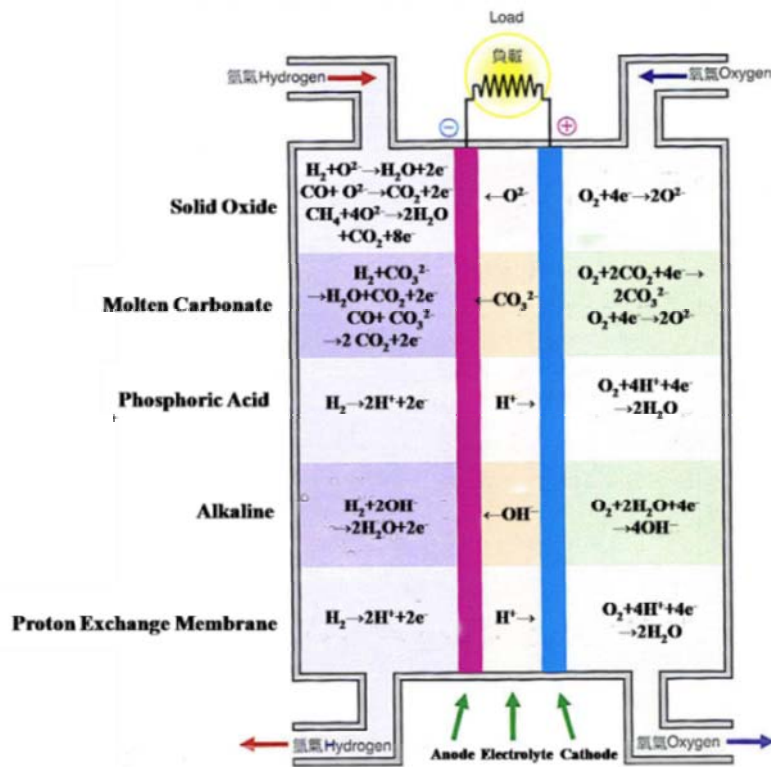


Fig. 1.1 Five major types of fuel cells

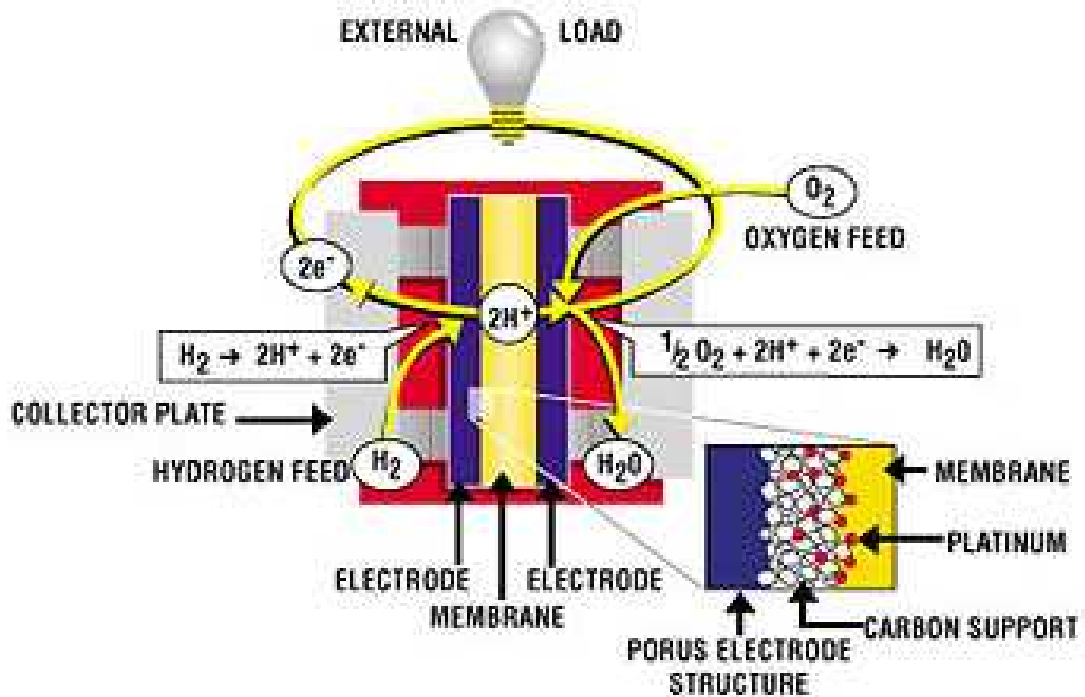


Fig. 1.2 Scheme of a typical PEMFC

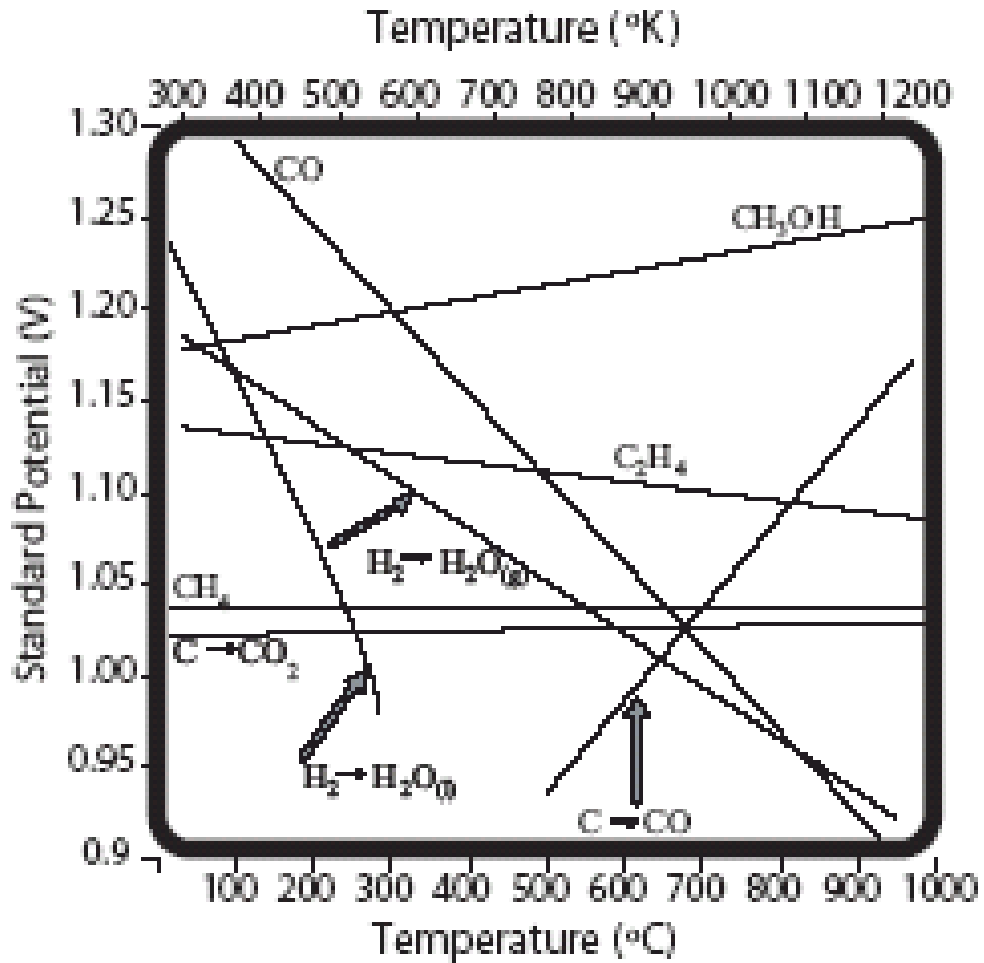


Fig. 1.3 Ideal reversible open circuit potential vs. temperature

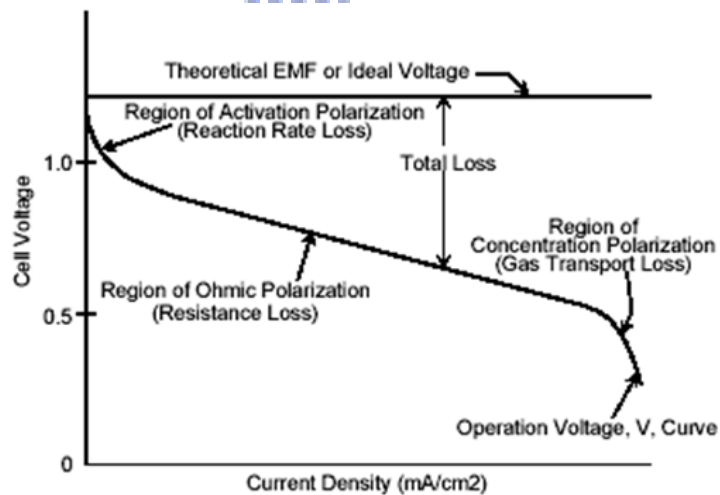


Fig. 1.4 Ideal vs. actual fuel cell polarization curve

CHAPTER 2

EXPERIMENTAL APPARATUSES AND FABRICATION PROCESSES

The effectiveness of a fuel cell requires the performance analysis for both a system as well as its individual components. In this chapter, the apparatuses and the fabrication processes for a typical PEMFC and a micro PEMFC will be introduced in details.

2.1 PEMFC Test Apparatuses Setup

In order to obtain a PEMFC polarization curve, the test apparatus should include an electrical load, MFC readout power supply, power supply, computer, gas pipelines controller, and gas supply unit. Figure 2.1 presents a diagram of a basic experimental apparatus for a fuel cell. This installation can provide the controls for operational conditions, such as temperature, humidification, flow rate, pressure, and cell potential, etc., and it also can evaluate the corresponding performance. The individual components of test station are described as follows.

2.1.1 Electrical Load

The electrical load is a device that simulates loading on an electrical circuit. As a counterpart to a current source, the load is served as a current sink. The load current is regulated electronically. The style of electrical load is HP6060b, whose box is shown in Fig. 2.2 that displays the cell performance on its monitor.

2.1.2 MFC Readout Power Supply

The PC-540 MFC readout power supply (Fig. 2.3) can display and control the units for precision gas control in conjunction with MFCs. This apparatus has multiple channel instrumentation that can completely control up to four MFCs at the same time.

In the present experiment, the flow rate controller operates three flow meters, which comprise anode gas, cathode gas and additional gas meter. These gas meters are for the anode (H_2), cathode (O_2 or air) and bleeding (air) gas, respectively.

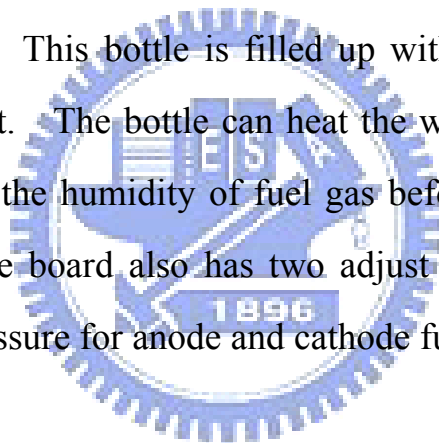
2.1.3 Power Supply and Computer

Power supply is a device that supplies electricity to each component in this experimental test installation (Fig. 2.4). It comprises mass flow controller, solenoid valve, heater (for anode, cathode and cell), and three thermocouples plugs. In this power supply, it has three temperature controllers and monitors. The controllable temperature range is from 25 to 95°C. These temperature controllers operate anode and cathode humidity bottle and cell temperature that can change temperature by the direct input buttons. When press power button, it will start all instruments of test station. On the other hand, pressing power off will shut down all power in the station. Computer regulates all of the test orders, and evaluates experiment results.

2.1.4 Gas Pipelines Controller

The gas pipelines controller (Fig. 2.5) can manage what kind of gas feeding into the anode and cathode fuel stream. It also controls gas humidity, temperature, back pressure and flow rate. There are five gas inlets behind this

apparatus. Both anode and cathode have two gas channels, respectively. The last one is nitrogen channel. The anode channels always are fed with H₂ and reformation gas (H₂/CO) and the cathode channels always fed with O₂ and air. On the operation board, it has anode and cathode globe valve, which can change the gas that test cell needs and can shut down the valve that the gas cannot pass through it into the test sample. In addition, the globe valves have three solenoid valves in the instrumentation which are the safe valves. When this test station is in dangerous or overload condition, the solenoid valves will shut off anode and cathode gas supplies, and then the other valve will open to purge nitrogen into test cell. Before fuel gas enters anode and cathode sides, it must go through humidity bottle first. This bottle is filled up with water and has a heater and thermocouple inside it. The bottle can heat the water when gas passes through the bottle to increase the humidity of fuel gas before fuel and oxidant enter the fuel cell. Finally, the board also has two adjust pressure valves and they can change outlet backpressure for anode and cathode fuel streams, respectively.



2.1.5 Liquid Gas Separator and Gas Supply Unit

After fuel gas passes through test cell, there will have some remnant gas and water discharged from the fuel outlet. If there is too much water in the waste gas channel, it will prevent remnant gas from entering into the atmosphere. Therefore, it must enter a liquid gas separator, where the water can be kept in the bottle and only let the gas go out from the instrument. Then, the waste gas will discharge to the atmosphere by an exhaust fan. Gas supply unit provides fuel gas into the fuel cell.

The photo of complete test station is shown in Fig. 2.6. It shows each apparatus from top to bottom that consists of MFC readout power supply,

electrical load, power output, gas pipelines controller and liquid gas separator, respectively.

2.2 Micro PEMFC Test Apparatuses Setup

In order to obtain a micro PEMFC polarization curve, the micro PEMFC test apparatus also has a gas supply unit, electrical load, power supply, computer, fuel humidifier, fuel temperature controller and mass flow controller. Figure 2.7 shows the experimental setup. The gas supply unit provides the fuel and oxidant into the micro fuel cell. The electrical load is a device that simulates loading on an electrical circuit. Contrary to the current source, the electrical load is a current sink. The load current is regulated electronically. The range of currents measured is 0~15 A and the maximum power output is 75 W. The power supply supplies electricity to each component in this test. A computer regulates all testing orders and evaluates experimental results.

2.3 Test Sample of PEMFC

This section describes the materials used for six major components in the PEMFC. They are MEA, GDL, gasket, flow field plate, current collector, and end plate. The MEA is considered as the “heart” of a PEMFC. It is used to promote ionic conduction. The standard membrane is made of sulfonated poly-tetraflouroethylene (PTFE) produced by DuPont, and it was first used in 1960s by NASA on the space vehicles. The special features of MEA are described as follows. They are high ionic conductivity and low electron conductivity, high stability and low fuel crossover, and high mechanical strength and easy to manufacture. A PRIMEA series 5561 commercial MEA (Fig. 2.8)

from Gore is used in all fuel cell experiments in this study. The membrane has a nominal thickness of 25 μm , and the catalyst loads are 0.45 mg/cm^2 Pt-Ru alloy (1:1) on the anode and 0.6 mg/cm^2 Pt on the cathode, respectively. The geometric active area of the membrane is 25 cm^2 and the cell border area is 100 cm^2 .

GDL is made of porous carbon paper or carbon cloth to provide mechanical strength, gas access, and electric conduction. The GDL (Fig. 2.8) used in the experiment is CARBEL CL GDL and the thickness is of 0.4 mm. Gaskets (Fig. 2.8) with a 25 cm^2 window (fuel cell active area) are used and their thickness is 1 mm.

The flow field plate supplies the reactant gases and removes products. It also electrically connects individual cells in the fuel cell stack. Graphite is used as the material for the flow field plates. A double-channel serpentine (with channel and rib widths of 0.1 cm each and a channel depth of 0.1 cm) is used for both the anode and cathode sites (Fig. 2.9). Serpentine channel is the mostly common-used geometry found in PEMFC prototypes. The anode and cathode flows are con-current.

The current collector (Fig. 2.10) is made of gold-plated copper. The current collector board conducts electricity from the cell. The end plate (Fig. 2.11) is made from nickel-plated steel, used to fix and protect the fuel cell structure. The integrated structural dimension of carbon board, current collector and end plate is 100 mm \times 100 mm \times 52 mm. Eight bolts are fastened into holes on each of the end plates, and the cell is subjected to a torque of 120 $\text{Kg}\cdot\text{cm}$.

Figure 2.12 shows all components of a single PEMFC. There is a sequence to resemble a fuel cell. The MEA is sandwiched between the GDL. In the

outer circle of GDL, it puts a gasket to prevent the gas leakage to environment. This resembling sequence is shown in Fig. 2.13.

2.4 Design and Fabrication of Micro PEMFC

A typical micro PEMFC has an end plate, gasket, GDL, MEA, flow field plate and current collector. The end plate, made of acrylic resin, is 45 mm × 45 mm × 13 mm. The gasket, made of silica gel, is 1 mm thick. This gasket isolates and prevents gas leakage. The 0.4-mm-thick GDL is made of standard carbon paper (CARBEL CL GDL). The MEA, 0.025 mm thick, whose catalyst loads are 0.45 mg/cm² Pt-Ru alloy (1:1) on the anode and 0.6 mg/cm² Pt on the cathode. It is a commercial product from Gore. The micro PEMFC reaction area is 2.5 cm².

A single micro PEMFC is assembled using two flow field plates. Silicon is used for the substrate in the anode and cathode flow field plates. The micro PEMFC is manufactured using MEMS technology. The purpose of silicon wafer etching process is to manufacture the micro PEMFC channels. Photolithography is used to transfer flow channel geometric shapes on a mask onto the surface of a silicon wafer. The steps in the photolithography process are wafer cleaning, deposit silicon nitride, spin coating the resist, soft baking, mask alignment and exposure, development, and hard baking. Figure 2.14 shows the fabrication procedure for the silicon wafer. A silicon wafer of 4 inches in diameter is employed as the substrate in this investigation.

Contaminants on the surface of silicon wafers at the start of the MEMS technology process or accumulated during processing must be removed during processing to obtain high-performance and highly reliable semiconductor devices, and prevent equipment from contamination, especially under high-temperature oxidation, diffusion and deposition tubes. In this study, RCA cleaning (Fig. 2.15), a four-step process, is carried out for removing the organic contaminants,

oxide layer, ions, and heavy metal contaminants from the wafer surface over a 4-inch, (100)-oriented 750- μm -thick silicon wafer.

The wafer is used to dehydration bake approximately 5 mins for dry by an electric hot plate after RCA cleaning. A 200-nm silicon nitride layer is deposited by low-pressure chemical vapor deposition (LPCVD) (Fig. 2.16). One side of the silicon wafer is polished, and the silicon substrate is then spin-coated by a spinner (Fig. 2.17) with a resistive layer of 7 μm thick at various rotating speeds.

The silicon substrate is then soft baked. Soft baking removes most solvents from the photoresist coating. A positive photoresist is then employed. The photoresist is exposed (Fig. 2.18) to ultraviolet (UV) light wherever the underlying material must be removed. The g-line is used during the exposure process in this study. After exposure, heat is applied for approximately 2-3 mins for post-exposure baking. Development is done in the vitrics to form micro flow channels.

The photoresist is then hard-baked for about 1 min. After development, the silicon substrate is examined. The flow structure cavities are patterned by wet etching (Fig. 2.19). Reactive ion etching (RIE) is applied to etch a silicon nitride layer of 300 μm wide. Notably, RIE, an etching technology used during micro fabrication, uses chemically reactive plasma to remove materials deposited on wafers. Plasma is generated under low pressure in an electromagnetic field. However, the silicon nitride layer is too thin for the fuel to flow from the inlet to the outlet. Hence, the exposed silicon wafer is etched into the patterned micro PEMFC channels in an aqueous solution of 45% KOH at 80°C. The depth of etched channel is 500 μm . Such depth promotes gas uniformity, water management and reduced flow resistance. Next, the photoresist is removed from the silicon substrate. The final step employs phosphoric acid to remove the remaining silicon nitride at 180°C. Figure 2.20 plots the fabrication flowchart.

Three serpentine channels, 300 μm wide and 500 μm deep each, are etched

into the sides of the anode and cathode. The fuel holes are drilled into the rear of silicon wafer. The oversize flow field plates are 16 mm × 16 mm. A silicon wafer 4 inches in diameter is used to make four flow field plates. Figure 2.21 shows the silicon substrate after etching.

Current collectors provide an electrical pad for transmission of electricity to the external load. Unlike metal, silicon is not considered as an ideal current collector due to its high electrical resistance. In this investigation, the silicon wafer is only used as a fuel carrier. Therefore, an alternative design in this study uses an MEA and GDL sandwiched between current collectors made of brass foil; this design replaces conventional bipolar plates. Consequently, silicon substrates are rarely used for flow field plates as electrons do not pass through silicon substrates. The advantage of this novel design is that no Au electroplate is required on the top of silicon wafer. The only requirement is that the current collectors be hollowed out to enable fuel to diffuse into the MEA.

In this study, the MEA is sandwiched between two GDLs, two current collectors, two flow field plates, two gaskets and two end plates. The assembled structures are clamped together with four screws. This assembling sequence is shown in Fig. 2.22.

Figure 2.23 (a) presents a schematic diagram of a micro PEMFC. The dimensions of channels are 300 μm wide and 16 mm long, which comprise an effective cell area of 2.5 cm². Figure 2.23 (b) displays the fabricated single micro PEMFC with all components.

2.5 Test Conditions

2.5.1 PEMFC

Before polarization data are collected, the fuel cell has been subjected to a

normal break-in of the MEA and typical polarization experiments. The break-in conditions are as follows. The cell voltage is held at 0.6 V for 24 h. The fuel flow rates, determined from the theoretical volume flow rate that could generate 1 A, for the anode (hydrogen) and cathode (oxygen) are 7.6 cm³/min/A and 3.8 cm³/min/A, respectively. The flow rate for the anode is multiplied by the stoichiometric ratio of 1.37 to yield a value of 10.4 cm³/min/A, whereas that for the cathode it is multiplied by 1.8 to yield 7 cm³/min/A. These flow rates can guarantee the fuel flow rates that are sufficient to initiate the electrochemical reaction. The cathode stoichiometric flow ratio exceeds that of the anode because oxygen is less reactive. The oxidization of hydrogen proceeds so quickly that it causes very low activation over-potential, which is approximately zero. Nevertheless, the reduction of oxygen involves more steps, causing its activation over-potential to exceed that of hydrogen. The cell temperature is held at 65°C and the temperature of the anode and cathode humidifiers is held at 80°C and 70°C, respectively. These temperatures mean that the fuel is sufficiently humid to cross through the membrane, yielding optimum cell performance at the operating temperature of 65°C. The exit pressure of the anode and cathode sides is 1 atm. The MEA performance is used to ensure a clean surface before the exposure experiments.

2.5.2 Micro PEMFC

The micro PEMFC structure cannot be heated because the end plate is made of acrylic resin. Therefore, a humidifier and temperature controller are used to humidify and heat the fuel to improve its performance. The flow rates of hydrogen, oxygen and air are regulated by mass flow controllers. Notably, the flow rate through this mass flow controller cannot be less than 10 cm³/min in the

anode and 20 cm³/min in the cathode. The micro PEMFC is connected to the electrical load. Polarization curves are plotted after the micro PEMFC reaches a steady state. Various fuel temperatures and stoichiometric flow ratios are tested.

2.6 Procedures of the Experimental Operation

2.6.1 PEMFC

1. Connect all electric wires of test station with fuel cell before the experiment. For instance, connect potential sensors to the current collectors, connect positive pole loading line to the cathode current collector. Connect anode with negative pole, insert the heater into the end plate holes, insert the thermocouple into the carbon board holes, and connect pipelines to the fuel cell.
2. Add the water to the humidification bottle by the atmosphere style water bottle.
3. Open the valves of H₂, O₂, N₂, and H₂/CO fuel cylinders and retain the inlet pressure up to 40 psi.
4. Turn on the globe valves of the gas pipelines on the controller operation board, anode side turns to H₂ or H₂/CO pipeline, cathode side turns to O₂ pipeline.
5. Turn on the power source of the exhaust fan. Because this laboratory is in the airtight space and the experimental gases contain CO and H₂, so it is a necessary procedure.
6. Check if any fuel gases leakage from pipeline's connection by applying suds on them. It is a very important procedure, especially for the uses of CO and H₂.
7. Push down the power button of the test station to start apparatus.

8. Activate the software of the test system.
9. Set the minimum fuel flow rate and the flow rate per ampere current of anode and cathode. The minimum flow rates of anode and cathode are $104 \text{ cm}^3/\text{min}$ and $70 \text{ cm}^3/\text{min}$, respectively, and the flow rates per ampere current are $10.4 \text{ cm}^3/\text{min}/\text{A}$ and $7 \text{ cm}^3/\text{min}/\text{A}$, respectively.
10. Set anode and cathode humidification temperature.
11. Push down the gas reset button on the power supply board. At the same time, solenoid valve will shut off N_2 , which stops to purge the fuel cell.
12. Push down the applying fuel icon of software window. The anode and cathode fuel pipeline solenoid valve will open and the fuel gas is fed into fuel cell.
13. Set the cell temperature to heat the fuel cell as humidification. It is to protect MEA from drying to damage the composition.
14. Push down the “apply load” icon of the window that the electrical load will start loading from the test sample as the OCV reaches the steady state value.
15. Set the same cell over-potential to activate the fuel cell. In general, a fuel cell needs to activate several hours until it achieves optimum or steady performance.
16. Investigate proper CO poisoning test condition for PEMFC.
17. Then inject air into anode fuel stream by the equivalent or periodic, or change fuel back to the pure H_2 to observe current recovery rate.
18. Investigate different periodic air bleeding polarization curves.
19. Replace CO concentration of the anode fuel and dose different air periodic. Repeat the procedure from (16)-(18) steps and observe fuel cell CO tolerance.

2.6.2 Micro PEMFC

1. Connect all electric wires of test station with micro fuel cell before the experiment. For instance, connect potential sensors to the current collectors, connect positive pole loading line to the cathode current collector. Connect anode with negative pole. Then, connect pipelines to the micro fuel cell.
2. Add the water to the humidification bottle by the atmosphere style water bottle.
3. Open the valves of H₂, O₂, N₂, and air fuel cylinders and retain the inlet pressure up to 40 psi.
4. Turn on the globe valves of the gas pipelines on the controller operation board, anode side turns to H₂ pipeline, cathode side turns to O₂ or air pipeline.
5. Check if any fuel gases leakage from pipeline's connection by applying suds on them.
6. Activate the software of the test system.
7. Set the minimum fuel flow rate of anode and cathode. The minimum flow rates of anode and cathode are 31.2 cm³/min and 21 cm³/min, respectively.
8. Set anode and cathode humidification temperature.
9. Push down the gas reset button on the power supply board. At the same time, solenoid valve will shut off N₂, which stops to purge the micro fuel cell.
10. Push down the applying fuel icon of software window. The anode and cathode fuel pipeline solenoid valve will open and the fuel gas is fed into the micro fuel cell.
11. Micro fuel cell is held at ambient temperature.

12. Push down the “apply load” icon of the window that the electrical load will start loading from the test sample as the OCV reaches the steady state value.
13. Set the same cell over-potential to activate the micro fuel cell. In general, a micro fuel cell needs to activate several hours until it achieves optimum or steady performance.
14. Investigate different test conditions to find out the optimal performance for micro PEMFC.

2.7 Uncertainty Analysis

The uncertainty analysis may be a simple verbal appraisal of the results, or it may take the form of a complex theoretical analysis of the errors involved in the experiment and matching of the data with fundamental physical principles. Therefore, their accuracy should be confirmed before the analyses of experimental results. Experimental measuring must have errors, and experimental errors divide into the fixed (systematic) error and random (non-repeatability) error, respectively [62]. Fixed error is produced after each experiments and it can be removed by proper calibration and correction. However, Random error is different for every apparatuses reading datum and hence cannot be removed. The objective of uncertainty analysis is to estimate the probable random error in experimental results.

2.7.1 Propagation of Uncertainty Analysis in Calculations

Uncertainty analysis estimates the uncertainty levels in the experiment. A method of estimating uncertainty in experimental results has been presented by

Kline and McClintock [63] as follows.

Suppose a set of measurements are made and the uncertainty in each measurement may be expressed with the same odds. These measurements are then used to calculate some desired results of the experiments. The result R is a given function of the independent variables $x_1, x_2, x_3, \dots, x_n$. Thus,

$$R = R(x_1, x_2, x_3, \dots, x_n) \quad (2-1)$$

An individual x_n , which affects error of R , can be estimated by the deviation of a function. A variation, δX_n , in x_n would cause R to vary according to:

$$\delta R_n = \frac{\partial R}{\partial x_n} \delta x_n \quad (2-2)$$

Normalize above equation by dividing R to obtain:

$$\delta \frac{R_n}{R} = \frac{1}{R} \frac{\partial R}{\partial x_n} \delta x_n = \frac{x_n}{R} \frac{\partial R}{\partial x_n} \frac{\delta x_n}{x_n} \quad (2-3)$$

Equation (2-3) can be used to estimate the uncertainty interval in the result due to the variation in x_n . Substitute the uncertainty interval for x_n ,

$$u_R = \frac{x_n}{R} \frac{\partial R}{\partial x_n} u_{x_n} \quad (2-4)$$

To estimate the uncertainty in R due to the combined effects of uncertainty intervals in all the x_i , it can be shown that the best representation for the uncertainty interval of the result is:

$$u_r = \pm \left[\left(\frac{x_1}{R} \frac{\partial R}{\partial x_1} u_1 \right)^2 + \left(\frac{x_2}{R} \frac{\partial R}{\partial x_2} u_2 \right)^2 + \dots + \left(\frac{x_n}{R} \frac{\partial R}{\partial x_n} u_n \right)^2 \right]^{\frac{1}{2}} \quad (2-5)$$

2.7.2 The Uncertainty Analysis of CO Concentrations

In the present thesis, it discusses the poisoning influence with the CO concentrations of 25, 52.7, and 100 ppm, respectively. These gases are analysed by using the GC-DID method and the accurate value of CO concentration contained in the H_2 can be ensured.

2.7.3 The Uncertainty Analysis of Test Station Apparatuses

The apparatuses must to be corrected by other standard instruments to make sure that they can normally operate and let the inaccuracy of the experimental results reduce to the minimum.

2.7.3.1 HP 6060B Electrical Load: u_V , u_A

The HP 6060B electrical load in the test station has been corrected its potential and current meter before experiment. The research uses FLUKE 8060A Digital Multimeter and Chroma Smart N300-040 Electrical load to correct HP load box. Table 2.1 shows the error for different potentials.

Next, the DC current meter of HP load box is corrected. They use Chroma Smart electrical load and FLUKE digital meter to find the impedance of the shunt. They connect the shunt between HP load box and DC power source after correcting and adjust different potentials of power source, therefore, it can change the measurement current of load box meter. At the same time, the shunt measures a signal of current. After converting this signal, it can define the actual current of this circuit. Table 3.2 shows the error for different current.

2.7.3.2 Mass Flow Controller

There are three MFCs in the test station comprising anode, cathode and oxygen bleeding flow meter in this thesis. The specified error is shown as follows:

$$ERROR (\%) = \frac{CALAUATED-TARGET}{FULLSCALE} \times 100\% \quad (2-6)$$

The ranges of MFC specified accuracy are $1000 \pm 0.1\%$ with anode MFC, $2000 \pm 0.2\%$ with cathode MFC and $500 \pm 0.07\%$ with air bleeding MFC.

They use the same company instrument, series 5850 MFC, as the standard correction apparatus to correct these MFCs. The results are listed in the Table 2.3, 2.4, and 2.5, respectively. They are anode, cathode and air bleeding flow meter, respectively. In these tables, the standard value means the setting flow rate, the Brooks MFC read value means the test station MFC readout value, the measurement value is the actual measured value. Then, these data can define the errors in different flow rates.

2.7.3.3 Temperature Controller

There are three temperature controllers in the test station. They are anode humidifier, cathode humidifier and fuel cell, respectively. The results of uncertainty analyses are listed in Table 2.6, 2.7, and 2.8, respectively. The standard value indicates the setting temperature and the measure value reveals actual value that is measured by the correction apparatus in these tables.

2.7.4 The Uncertainty Analysis of PEMFC and Micro PEMFC

The uncertainty analysis of PEMFC and micro PEMFC results from measuring process of fuel cell apparatus. The minimum scale of measuring voltage in the apparatus is 1 mV, and the minimum scale of measuring current density in the apparatus is 0.1 mA/cm². The Appendix A shows the measuring uncertainty analysis calculating process in detail. Table 2.9 shows the PEMFC and micro PEMFC uncertainty analysis of voltage, current density, and power density, respectively.

2.7.5 The Experimental Repeatability

In general speaking, the life of the commercial MEA is about 300 hours,

therefore, the fuel cell performance will decline with an increase of test time. Moreover, CO makes anode catalyst decaying and aging in the poisoning test, the life of fuel cell is expected to be shorter. In order to improve the cell CO tolerance, the thesis uses air bleeding technique as the CO oxidant to remove the adsorbed CO from catalyst surface. However, the major amount of O₂ will react with H₂ to form water and resultant reaction heat is quite high. This is the other factor that may cause anode catalyst decay. Therefore, the thesis must complete experiment as quick as possible to reduce the effect of time, which influences the experiment results. According to these factors, the thesis is difficult to perform repeatability test. In order to confirm the accuracy and confidence of the experiment, the cell performance must recover to the base performance before it carries out the next poisoning experiment.

All of the experimental works in PEMFC and micro PEMFC tset for three times and calculate the average values to perform results. The repeatability test samples of PEMFC and micro PEMFC polarization curves are shown in Fig. 2.24, and 2.25, respectively.

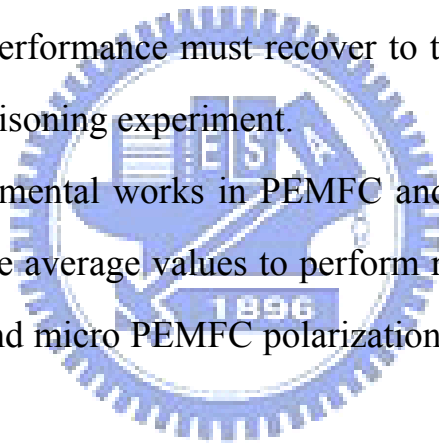


Table 2.1 Uncertainty analysis of electrical load potential meter

Standard value voltage (V)	Digital meter voltage (V)	Uncertainty (%)
20	19.81	-0.95
9.95	9.85	-1
8.02	7.95	-0.87
6.04	5.95	-1.49
5	4.97	-0.6
3.03	3	-0.99
1	0.998	-0.2
0	0	0

Table 2.2 Uncertainty analysis of electrical load current meter

Fluke digital meter (mV)	Electrical load (A)	Conversion value (\bar{A})	Uncertainty (%)
0	0	0	0
1.69	1	1.02	2
5.05	3	3.04	1.33
8.37	5	5.03	0.6
16.71	10	10.05	0.5
25.04	15	15.06	0.4
33.41	20	20.09	0.45
50.21	30	30.19	0.63

Table 2.3 Uncertainty analysis of anode MFC

Standard value (cm ³ /min)	Brooks MFC read value (cm ³ /min)	Measure value (cm ³ /min)	Uncertainty (%)
1000	1002	1001	-0.1
500	501	499.8	-0.24
250	250.2	249.7	-0.2
0	0	0	0

Table 2.4 Uncertainty analysis of cathode MFC

Standard value (cm ³ /min)	Brooks MFC read value (cm ³ /min)	Measure value (cm ³ /min)	Uncertainty (%)
2000	1999.8	1999.4	-0.02
1250	1255	1253	-0.16
1000	1000.3	1000.2	-0.01
500	500.2	500	-0.04
0	0	0	0

Table 2.5 Uncertainty analysis of air bleeding MFC

Output voltage (V)	Brooks MFC read value (cm ³ /min)	Measure value (cm ³ /min)	Uncertainty (%)
5	500	500.34	0.07
3.75	375	374.54	-0.12
2.5	250	250.32	0.13
1.25	125	124.54	-0.37
-0.001	0	0	0

Table 2.6 Uncertainty analysis of anode temperature controller

Standard value (°C)	Measure value (°C)	Uncertainty (%)
25	25	0
35	35	0
50	50	0
70	70	0
85	84	-1.18
95	94	-1.05
100	99	-1

Table 2.7 Uncertainty analysis of cathode temperature controller

Standard value (°C)	Measure value (°C)	Uncertainty (%)
25	25	0
35	35	0
50	50	0
70	70	0
85	85	0
95	94	-1.05
100	99	-1

Table 2.8 Uncertainty analysis of cell temperature controller

Standard value (°C)	Measure value (°C)	Uncertainty (%)
25	25	0
35	35	0
50	50	0
70	70	0
85	85	0
95	95	0
100	100	0

Table 2.9 The measuring uncertainty analysis of PEMFC and micro PEMFC

PEMFC	The measuring uncertainty analysis	Voltage	$\pm 0.1\%$
		Current density	$\pm 0.003\%$
		Power density	$\pm 0.1\%$
Micro PEMFC	The measuring uncertainty analysis	Voltage	$\pm 0.1\%$
		Current density	$\pm 0.005\%$
		Power density	$\pm 0.1\%$

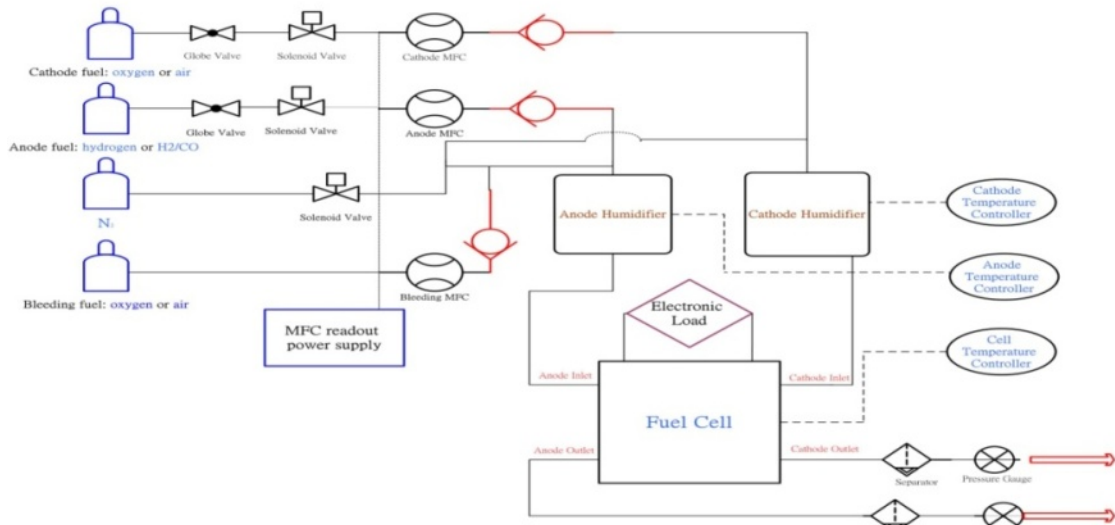


Fig. 2.1 Schematic diagram of the PEMFC experimental setup



Fig. 2.2 HP 6060B electrical load



Fig. 2.3 MFC readout power supply



Fig. 2.4 Power supply



Fig. 2.5 Gas pipelines controller



Fig. 2.6 The fuel cell test station

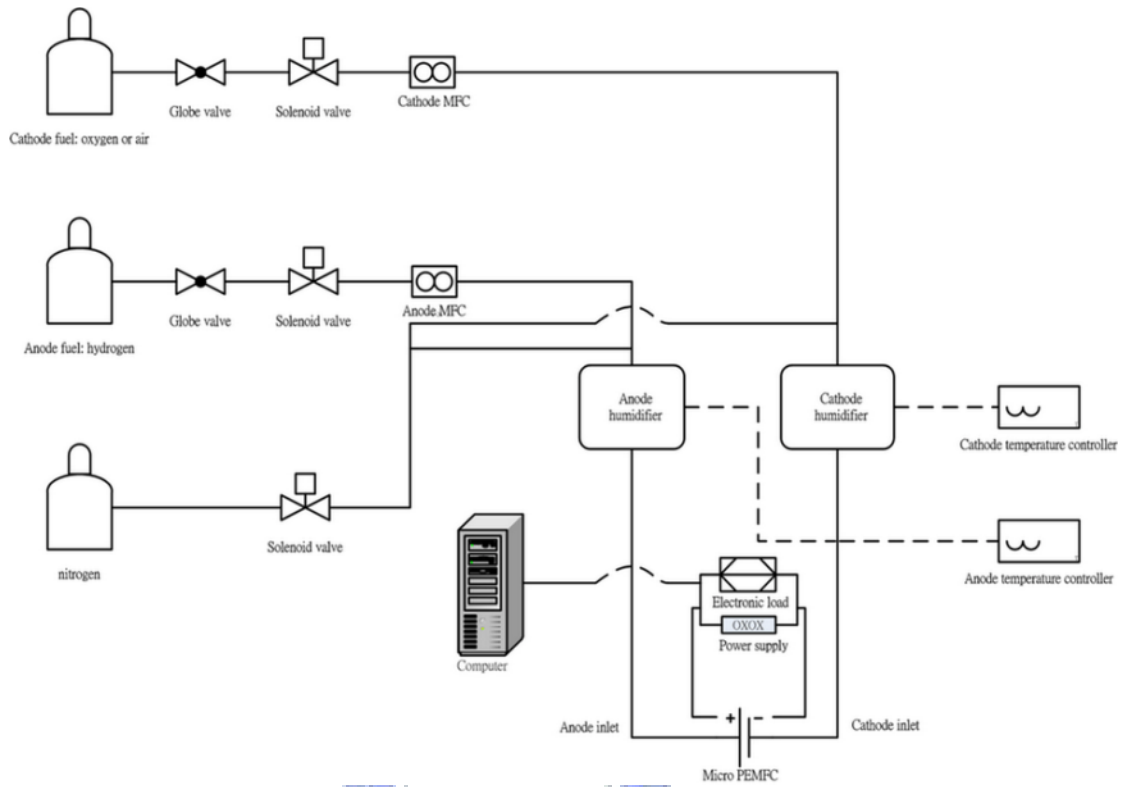


Fig. 2.7 Schematic diagram of the micro PEMFC experimental setup



Fig. 2.8 MEA, GDL, and gasket

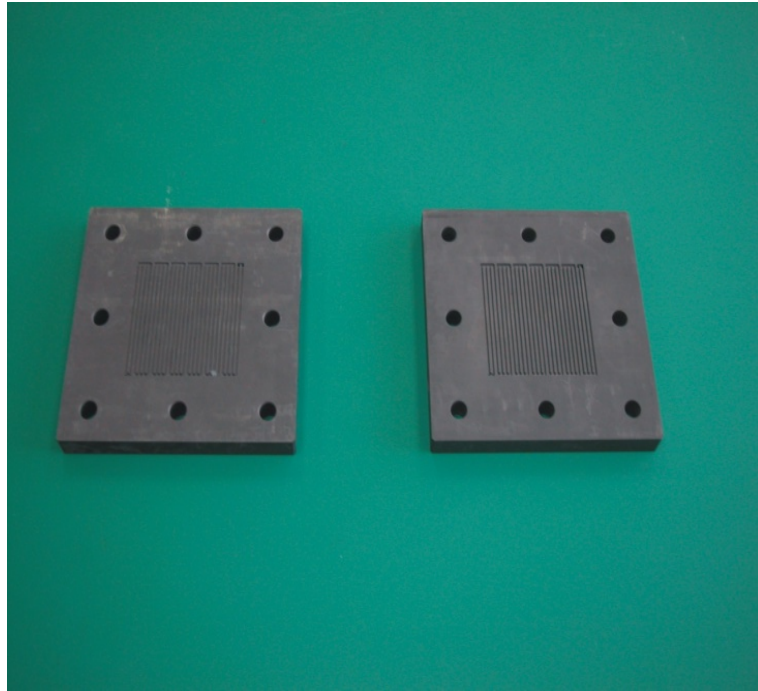


Fig. 2.9 Flow field plate



Fig. 2.10 Current collector

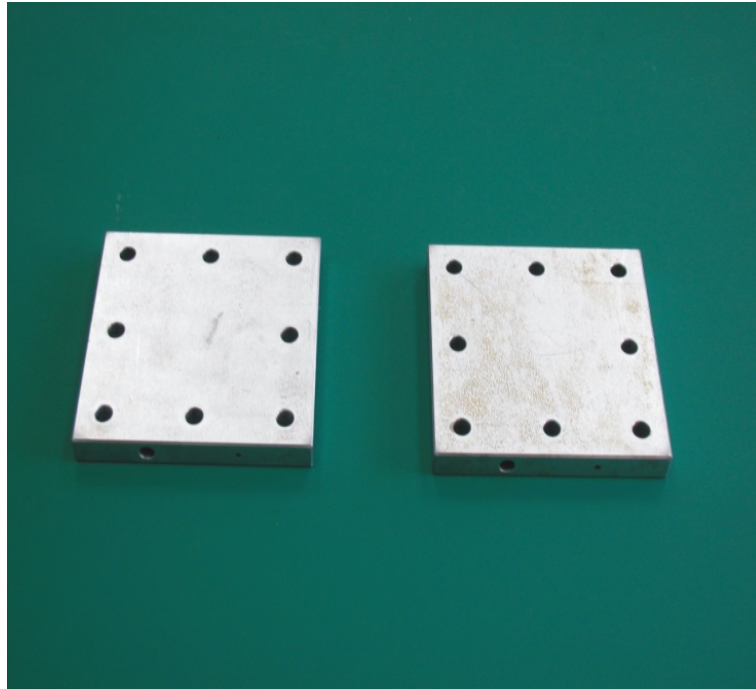


Fig. 2.11 End plate



Fig. 2.12 All components of PEMFC

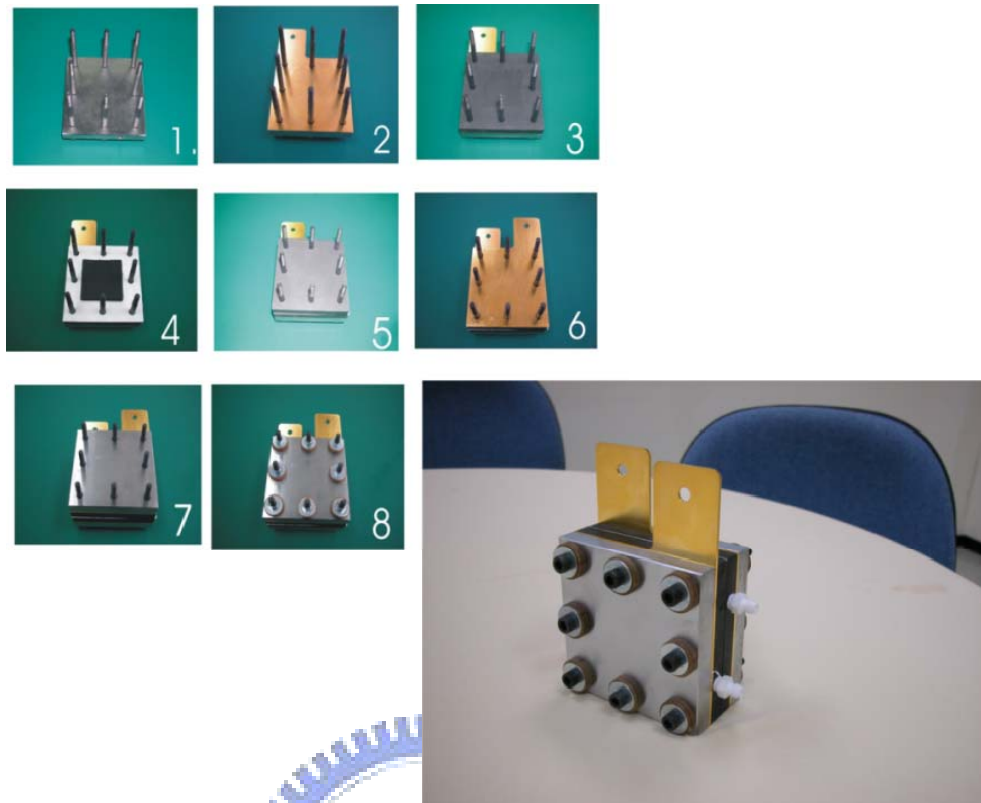


Fig. 2.13 The sequence of fabricating PEMFC

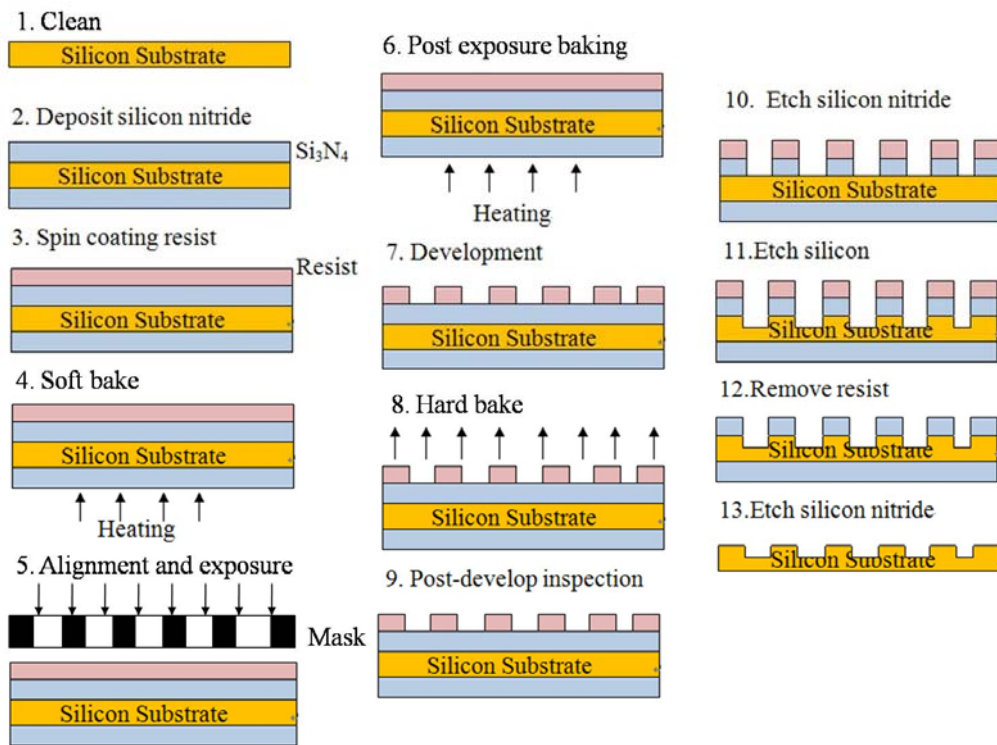


Fig. 2.14 Silicon wafer etching processes



Fig. 2.15 RCA cleaning (Wet bench)



Fig. 2.16 LPCVD



Fig. 2.17 Spinner



Fig. 2.18 Exposure



Fig. 2.19 Wet etching chemical hood

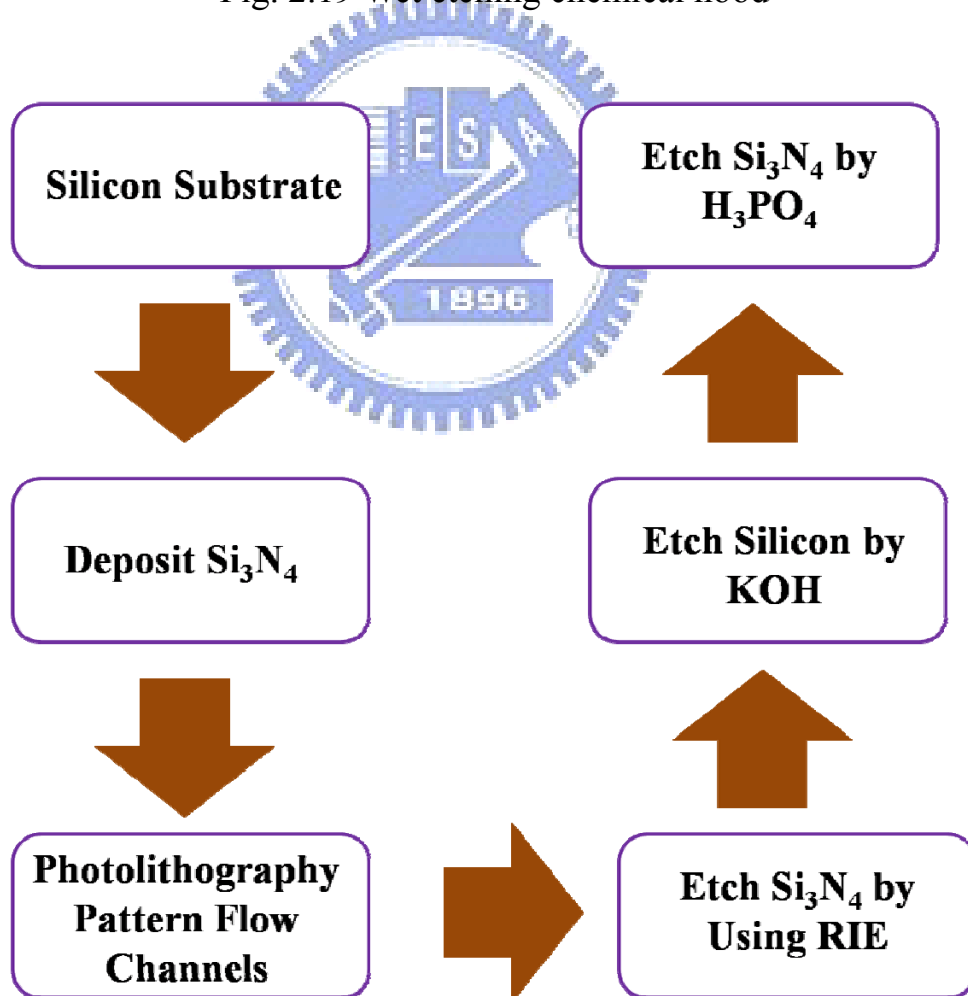


Fig. 2.20 Fabrication flowchart

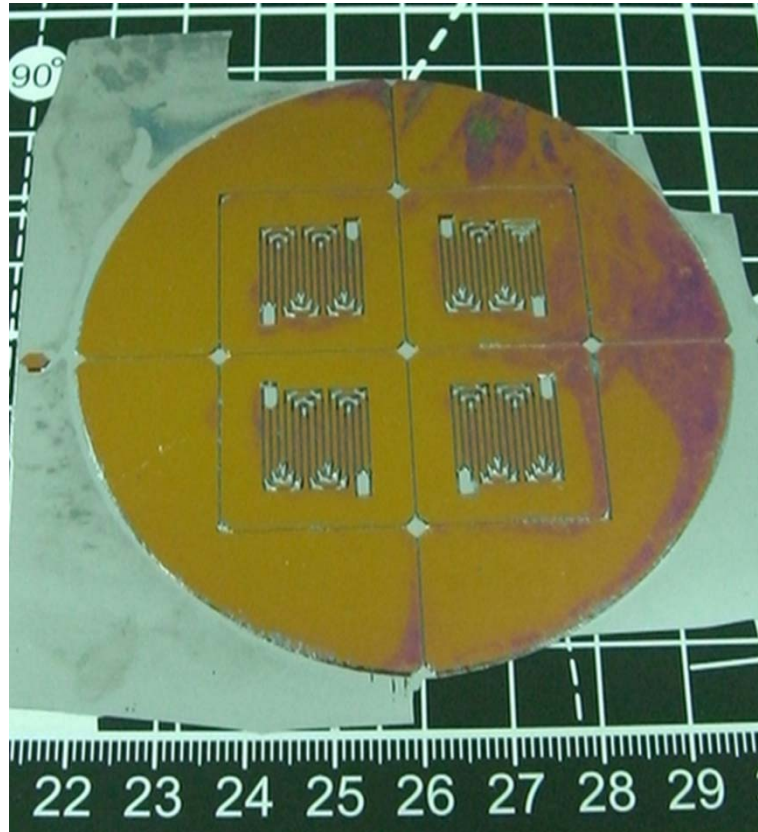


Fig. 2.21 Silicon substrates after etching processes

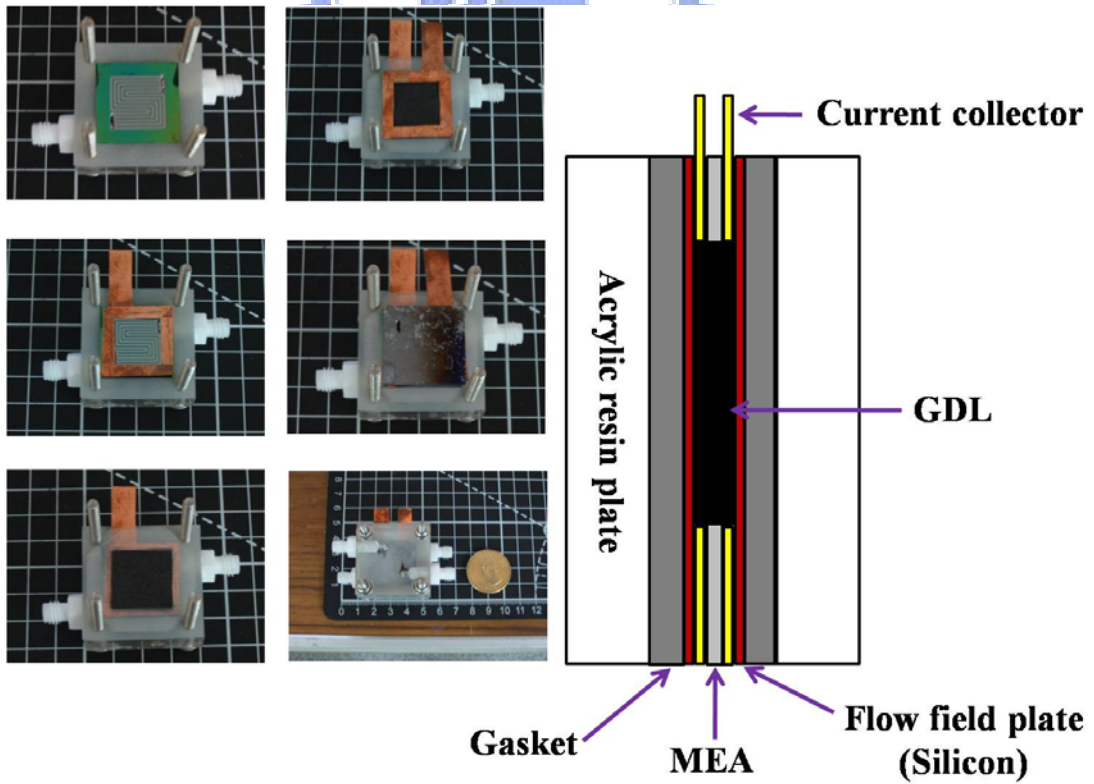


Fig. 2.22 The sequence of fabricating micro PEMFC

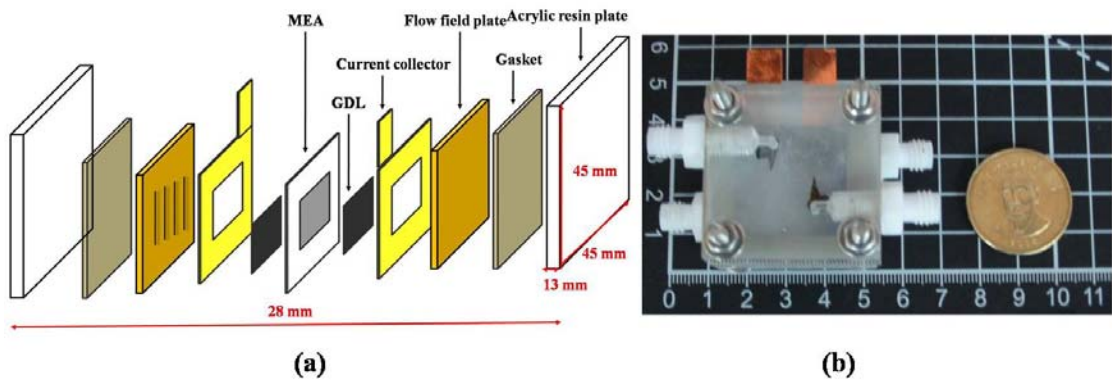


Fig. 2.23 (a) Scheme of micro PEMFC; (b) Picture of micro PEMFC

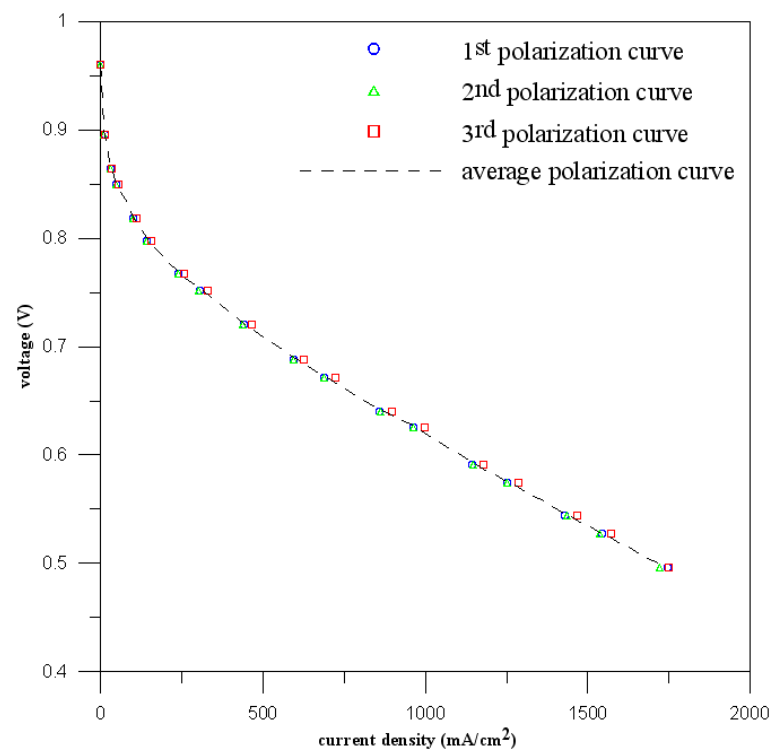


Fig. 2.24 The repeatability test sample of PEMFC polarization curves

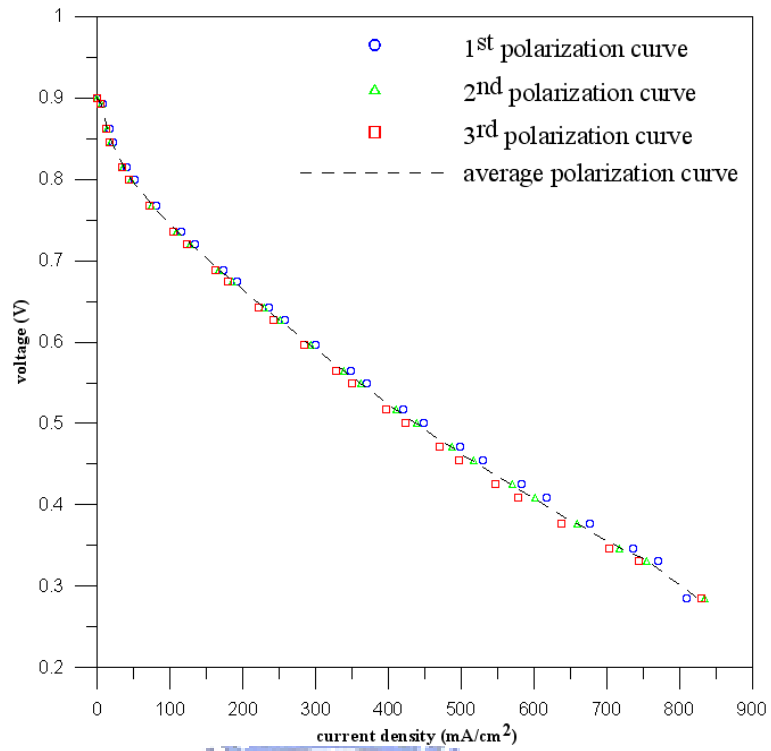
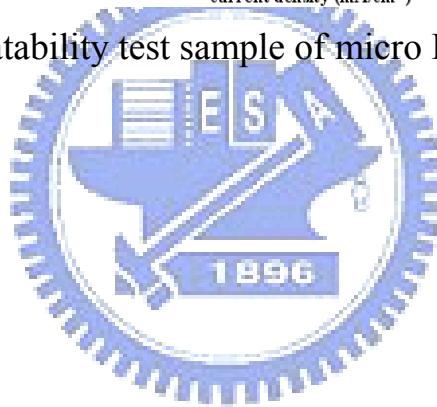


Fig. 2.25 The repeatability test sample of micro PEMFC polarization curves



CHAPTER 3

MICRO PEMFC MATHEMATICAL MODEL

3.1 Basic Assumptions

The following assumptions are utilized to simplify simulation conditions for studying the effect of water and temperature distributions on the performance of micro PEMFC. The simulations performed in this study are based on the flow is steady state, laminar and neglects gravity effect. The gases obey ideal gas and are distributed uniformly at the inlet. The flows in catalyst layer, gas diffusion layer (GDL) and gas flow channels are gas phase without considering the effects of vaporization and condensation. Diffusion of the multi-component gas streams through the electrodes may be described using the Stefan-Maxwell equation. Butler-Volmer equation is used to describe electrochemical reaction within the catalyst layer. Nernst-Planck equation is used for the transport of protons through the membrane. Ohm's law is applied across whole region of the polarization curve. The catalyst layer, GDL and membrane are all isotropic porous media. The membrane is impermeable for gases and electrons. Physical transport properties are considered as constant in each domain.

3.2 Governing Equations in Flow Field Plate and Porous Media

The three dimensional mathematical model consists of the conservation equations of mass, momentum, species, charge, and energy in a fully integrated finite-volume solver using the CFD-ACE+ commercial code. The conservation equations used are listed as follows. Further details can be found in Mazumder

and Cole [64].

Based on the above assumptions, the conservation equations of mass, momentum and species in the gas flow channels and porous media (catalyst layer, GDL, and membrane) are follows:

Mass conservation equation [65]:

$$\frac{\partial}{\partial t}(\varepsilon\rho) + \nabla \cdot (\varepsilon\rho\vec{U}) = 0 \quad (4-1)$$

Momentum conservation equation [65]:

$$\frac{\partial}{\partial t}(\varepsilon\rho\vec{U}) + \nabla \cdot (\varepsilon\rho\vec{U}\vec{U}) = -\varepsilon\nabla p + \nabla \cdot (\varepsilon\tau) + \frac{\varepsilon^2\mu\vec{U}}{\kappa} \quad (4-2)$$

where ε is the porosity, ρ is the fluid density, U is the fluid velocity vector, p is the pressure, τ is the shear stress tensor, μ is the dynamic viscosity, and κ is the permeability (the square of effective volume to the surface area ratio of a porous medium). The last term in Eq. (4-2) represents Darcy's drag force imposed by pore walls on the fluid, which leads to a significant pressure drop across the porous medium. In purely open regions, such as in the gas flow channels, $\varepsilon \rightarrow 1$ and $\kappa \rightarrow \infty$, and Eqs. (4-1) and (4-2) reduce to the well-known Navier-Stokes equations.

Species conservation equation [65]:

$$\frac{\partial}{\partial t}(\varepsilon\rho Y_i) + \nabla \cdot (\varepsilon\rho\vec{U}Y_i) = \nabla \cdot J_i + \dot{\omega}_i \quad (4-3)$$

where Y_i is the mass fraction of the i -th species, J_i is the mass diffusion flux of the i -th species and $\dot{\omega}_i$ is the mass production rates of the i -th species in gas phase. $\dot{\omega}_i$ due to heterogeneous electrochemical reactions is non-zero within the porous media, and is zero elsewhere. It is written as [65]:

$$\dot{\omega}_i = \frac{jM_i}{2nF} \left(\frac{S}{V}\right)_{eff} \quad (4-4)$$

where j is the net transfer current density due to electrochemical reaction, M_i is the molecular weight of the i -th species, n is the number of electrons transferred

during the electrochemical reaction, and F is the Faraday constant. $\left(\frac{S}{V}\right)_{\text{eff}}$ represents the ration of the active surface area of the catalyst to its overall volume (including the support).

The Stefan-Maxwell equation [66] for multi-component gas mixture is considered for the molecular transport in the gas diffusion electrodes.

$$\nabla x_i = \sum_{j=1}^n \frac{RT}{pD_{ij}^{\text{eff}}} (x_i N_{j,g} - x_j N_{i,g}) \quad (4-5)$$

where x_i is the mole fraction of species i , $N_{i,g}$ is the superficial gas-phase flux of species i averaged over a differential volume element, which is small with respect to the overall dimensions of the system, but large with respect to the pore size. The quantity D_{ij}^{eff} is an effective binary diffusivity of the pair i - j in the porous medium.

The diffusion flux is given by Stefan-Maxwell equation relationship [67]:

$$\vec{J}_i = -\sum_{j=1}^n \rho D_{i,j} \nabla M_j \quad (4-6)$$

where $D_{i,j}$ is the binary diffusion coefficient of species i in species j .

The species diffusion flux may be written as [68]:

$$J_i = \rho D_i \nabla Y_i + \frac{\rho Y_i}{M} D_i \nabla M - \rho Y_i \sum_j D_j \nabla Y_j - \rho Y_i \frac{\Delta M}{M} \sum_j D_j Y_j \quad (4-7)$$

where M is the mixture molecular weight and D_i is the effective mass diffusion coefficient of species i . The first term represents Fickian diffusion due to concentration gradients. The last three terms are correction terms necessary to satisfy the Stefan-Maxwell equations for multi-component species i within the porous medium, and depend on the porosity, ε , and tortuosity, δ , of the medium:

$$D_i = D_{i,FS} \varepsilon^\delta \quad (4-8)$$

where $D_{i,FS}$ is the free stream diffusion coefficient of the i -th species. ε is the porosity of the medium and δ is the tortuosity of the medium. It is a common

practice to use tortuosity value of 1.5 in Eq. (4-8) for catalyst layer and GDL, resulting in the so-called Bruggemann model.

The temperature field of each domain is acquired by solving the energy conservation equation, which is written as [69]:

$$\nabla \cdot (\varepsilon \rho \vec{U} h) = \nabla \cdot q + \varepsilon \tau \cdot \nabla \vec{U} - j_e \left(\frac{S}{V} \right)_{eff} \eta + \frac{|j \cdot j|}{\sigma} \quad (4-9)$$

where h is the gas enthalpy, q is the heat flux comprised of contributions due to thermal conduction, j_e is the exchange current density, S is the reaction surface area, V is the medium volume, $\left(\frac{S}{V} \right)_{eff}$ is the effective surface-to-volume ratio, η is the electrode over-potential, j is the transfer current density and σ is the electrical conductivity.

The transfer current density j is expressed using the Butler-Volmer equation [70]:

$$j = j_e \left[\exp\left(\frac{\alpha_a F}{RT} \eta\right) - \exp\left(-\frac{\alpha_c F}{RT} \eta\right) \right] \prod_{i=1}^N [\Lambda_i]^{\alpha_i} \quad (4-10)$$

where j is the reference current density, α_a and α_c are kinetic constants. $[\Lambda_i]$ and α_i are the molar concentrations and the concentration exponents for the i -th species, respectively. Reactant species undergo electrochemical reactions at the electrode catalyst layers. Hydrogen is oxidized at the anode and oxygen is reduced at the cathode. These two reactions are driven by the potential difference between solid phase and electrolyte phase, which is called activation over-potential. The Butler-Volmer equation, which describes this phenomenon, is expressed as [70]:

$$j = j_e \left(\frac{C}{C_{ref}} \right)^\varphi \left[\exp\left(\frac{\beta_{an} F}{RT} \eta\right) - \exp\left(-\frac{\beta_{ca} F}{RT} \eta\right) \right] \quad (4-11)$$

where C is the reactant molar concentration, C_{ref} is the reference molar concentration, φ is the concentration exponent, β_{an} and β_{ca} are kinetic constants

determined from experimentally generated Tafel plots and η is the over-potential between the solid and electrolyte phases of the electrode.

The exchange current density for a reaction, j_e , depends strongly on the compositions and temperature at the reaction interface. The surface over-potential for an electrochemical reaction, η , is defined as [70]:

$$\eta = \Phi_s - \Phi_F - u_0 \quad (4-12)$$

where Φ_s and Φ_F are the electronic potentials of the electronic phase and electrolyte, respectively, at the triple-phase interface. The last term in Eq. (4-12), u_0 , is the thermodynamic equilibrium potential of the reaction, which is, in turn, a function of the reactant and product concentrations at the interface as generally expressed by the Nernst-Planck equation. Note that the surface over-potential, η , represents the driving force for an electrochemical reaction. The thermodynamic equilibrium potentials of anode and cathode are assumed to be zero and a function of temperature, respectively, as [70]:

$$u_0 = 1.23 - 0.9 \times 10^{-3}(T - 298.15) + \frac{RT}{2F} \left(\ln p_{H_2} + \frac{1}{2} \ln p_{O_2} \right) \quad (4-13)$$

In the micro PEMFC calculation, in addition to mass conservation, it is necessary to enforce charge conservation. Under the assumption of electro-neutrality, charge conservation reduces to current conservation, written as [65]:

$$\nabla \cdot \vec{i} = 0 \quad (4-14)$$

where i is the current density vector. In the micro PEMFC, the current flow is due to protons (H^+) flowing through the membrane, resulting in an ionic phase current (i_F), and due to electrons flowing through the carbon in the porous matrix of the GDL, resulting in an electronic phase current (i_S). Thus, Eq. (4-14) can be rewritten as follows:

$$\nabla \cdot i_F + \nabla \cdot i_S = 0 \quad (4-15)$$

Since current transport in the ionic phase is due to ions and that in the electronic phase is due to electrons, the transport in each phase is governed by separate electric potential fields. Using Ohm's law, Eq. (4-15) can be written as:

$$\nabla \cdot (\sigma_F \nabla \Phi_F) + \nabla \cdot (\sigma_S \nabla \Phi_S) = 0 \quad (4-16)$$

where σ_F and σ_S are the conductivities of the ionic and electronic phases, respectively. The exchange of current density from the ionic to the electronic phase occurs due to electrochemical reactions during which electrons are transferred from one phase to the other. Thus, Eq. (4-16) can be rewritten as:

$$-\nabla \cdot (\sigma_F \nabla \Phi_F) = \nabla \cdot (\sigma_S \nabla \Phi_S) = j \left(\frac{S}{V} \right)_{eff} \quad (4-17)$$

The ionic phase electric potential equation (for Φ_F) must be solved in the anode catalyst layer and the membrane, while the electronic phase electric potential equation (for Φ_S) must be solved in the anode catalyst layer and the GDL. In the anode catalyst layer, both equations are solved, and are strongly coupled. The difference in value between Φ_S and Φ_F represents the total electrode over-potential.

The development of the equations for describing the membrane portion of the fuel cell electrode model is based on the macrohomogeneous description given by Bernardi and Verbrugge [66]. A form of the Nernst-Planck equation that includes convection is used to describe the flux of species in the membrane pore fluid, which is written as:

$$N_i = -z_i \frac{F}{RT} D_i C_i \nabla \Phi - D_i \nabla C_i + C_i v \quad (4-18)$$

where N_i is the superficial flux of species i , z_i is the charge number of species i , F is the Faraday constant, R is the universal gas constant, T is the absolute temperature, D_i is the diffusion coefficient of a membrane species i , Φ is the

potential, C_i is the concentration of species i , v is the pore water velocity in the membrane.

The hydrogen-ion concentration in the membrane pore fluid can be considered constant, and diffusion is not a mode of proton transport. The conductivity κ is defined as:

$$\kappa = \frac{F^2}{RT} D_{H^+} C_{H^+} \quad (4-19)$$

Along with the steady state material balance expression follows from continuity equation, which is written as:

$$\nabla \cdot N_i = 0 \quad (4-20)$$

The hydrogen-ion concentration in the membrane pore fluid can be considered constant, and diffusion is not a mode of proton transport. The continuity equation for dissolved-oxygen species results from application of Eqs. (4-18) and (4-20):

$$D_{O_2}^{eff} \nabla^2 C_{O_2} = v \cdot \nabla C_{O_2} \quad (4-21)$$

The migration term of the Nernst-Planck equation vanishes because oxygen is not charged.

During the electrochemical reaction, potential of micro PEMFC drops when reactant species concentrations are deficient on reaction surfaces, especially when operating a micro PEMFC at low operating voltage due to large amounts of water that cause clogging. Concentration loss happens due to water clogging and bending channels. Total concentration loss is expressed as [70]:

$$\eta = \frac{RT}{2F} \left(1 + \frac{1}{\alpha} \right) \ln \frac{C_C^R}{C_L^R} \quad (4-22)$$

where C_C^R is the reactant molar concentration in gas flow channels, C_L^R is the reactant molar concentration in catalyst layers and α is the mass transfer coefficient expressing how variations in electrical potential across reaction

interfaces changes the reaction rate. The value of α depends on the reaction and electrode material.

One concentration loss, which is called Nernst potential change due to reactant species depletion in catalyst layers, has the form [70]:

$$\eta = \frac{RT}{2F} \ln \frac{C_C^R}{C_L^R} \quad (4-23)$$

The second way by which a concentration contributes to concentration loss is via reaction kinetics, and has the form [70]:

$$\eta = \frac{RT}{2\alpha F} \ln \frac{C_C^R}{C_L^R} \quad (4-24)$$

3.3 Boundary Conditions

The governing equations for the present micro PEMFC model are elliptic and partial differential equations. Hence, boundary conditions are required for all boundaries in the computational domain. The temperature of the outer surfaces of flow patterns are maintained at 323K. The conditions of the anode and cathode inlet are a temperature of 323K, and pressure of 3 atm with 3 and 5 stoichiometric flow ratios of 100% H₂ and 100% O₂, respectively. Each outer surface of the flow pattern in the z direction is assigned for specific solid-phase over-potential. This value is set to zero on the anode side, and a total over-potential is set on the cathode side. Con-current flow direction is applied in this investigation.

The boundary conditions are presented as follows:

Anode inlet of the channel:

$$u=u_{in}, T=T_{operating} \quad (4-25)$$

Anode outlet of the channel:

$$P=P_{atm} \quad (4-26)$$

Cathode inlet of the channel:

$$u=u_{in}, T=T_{operating} \quad (4-27)$$

Cathode outlet of the channel:

$$P=P_{atm} \quad (4-28)$$

Outer surface of bipolar plate at Anode:

$$u=0, T=T_{operating}, V_{cell}=0 \quad (4-29)$$

Outer surface of bipolar plate at Anode:

$$u=0, T=T_{operating}, V_{cell}=V_{re}+\eta_{tot} \quad (4-30)$$

where η_{tot} is the total cell overpotential and V_{re} is the reversible voltage given by:

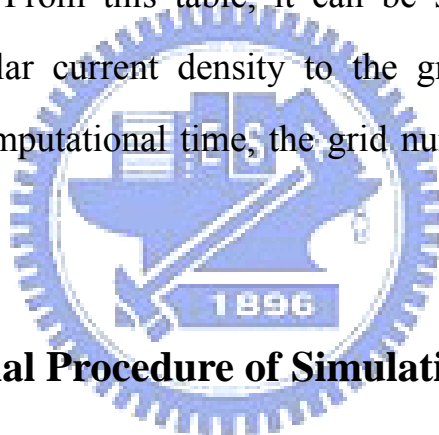
$$V_{re}=0.2329+0.0025T \quad (4-31)$$

3.4 Solution Strategy

Simulations are solved using the commercial computational package CFD-ACE+. The results are regarded to be converged as the normalized residual of each parameters (such as temperature, pressure and gases velocity) are less than 10^{-4} . The physical and chemical properties of the membrane in this model are those determined by Weng *et al.* [71]. The diffusivity of gases are calculated using Stefan-Maxwell equations with Bruggeman correction applied to account for porosity and tortuosity in the porous media. Tables 3.1 and 3.2 are the dimensions and properties of the flow field plate, membrane, electrode material properties and the initial operating conditions used in the numerical simulation. Component parameters and transport properties are obtained by Mazumder and Cole [64] and Springer *et al.* [72] in this study.

3.5 Grid Independence Test

To fully appreciate the mesh required, consider a typical geometry of a micro PEMFC displayed in Fig. 3.1, where the anode flow field (bottom) and cathode flow field (top) sandwich a membrane, catalyst layer with two GDL. For obtaining the acceptable numerical solution, this dissertation applies the unstructured grids produced from geometry models to carry out grid independence test. Three different grid distributions (densities) are tested: there are the grid number of 708392, 740664 and 1539930, respectively. The test results are given in Table 3-3, in which the voltage is fixed at 0.4 V to evaluate the current density. From this table, it can be seen that the grid number of 740664 has the similar current density to the grid number of 1539930. To negotiate with the computational time, the grid number of 740664 is adopted in this dissertation.



3.6 Computational Procedure of Simulation

The complete operating procedure for using CFD-ACE+ package software simulates fuel cell model. The flowchart of solution procedure is shown in Fig 3.2. The first step is setting the boundary values and importing initial conditions. Second, import the computational domain which possesses grids to solver software CFD-ACE-GUI, used to set the model options, the properties of fluid, boundary conditions, and the numerical methods. Then, execute numerical calculation with these data and commands. The solutions first solve the pressure and velocity fields, and then solve the current, potential, temperature and concentration fields in the calculation procedures.

Table 3.1 Dimensions, properties and parameters for the numerical model

Parameters and Properties	Value	Unit	Sources
Channel length	16	mm	Experiment
Channel width	0.3	mm	Experiment
Channel depth	500	μm	Experiment
Rib width	0.7	mm	Experiment
Total reaction area	2.5	cm^2	Experiment
H ₂ and O ₂ side pressure	3	stm	Experiment
Ionic conductivity in GDL and catalyst layer	53	$\text{S}/\Omega\text{m}$	Kamarajugadda, and Mazumder [65]
Ionic conductivity in Membrane	12	$\text{S}/\Omega\text{m}$	Kamarajugadda, and Mazumder [65]
Effective diffusivity	Bruggeman model, $\delta=1.5$ for GDL and catalyst layer		Weng <i>et al.</i> [71]
Effective diffusivity	Bruggeman model, $\delta=7$ for membrane		Weng <i>et al.</i> [71]
Transfer coefficient at anode	0.5		Weng <i>et al.</i> [71]

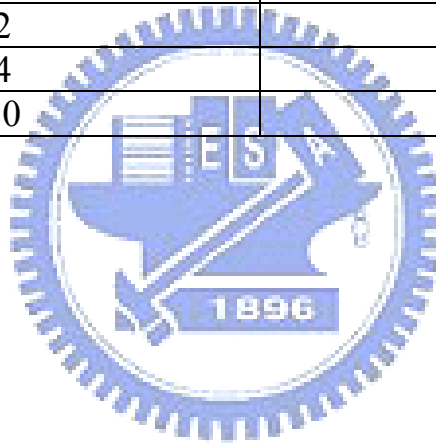
Reference current density at anode	9.23×10^8	$(\text{A/m}^3)[\text{m}^3/(\text{kgmolH}_2)]^{1/2}$	Weng <i>et al.</i> [71]
Transfer coefficients at cathode	1.5		Weng <i>et al.</i> [71]
Reference current density at cathode	1.05×10^6	$(\text{A/m}^3)[\text{m}^3/(\text{kgmolH}_2)]^{1/2}$	Weng <i>et al.</i> [71]
GDL and catalyst layer permeability	1.76×10^{-11}	m^2	Weng <i>et al.</i> [71]
Membrane permeability	1.8×10^{-18}	m^2	Weng <i>et al.</i> [71]
GDL and catalyst layer porosity	0.4		Weng <i>et al.</i> [71]
Membrane porosity	0.28		Weng <i>et al.</i> [71]
Catalyst layer thickness	Anode: 0.018; Cathode: 0.026	mm	Weng <i>et al.</i> [71]
GDL thickness	0.3	mm	Meng and Wang [73]
Membrane thickness	0.025	mm	Meng and Wang [73]

Table 3.2 Operating conditions for the numerical model

H ₂ at fuel inlet (stoichiometric flow rate)	3 and 5
Anode gas	H ₂ , 100%
O ₂ at fuel inlet (stoichiometric flow rate)	3 and 5
Cathode gas	O ₂ , 100%
Operating pressure (atm)	1
Operating temperature (K)	323

Table 3.3 Grid independence test

Grids	Current density (mA/cm ²)
708392	1250
740664	1169
1539930	1165



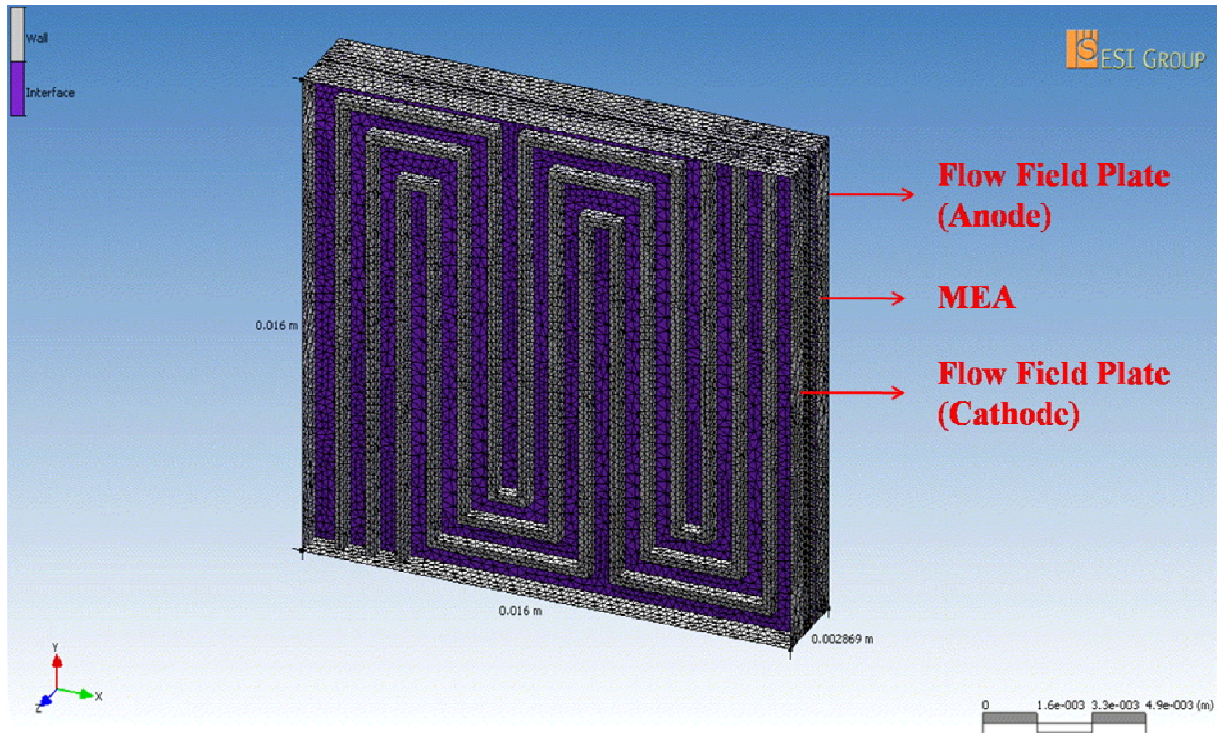
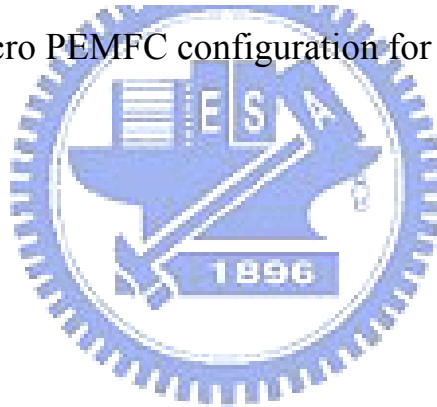


Fig. 3.1 Micro PEMFC configuration for numerical modeling



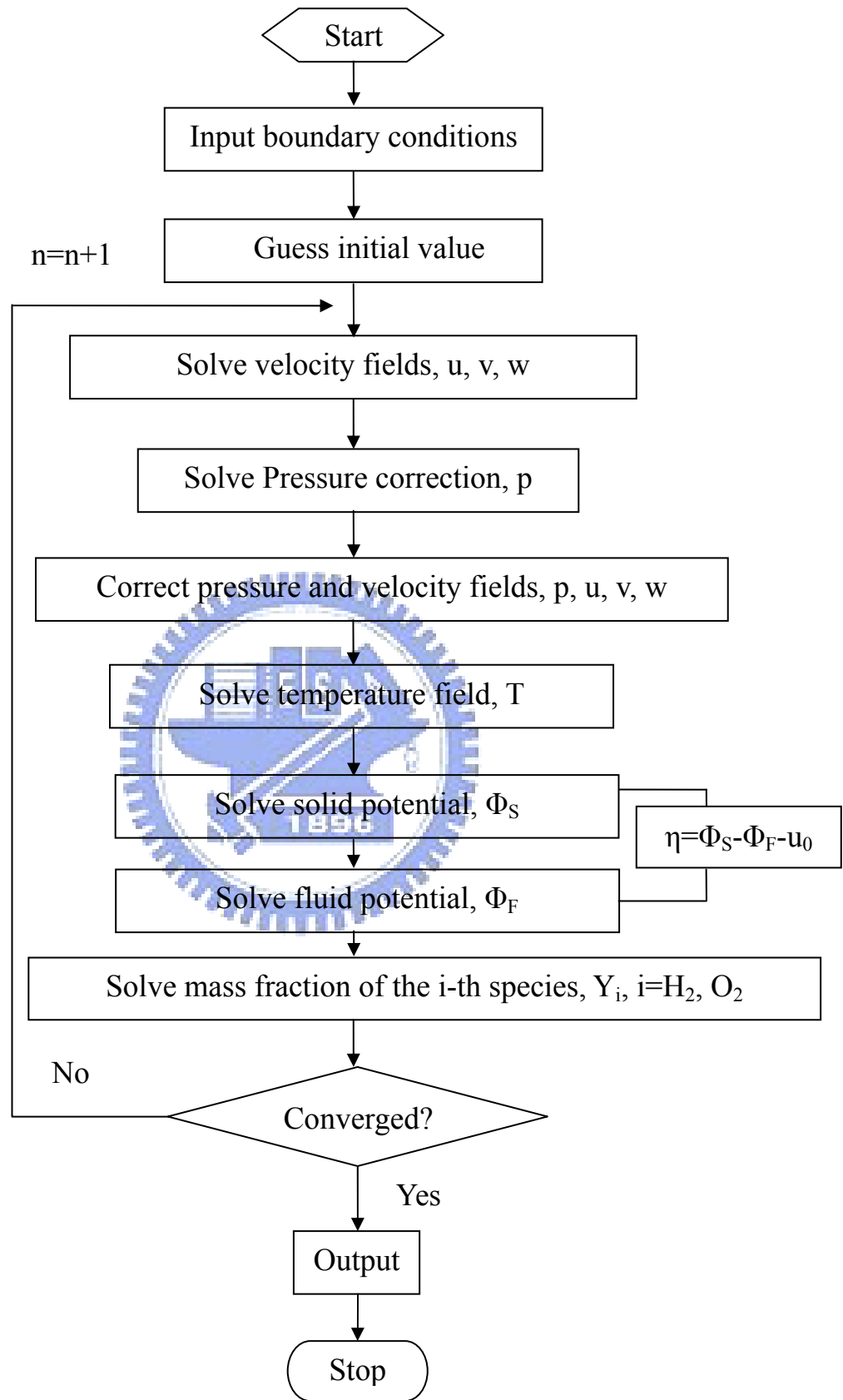


Fig. 3.2 Flowchart of CFD-ACE+ solution algorithm

CHAPTER 4

RESULTS AND DISCUSSION

The first part of this dissertation is using intermittent air dosing to the anode fuel when the PEMFC is poisoned by CO, and the second one is to develop a process for fabricating a micro PEMFC with a simple structure using MEMS technology applied on a silicon substrate. A corresponding numerical simulation results are also provided. Figure 4.1 shows the flowchart of this dissertation. The details are discussed as follows.

4.1 CO Poison Effects on PEMFC

The test results of CO tolerance experiments are given and discussed in this section. They include three scenarios, which one is dosing different air concentrations to carry out a suitable air ratio. After that, it will discuss the effects of dosing different periodic air bleeding into the poisoned cell when the voltage is fixed at 0.6 V. Finally, the long time tests with CO tolerance are discussed.

4.1.1 The Effects of 25 ppm CO Poisoning when PEMFC Dosing Different Air Concentrations

As shown in Fig. 4.2, air ratio continues to change until the air bleeding condition gets a steady state. The experiment fixes the voltage at 0.6 V and injects pure hydrogen and pure oxygen at the first 15 min, which is as a base line. Then, the fuel gas is switched to H₂-CO 25 ppm after 15 min. The experiment finds that the current density decays rapidly as the injection of CO in the anode.

When current density decays to 700 mA/cm^2 , it becomes gentle. Thus, air bleeding starts at the 100th minute. First, inject air of 2% concentration into the anode for 15 min (100th~115th minute), and raise current density from 700 mA/cm^2 to 1608.2 mA/cm^2 ; then, inject air of 4% concentration at the 115th~130th minute with current density from 1608.2 mA/cm^2 to 1689.7 mA/cm^2 ; and inject air of 6% concentration with decreasing current density from 1689.7 mA/cm^2 to 1687.3 mA/cm^2 at the 130th~145th minute as well; to follow, inject air of 8% concentration at the 145th~160th minute with current density decreasing from 1687.3 mA/cm^2 to 1685.3 mA/cm^2 ; to carry on injecting concentration of 10% air at the 160th~175th minute with current density decreasing from 1685.3 mA/cm^2 to 1671.9 mA/cm^2 ; moreover, inject concentration of 15% air at the 175th~190th minute with current density decreasing from 1671.9 mA/cm^2 to 1604 mA/cm^2 ; inject concentration of 20% air at the 190th~205th minute with current density decreasing from 1604 mA/cm^2 to 1507.5 mA/cm^2 . Finally, stop air bleeding at the 205th minute and inject $\text{H}_2\text{-CO}$ into the cell at the same time. Start air bleeding (4%) while current density is decaying to 800.8 mA/cm^2 (285th minute). The current density improves to 1759.6 mA/cm^2 at the 300th minute. The transient curve shows that the cell potential recovers to a constant value (1780 mA/cm^2); even the air ratio is raised to 4%. The major consumption of O_2 is used for H_2 oxidation reaction, and just a little fraction is for CO oxidation reaction. Therefore, the excess of O_2 reacts with H_2 in the anode to produce H_2O or H_2O_2 . On the contrary, the air bleeding ratio above 4% may cause a decline in cell performance. The excess of O_2 lessens the amount of H_2 , which can produce oxidation with a catalyst surface. On the other hand, the oxidation of H_2 with O_2 generates heat in the catalyst surface. The heat may destroy anode catalyst and cell membrane to cause a loss of cell performance. The air bleeding

technique is useful to improve the CO tolerance; however, a suitable air ratio is a more important factor.

4.1.2 The Effects of CO Poisoning when PEMFC Dosing Different Periodic Air Bleeding

In this case, it will investigate the effect of air bleeding on CO tolerance improvement. The periodic air dosing leads to a significant CO tolerance improvement of the cell. The continuous air bleeding, a dosing of air for 10 s in intervals of 10 s, 30 s, and 60 s are selected for this test.

4.1.2.1 25 ppm CO

In the transient CO poisoning test (Fig. 4.3), according to the experience of experiments, the cell current density is 1637.4 mA/cm^2 in the first 15 min and the cell performance declines to 450.2 mA/cm^2 after 100 min poisoning even when the CO concentration is 25 ppm. Table 4.1 shows the summary data from the CO poisoning experiments with different periodic air bleeding. To continue air bleeding, cell performance reaches to 1460.6 mA/cm^2 , the recovery rate is 89%. With a dosing of air for 10 s in intervals of 10 s, cell performance reaches to 1358.3 mA/cm^2 , the recovery rate is 83%, which is obvious and conspicuous. Its recovery rate is as good as the continuous air bleeding. On the other hand, with a dosing of air for 10 s in intervals of 30 s and 60 s, cell performance reaches to 1255.5 mA/cm^2 and 1031.1 mA/cm^2 , the recovery rate is only 77% and 63%. Figure 4.4 shows the polarization curves of different air bleeding durations with 25 ppm CO. It is examined while the voltage is above 0.8 V; these curves—the baseline, continuous air bleeding, a dosing of air for 10 s in intervals of 10 s, 30 s,

and 60 s—and any of their current density are extremely close to each other. Therefore, the current density has an obvious difference when the voltage does not reach 0.8 V. That is the reason why the voltage is fixed at 0.6 V. With longer ceasing duration, its performance recovery rate is delayed. The performance recovery rate of a dosing of air for 10 s in intervals of 10 s is extremely close to that of the continuous air bleeding. Hence, a dosing of air for 10 s in intervals of 10 s is chosen in this experiment.

4.1.2.2 52.7 ppm CO

It discusses the effect of CO concentrations with 52.7 ppm on the performance of PEMFC. In the transient CO poisoning test (Fig. 4.5), according to the experience of experiments, the cell performance declines seriously to the minimum after 60 min poisoning and even the CO concentration is 52.7 ppm. The cell current density is 1770.7 mA/cm^2 in the first 15 min and the cell performance declines to 528.2 mA/cm^2 after 60 min poisoning even when the CO concentration is 52.7 ppm. Table 4.2 shows the summary data from the CO poisoning experiments with different periodic air bleeding. To continue air bleeding, cell performance reaches 1667.4 mA/cm^2 and the recovery rate is 94%. With a dosing of air for 10 s in intervals of 10 s, cell performance reaches 1587.3 mA/cm^2 and the recovery rate is 90%. Its recovery rate is as good as the continuous air bleeding. On the other hand, with a dosing of air for 10 s in intervals of 30 s and 60 s, cell performance reaches to 1331.5 mA/cm^2 and 992.2 mA/cm^2 , respectively. They are not worthy to use for fuel cells. Figure 4.6 is the polarization curves of different air bleeding durations with 52.7 ppm CO. A dosing of air for 10 s in intervals of 10 s has a very close performance to that of

continuous air bleeding. On the other hand, the poisoning condition of a dosing of air for 10 s in intervals of 60 s greatly harms the performance.

4.1.2.3 100 ppm CO

In the transient CO poisoning test, the cell performance (Fig. 4.7), according to the experience of experiments, declines seriously after 40 min poisoning even when the CO concentration is 100 ppm (278.3 mA/cm^2). CO concentration (100 ppm) with a dosing of air for 10 s in intervals of 10 s, 30 s, and 60 s are unable to recover adequate performance. Table 4.3 shows the summary data from the CO poisoning experiments with different periodic air bleeding. With a dosing of air for 10 s in intervals of 10 s, the cell performance reaches to 1161.1 mA/cm^2 , and the recovery rate is only 73%. The situation is different with H_2 -CO 25 ppm and 52.7 ppm. With a dosing of air for 10 s in intervals of 30 s and 60 s, cell performance reaches to 453.5 mA/cm^2 and 342.8 mA/cm^2 , respectively. They are also not helpful to the CO tolerance of fuel cells. The performance recovery rate of continuous air bleeding is 89%, but performance recovery rates of the others—a dosing of air for 10 s in intervals of 10 s, 30 s, and 60 s, are 73%, 29%, and 22%, respectively. CO 100 ppm concentration has a great harmful effect on performance of fuel cell. Only continuous air bleeding can recover the cell performance and make it go back near 90% of the baseline. Figure 4.8 shows the polarization curves in pure H_2 and H_2 -CO 100 ppm with continuous air bleeding and a dosing of air for 10 s in intervals of 10 s, 30 s, and 60 s. The presence of 100 ppm CO with continuous air bleeding and a dosing of air for 10 s in intervals of 10 s can improve CO tolerance of fuel cell. However, a dosing of air for 10 s in intervals of 30 s and 60 s can't helpful to the CO tolerance.

4.1.3 Long Time Test of PEMFC with CO Poison

4.1.3.1 25 ppm CO

Figure 4.9 is the transient air bleeding through long time experiment with CO poisoning (25 ppm). From the experiments above mentioned, it is recognized that a dosing of air for 10 s in intervals of 10 s can make the recovery rate reach 84% of cell performance. Thus, this experiment begins with the air bleeding (a dosing of air for 10 s in intervals of 10 s) at the performance dropping to the 84% of the baseline. In the first 15 min, pure hydrogen and pure oxygen are the baseline, and then the fuel gas is switched to H₂-CO 25 ppm into the anode the next 15 min. The average current density is 1737.7 mA/cm² in the first 15 min. The air bleeding starts as soon as the performance drops to the 1464.1 mA/cm² (34 min). The average current density is 1658.5 mA/cm² in the 34th~250th min. Therefore, the performance recovery rate promotes to 95%.

4.1.3.2 52.7 ppm CO

Figure 4.10 is the transient air bleeding through long time experiments with CO poisoning (52.7 ppm), same as the above. The average current density is 1737.7 mA/cm² in the first 15 min, and the air bleeding starts as the performance drops to the 1559.1 mA/cm² (22 min). The average current density is 1605.9 mA/cm² from the 22nd to 250th minute. Then, the performance recovery rate promotes to 92%. From these two experiments, the observations get the pictures that air bleeding begin when the CO poison has little effect on the cell, which can get better performance recovery rate.

It is widely known that air bleeding is very effective to compensate the drop in CO tolerance of the anode. Air bleeding increases the CO tolerance of the fuel cell and effectively improves the performance. With dosing of air for 10 s

in intervals of 10 s is the optimum air bleeding ratio, which had already been found at each CO poisoning concentrations in the previous experiments. O₂ is then more likely to be absorbed on the catalyst surface to react with CO to form CO₂. Accelerating the reaction between O₂ and CO increases the rate of air bleeding. The frequent duration is required to optimize CO tolerance when air is injected into the anode fuel stream. Therefore, the CO tolerance is increased when the duration of air bleeding is used frequently in the CO poisoning tests.

4.2 Micro PEMFC

The test results of micro PEMFC are given and discussed in this section. The experiments investigate different operating conditions to carry out optimal performance, such as fuel temperature, fuel flow rate and channel depth. The experiments are performed at ambient pressure and temperature; pure humidified hydrogen and oxygen are fed into the micro PEMFC. The flow phenomena in a serpentine micro channel attached to a porous transport layer in a micro PEMFC is investigated.

4.2.1 The Effects of Fuel Temperature

Figure 4.11 plots the micro PEMFC polarization curves obtained at fuel temperatures of 30, 40, 50, 60, 70 and 80°C, respectively. Table 4.4 shows the operation conditions in this experiment. At 0.46 V, the current densities are 436.8 mA/cm², 421.8 mA/cm², 402 mA/cm², 469.6 mA/cm², 488.3 mA/cm² and 490.8 mA/cm², respectively. The performance at a fuel temperature of 80°C is a little better than that at 70°C. The average power densities are 225.8 mW/cm² and 224.6 mW/cm², indicating that the optimal fuel temperatures for the micro PEMFC is 80°C in this experiment. Experimental results show that a high fuel

temperature increases gas diffusivity and membrane proton conductivity. Therefore, a high fuel temperature induces electrochemical reactions. These experimental results indicate that cell performance is increased as fuel temperature increases. Restated, micro PEMFC performance depends on fuel temperature.

4.2.2 The Effects of Flow Rate

Figure 4.12 presents the micro PEMFC polarization behavior when the fuel flow rates of H₂/O₂ are changed to 3, 4 and 5 times of the reference flow rate (H₂: 10.4 cm³/min and O₂: 7 cm³/min). Table 4.5 shows the operation conditions in this experiment. As the fuel flow rates increases, cell performance worsens. As mentioned, increasing fuel temperature accelerates electrochemical reactions, and increases the amount of liquid water produced. But the results observe that increasing gas velocity improves the removal of fuel and water produced by the cathode. The high H₂/O₂ stoichiometric ratio flow may not diffuse fuel to the MEA. Moreover, it may make MEA dry and increase proton conduction resistance. Therefore, internal flooding is not obvious. The low H₂/O₂ stoichiometric ratio flow yields better performance than that obtained with the high ones. The maximum current density output with the flow of stoichiometric ratio of 3 is 504.4 mA/cm² at 0.409 V.

These experimental results indicate that the fuel stoichiometric ratio markedly affects cell performance. However, the high H₂/O₂ stoichiometric ratio flow dries out the membrane, which increases electrical resistance. Therefore, the flow of stoichiometric ratio of 5 generates the worst performance.

Figure 4.13 plots polarization curves of pure humidified hydrogen and air, which are used as reactant gases under ambient conditions. The fuel flow rates of H₂/air are controlled at 1, 2 and 3 times of the reference flow rate (H₂: 10.4 cm³/min and Air: 35 cm³/min). Table 4.6 shows the detailed operation conditions in this experiment. The performance becomes poorer than when pure

oxygen is used in the cathode; experimental results demonstrate that current densities are 139 mA/cm², 149.9 mA/cm² and 166.7 mA/cm², respectively, at 0.46 V. These results indicate that the fixed flow of stoichiometric ratio of 3 optimizes the performance of micro PEMFC when the cathode fuel is air.

4.2.3 The Effects of Channel Depth

Two different channel depths, 100 μm and 500 μm, are selected to study their effects on cell performance. Table 4.7 shows the operation conditions in this experiment. Figure 4.14 plots polarization curves obtained by these two different channel depths. It shows that the performance of the deeper channel is better.

In the study of reactant gas transport in PEMFC, a detailed understanding of fuel distribution at the interface between the channel and gas diffusion layer is important to the design of a PEMFC. To this end, the results observe that the fuel in the shallow channels do not diffuse to the GDL. Therefore, the performance becomes very poor because the electrochemical reaction has barely a little fuel to react. Such result emphasizes the importance of channel depth, which is associated with fuel diffusion.

In order to enhance shallow channels' performance, the increases of back pressure on the anode and cathode sides are tested. Figure 4.14 shows the performance of micro PEMFC for H₂/O₂ reaction. The back pressure increases from zero to 0.4 kg/cm², the current density is improved to 405.3 mA/cm² from 174 mA/cm² under the voltage of 0.406 V. Moreover, an increase of 0.8 kg/cm² back pressure on the anode and cathode sides is applied. The current density reaches a value of 494.8 mA/cm² at a potential of 0.406 V. The back pressure adjustment improves the micro fuel cell performance. This may be attributed to an improved humidification of the membrane and of the ionic phase of the catalyst layer, which would reduce the proton conduction resistance. Therefore, the results indicate that the influence of increased back pressure is superposed

here that can increase water production, causing an improved humidification of the ionic phase.

4.2.4 Numerical Simulations for Micro PEMFC

As mentioned previously, the experimental micro PEMFC was manufactured by using MEMS technology based on a silicon substrate. Then, a single micro PEMFC is assembled to be tested to obtain the polarization curve. Now, a series of numerical computations is carried out to simulate the performance for such micro PEMFC. The governing equations are solved using CFD-ACE+ code. The results of numerical simulation are validated with experimental data, and the corresponding polarization curves can be obtained. The experimental measurements of two different stoichiometric H_2/O_2 flows are compared with the corresponding numerical predictions. The polarization curves of hydrogen and oxygen are supplied at the base operating conditions of the flow rates of 3 and 5 times of reference flow rate. The exit pressures of the anode and cathode sides are 1 atm and the cell temperature is held at 323K.

Figure 4.15 and 4.16 display the comparisons between measurements and predictions. The relative difference of current densities between the numerical data are better than that of the experimental data. Since the flow is steady state and the effect of water flooding is neglected in the simulation on the cathode side in a single phase model, the numerical values apparently are over predicted. This reason explains why the numerical data are better than the experimental ones. However, the simulation results help to elucidate the phenomena in the micro PEMFC.

When the fuel flow rate of H_2/O_2 is 3 times of the reference flow rate, the current density is 1170 mA/cm^2 at 0.4 V in simulation. When the fuel flow rate is increased to 5 times of the reference flow rate, the simulated current density is lowered to 693 mA/cm^2 at 0.4 V. Figure 4.17 shows the two polarization curves for two different stoichiometric ratio flows. The results indicate that the lower

stoichiometric ratio flow has a higher limiting current density, which is almost two times of that of the higher one. It indicates that the output current density is dictated by the stoichiometric ratio of the fuel flow, and the superior performance is achieved when applying the lower stoichiometric ratio flow that is attributed to the fuel permeability in the membrane. The low stoichiometric ratio flow enables more fuel to permeate into the membrane and increases cell electrochemical reaction. Therefore, the lower stoichiometric ratio flow can provide a better performance. In addition, the water and temperature distributions of the membrane also can affect micro fuel cell performance.

4.2.4.1 Current Density Distribution

Figures 4.18 (a) and (b) show the distributions of local current density in the membrane at operation voltage 0.4 V. For overall current density distributions, the local current density is increased from inlet toward outlet, leading to a low temperature distribution. The local current density distributions relate to the temperature ones in Figs. 4.20 (a) and (b). The results show that the more uniform temperature distribution (Fig. 4.20 (a)) leads to a higher current density (Fig. 4.18 (a)) because of the higher fuel permeability that enables fuel to reach the membrane easier, therefore, enhances electrochemical reaction. Moreover, the more uniform temperature distribution of micro PEMFC has lower proton conduction resistance and more active electrochemical reaction at midstream to downstream along flow channels. The phenomenon of gradually increasing local current density distribution appears to be significant at the midstream to downstream. This leads to the uniformity of temperature distribution as well as the increase of cell current density. In this study, the micro PEMFC uses small dimension MEA, only 2.5 cm². For this reason, the worse performance caused by the higher fuel flow rate could result in an increase of hot spots in the membrane that damages the membrane structure. Consequently, a uniform temperature distribution is important to membrane proton conductivity that can

increase cell performance. This is verified by the experimental results in Fig. 4.11.

4.2.4.2 Water Distribution

Water management also importantly affects the performance of micro PEMFC. To study the effects of water distribution on micro PEMFC, Figs. 4.19 (a) and (b) present the water distribution in the membrane at operation voltage 0.4 V in the flow rates of 3 and 5 times of the reference flow rate. At fixed over-potential, the water concentration increases from inlet to outlet. The results show that the lower flow rate can increase the electrochemical reaction and the quantity of water produced. The results also indicate that the concentration of water is maximal at the outlet gas channel region adjacent to membrane because the consumption of oxygen produces water by an electrochemical reaction and the oxygen concentration is the lowest there. Then, the water diffuses backward from membrane to gas channel, therefore, water accumulates in the outlet gas channel. The higher flow rate results in a more rapid exhaustion of water and less fuel perform electrochemical reaction. For these reasons mentioned above, the less water accumulates as the higher flow rate, implying that the higher proton conduction resistance leads to worse cell performance.

4.2.4.3 Temperature Distribution

The uniformity of temperature distribution is important for minimizing the material stress on MEA so that its lifetime can be extended. To see how the inside temperature of a micro PEMFC is affected by the electrochemical reaction. The temperature distributions in the membrane surface at the nominal operating condition, 0.4 V, are shown in Fig. 4.20. The temperature slightly decreases with increasing current density because the higher electrochemical reaction rate can produce more water, which can wet membrane to increase proton conduction. Hence, this reveals uniform temperature distribution being able to lead to increase

cell performance. Fig. 4.20 (b) illustrates the high and non-uniform temperature distribution in the membrane at the flow rate of 5 times of the reference flow rate. It shows that the temperature approaches to 360K from the inlet region to the midstream of membrane, and it drops around 350K along the flow path. High temperature may dry membrane to increase proton conduction resistance. The lowest temperature is distributed at right-middle region in the flow channels. This could be due to the existence of low temperature, as the result of water accumulation, at exit region. Therefore, it is important to know the uniformity of temperature distribution indeed can affect electrochemical reaction rate greatly. The low flow rate can make uniform temperature distribution and obtain a better micro PEMFC performance.

4.2.4.4 Water Content Distribution

Water content is given as the ratio of the number of water molecules to that of charge (SO_3H^+) sites. This ratio indicates how well the membrane is hydrated and is the key to reduce membrane electrical resistance. Furthermore, maintaining a uniform distribution of membrane water content can extend micro PEMFC lifetime because the uniform distribution reduces the formation of local hot spots and the flooding that stress and damage MEA. Figure 4.21 (a) and (b) shows the distributions of water content in the membrane at operation voltage 0.4 V in the flow rates of 3 and 5 times of reference flow rate. However, membrane water content in this study is lower than 6 since no liquid water is formed. The results show that current density increases and the membrane water content also increases for these two different flow rates. The results also find out that the higher water content occurs in the case of 3 times of reference flow rate due to the gradual increase of current density distribution comparing with the case of 5. The membrane water content in the flow rate of 3 times of reference flow rate reaches to 2~5 in the midstream to the downstream of the flow channels, whereas in the case of 5 it only reaches to 0~3 in all flow channels. Therefore, it shows

that the water content distribution is based on fuel reaction utilizing rate. The results indicate that the flow rate of 3 times of reference flow rate has higher water content in the membrane due to the higher water production rate from the electrochemical reaction. The water content is linearly related to the proton conductivity such that higher membrane water content leads to higher proton conductivity, which decreases the over-potential caused by ohmic loss. So the micro PEMFC performance is improved.



Table 4.1 Summary data from 25 ppm CO poison experiments with different periodic air bleeding

CO: 25 ppm			
The periodic of air bleeding			
Continue air bleeding	A dosing of air for 10 s in intervals of 10 s	A dosing of air for 10 s in intervals of 30 s	A dosing of air for 10 s in intervals of 60 s
Current density (I) (mA/cm ²)			
1460.6	1358.3	1255.5	1031.1
Reference current density (I _{ref}) (mA/cm ²)			
1637.4			
Recovery rate (I/I _{ref}) (%)			
89	83	77	63

Table 4.2 Summary data from 52.7 ppm CO poison experiments with different periodic air bleeding

CO: 52.7 ppm			
The periodic of air bleeding			
Continue air bleeding	A dosing of air for 10 s in intervals of 10 s	A dosing of air for 10 s in intervals of 30 s	A dosing of air for 10 s in intervals of 60 s
Current density (I) (mA/cm ²)			
1667.4	1587.3	1331.5	992.2
Reference current density (I _{ref}) (mA/cm ²)			
1770.7			
Recovery rate (I/I _{ref}) (%)			
94	90	75	56

Table 4.3 Summary data from 100 ppm CO poison experiments with different periodic air bleeding

CO: 100 ppm			
The periodic of air bleeding			
Continue air bleeding	A dosing of air for 10 s in intervals of 10 s	A dosing of air for 10 s in intervals of 30 s	A dosing of air for 10 s in intervals of 60 s
Current density (I) (mA/cm ²)			
1415.5	1161.1	453.5	342.8
Reference current density (I _{ref}) (mA/cm ²)			
1590.5			
Recovery rate (I/I _{ref}) (%)			
89	73	29	22

Table 4.4 Operation conditions at different fuel temperature

Flow rate (cm ³ /min)	
H ₂	31.2
O ₂	21
Operating temperature (°C)	25
Operating pressure (atm)	1
Fuel temperature (°C)	30
	40
	50
	60
	70
	80

Table 4.5 Operation conditions at different fuel flow rate

Operating temperature (°C)	25
Fuel temperature (°C)	80
Operating pressure (atm)	1
Flow rate (f) (cm ³ /min)	
H ₂	31.2
	41.6
	52
O ₂	21
	28
	35
Reference flow rate (f _{ref}) (cm ³ /min)	
H ₂	10.4
O ₂	7
Stoichiometric ratio (f/f _{ref})	3, 4, 5

Table 4.6 Operation conditions at different fuel flow rate (H₂/air)

Operating temperature (°C)	25
Fuel temperature (°C)	80
Operating pressure (atm)	1
Flow rate (f) (cm ³ /min)	
H ₂	10.4
	20.8
	31.2
Air	35
	70
	105
Reference flow rate (f _{ref}) (cm ³ /min)	
H ₂	10.4
Air	35
Stoichiometric ratio (f/f _{ref})	1, 2, 3

Table 4.7 Operation conditions of two different channel depths

Operating temperature (°C)	25
Fuel temperature (°C)	80
Operating pressure (atm)	1
Flow rate (cm ³ /min)	
H ₂	31.2
O ₂	21
Channel depth (μm)	100
	500

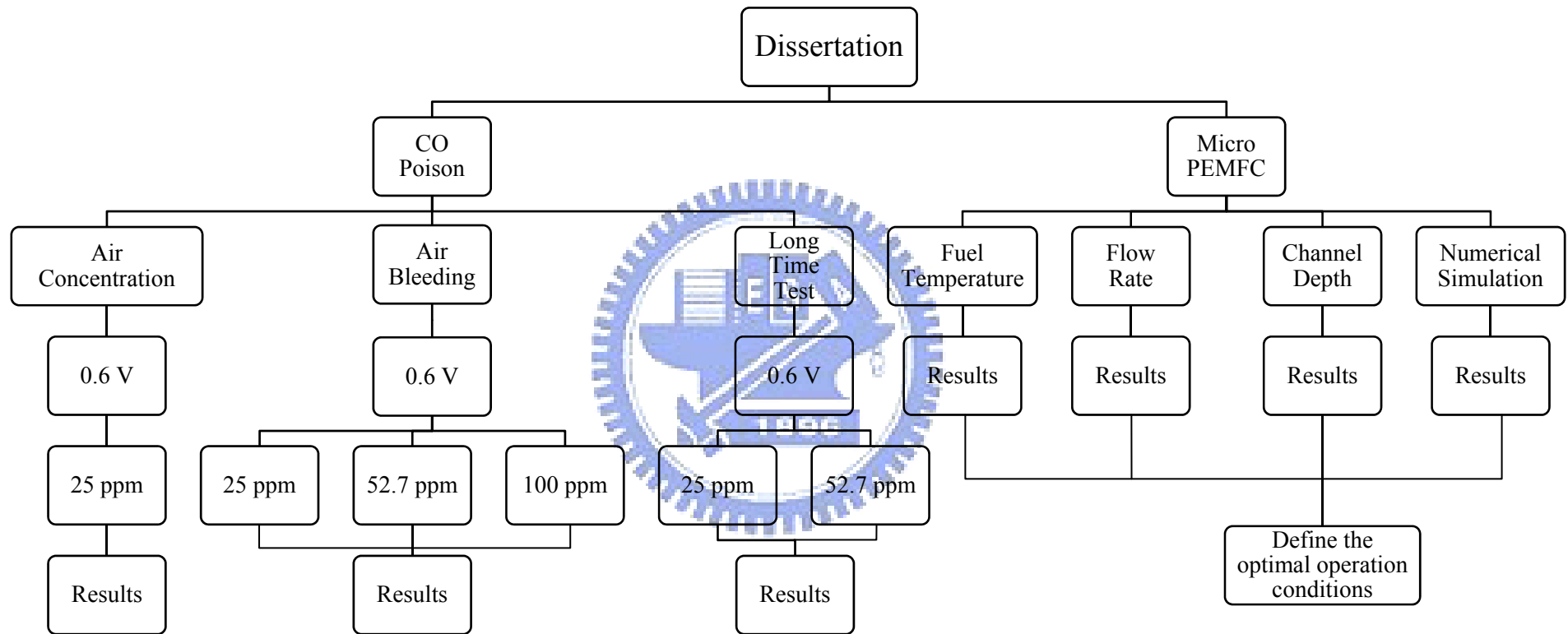


Fig. 4.1 The flowchart of this dissertation

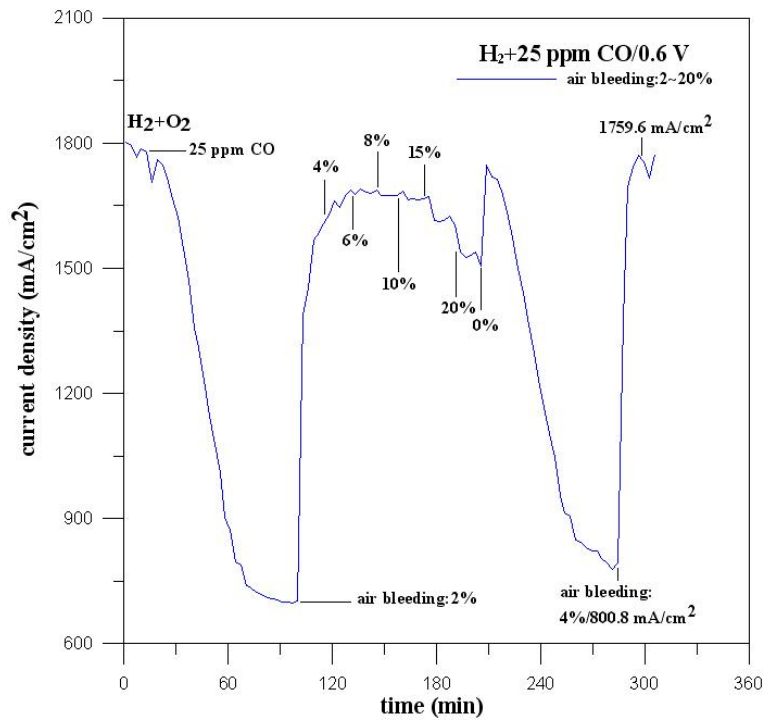


Fig. 4.2 Transient performance with continuously changing air ratio at 25 ppm

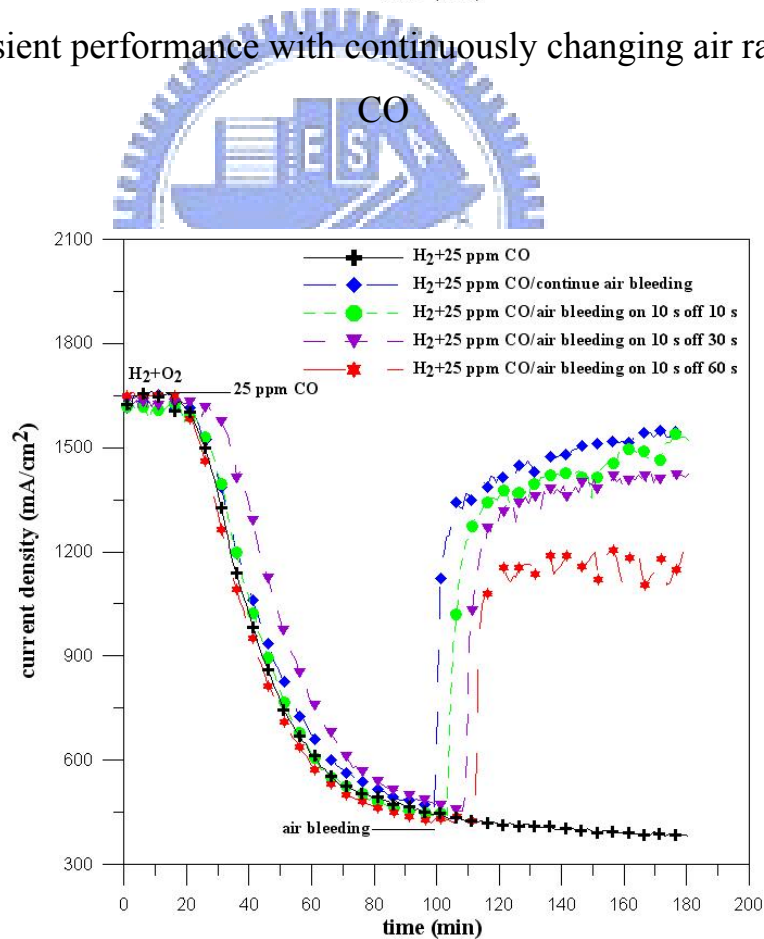


Fig. 4.3 Transient CO poisoning and recovery performance with different air bleeding frequencies (25 ppm CO)

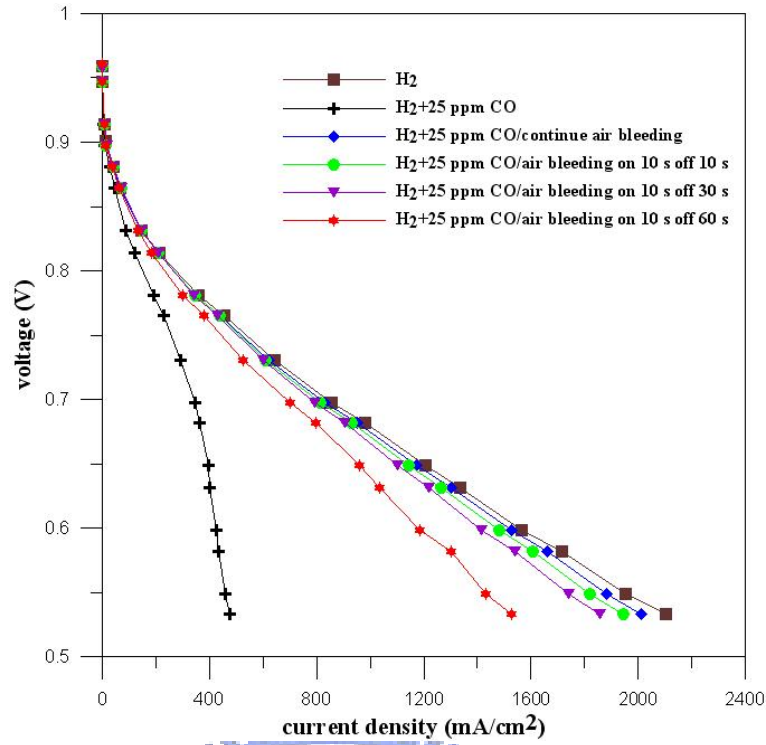


Fig. 4.4 Polarization curve with different air bleeding frequencies (25 ppm CO)

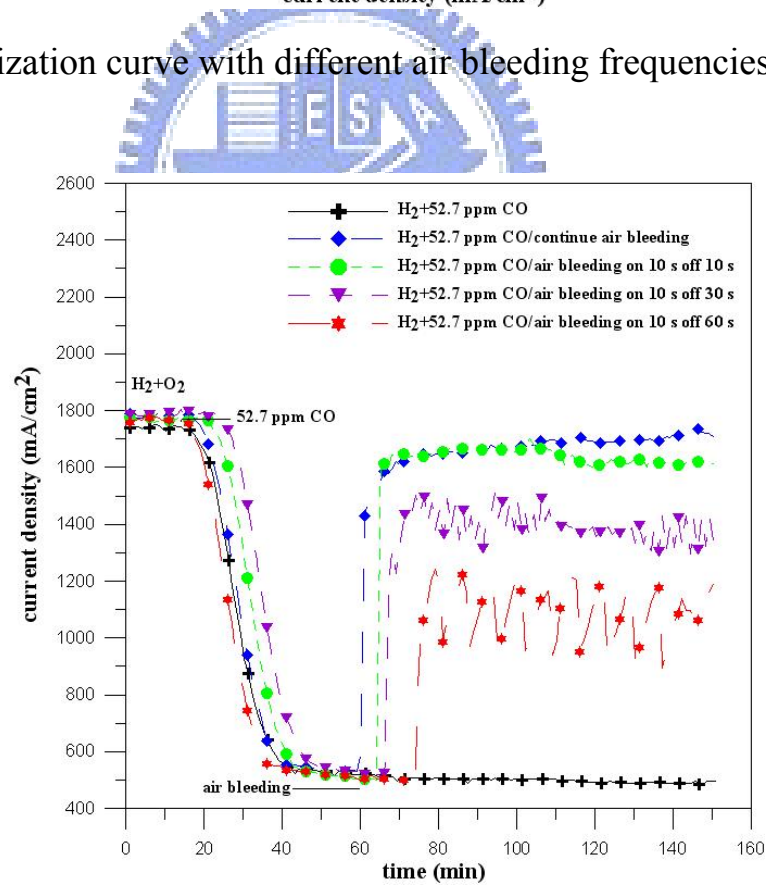


Fig. 4.5 Transient CO poisoning and recovery performance with different air bleeding frequencies (52.7 ppm CO)

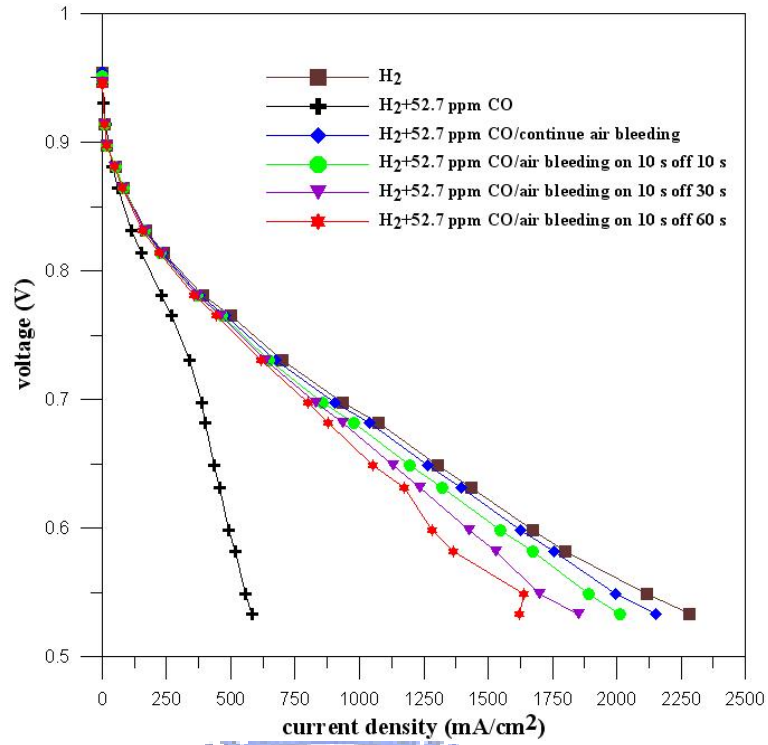


Fig. 4.6 Polarization curve with different air bleeding frequencies (52.7 ppm CO)

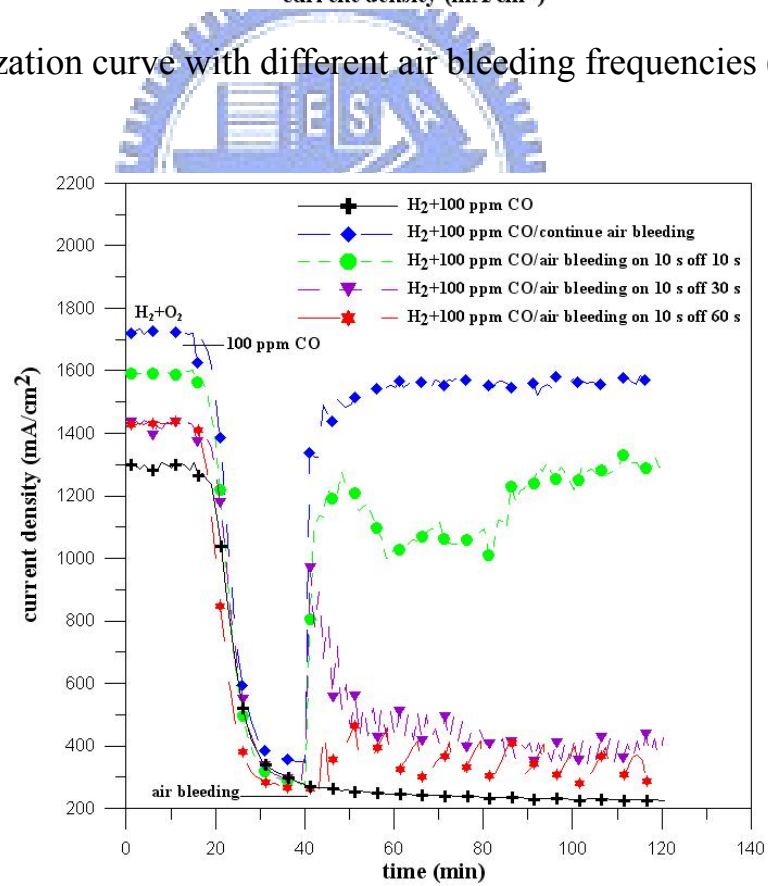


Fig. 4.7 Transient CO poisoning and recovery performance with different air bleeding frequencies (100 ppm CO)

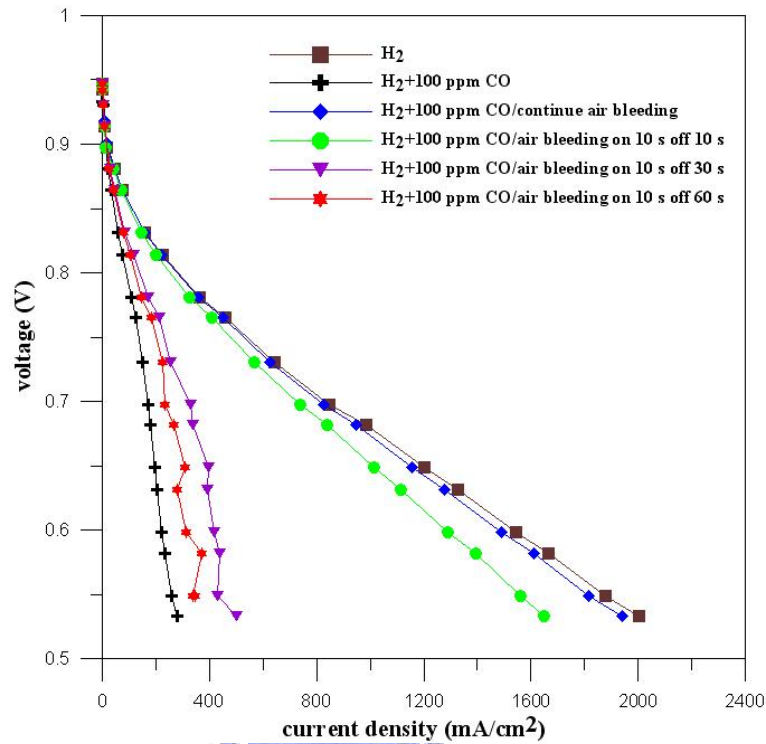


Fig. 4.8 Polarization curve with different air bleeding frequencies (100 ppm CO)

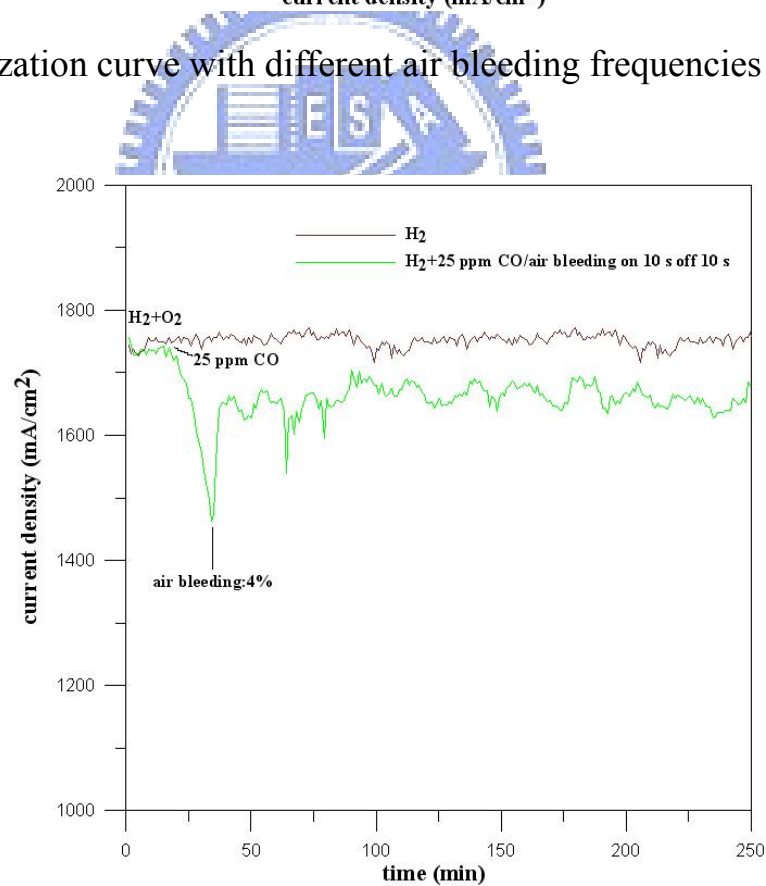


Fig. 4.9 Transient air bleeding long time test with CO poisoning concentrations (25 ppm), a dosing of air for 10 s in intervals of 10 s

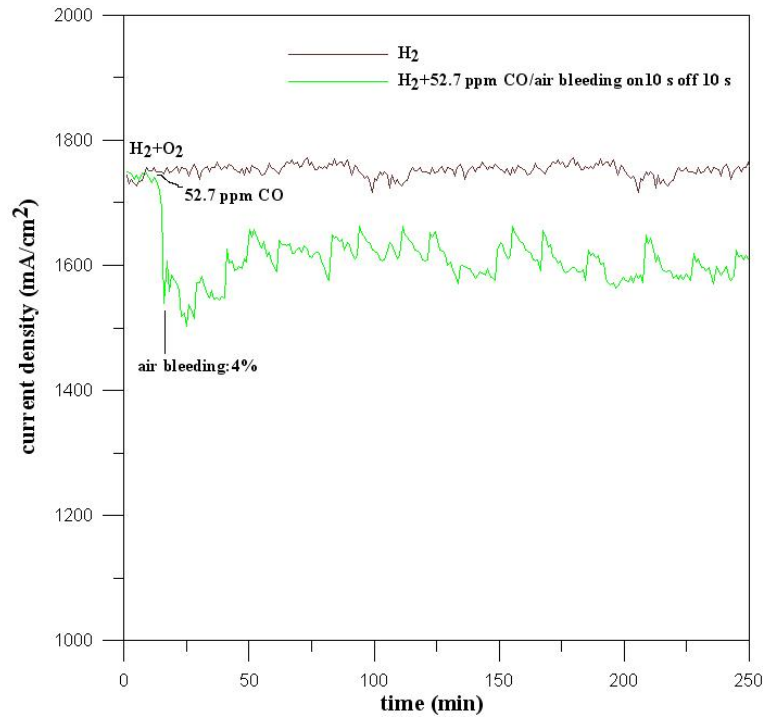


Fig. 4.10 Transient air bleeding long time test with CO poisoning concentrations (52.7 ppm), a dosing of air for 10 s in intervals of 10 s

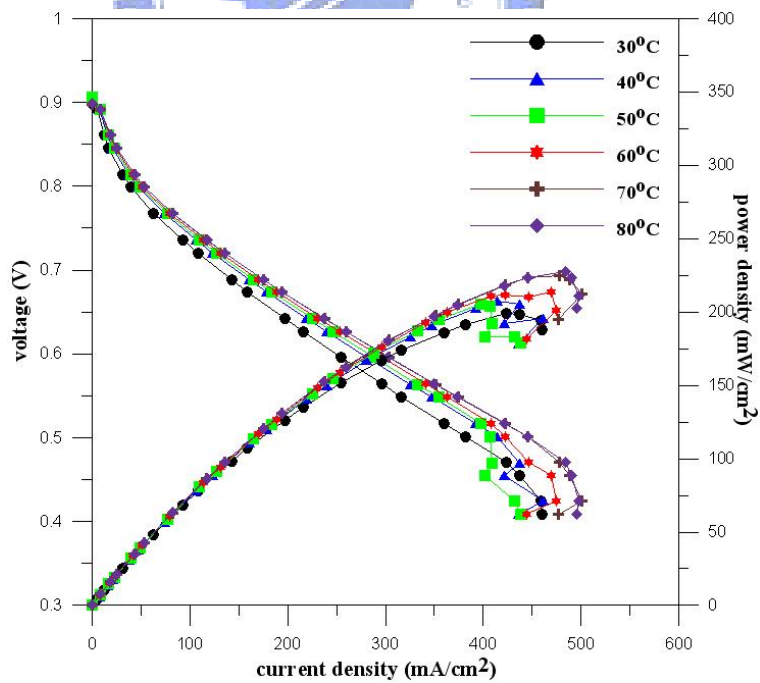


Fig. 4.11 Polarization curves of micro PEMFC at different fuel temperatures

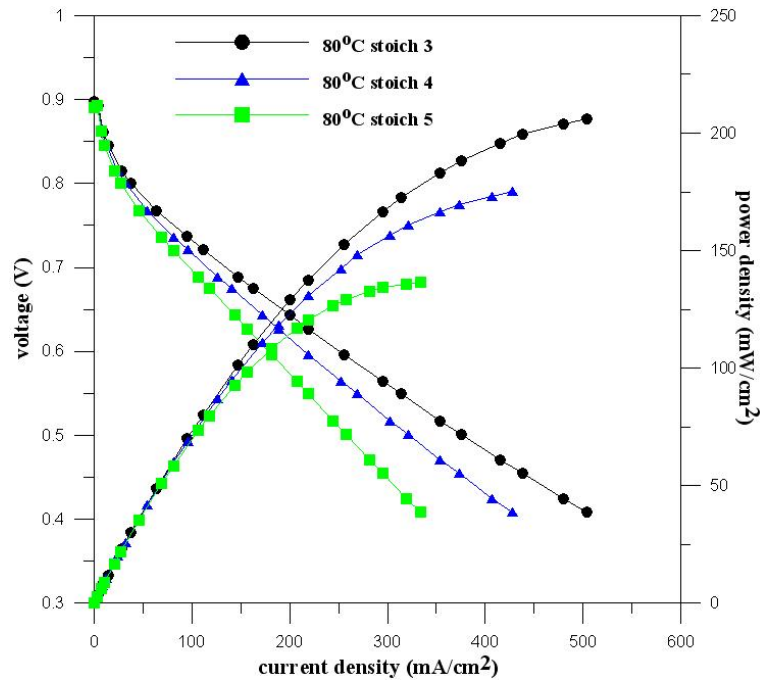


Fig. 4.12 Comparison of polarization curves at three operating fuel (H_2/O_2) flow rates at $80^\circ C$

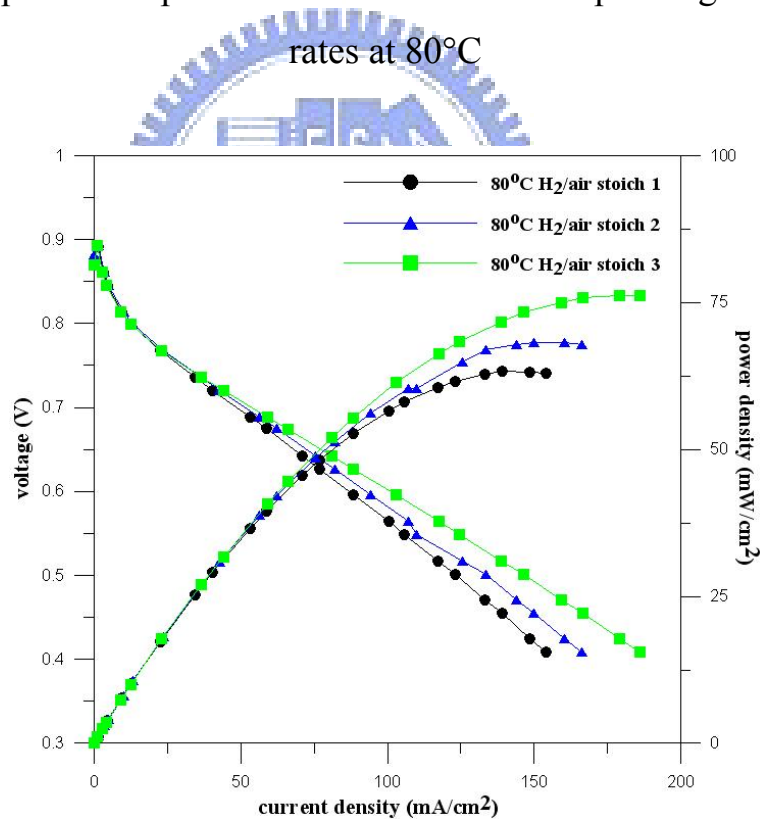


Fig. 4.13 Comparison of polarization curves at three operating fuel (H_2/air) flow rates at $80^\circ C$

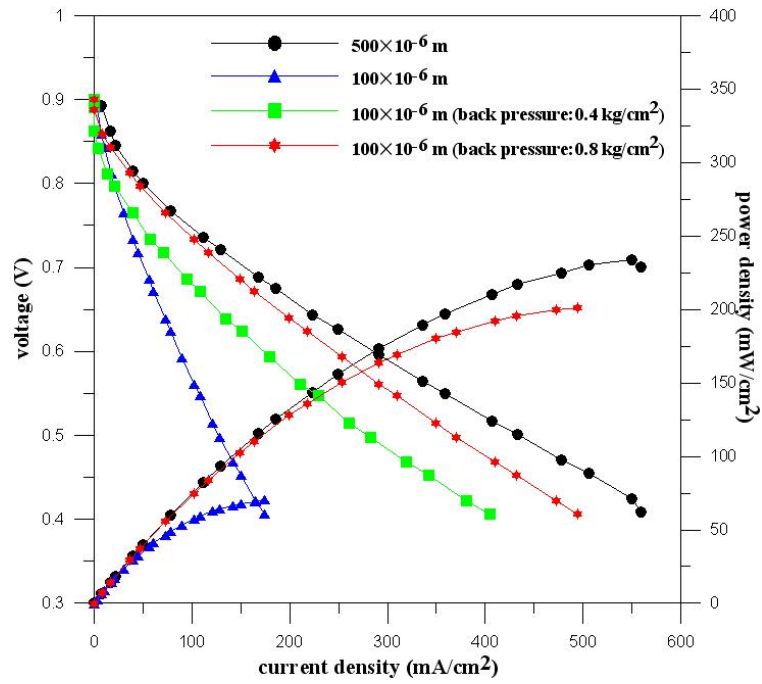


Fig. 4.14 Comparison of polarization curves at two different channel depths and employing back pressure in shallow channels

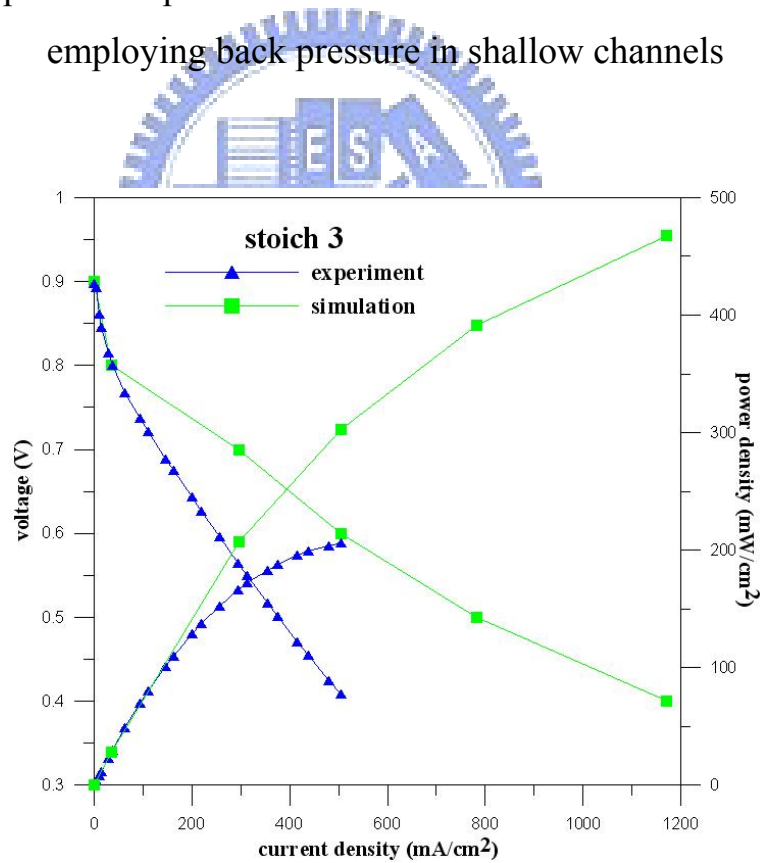


Fig. 4.15 Comparison of polarization curves with simulation and experiment (the flow rate of 3 times of reference flow rate)

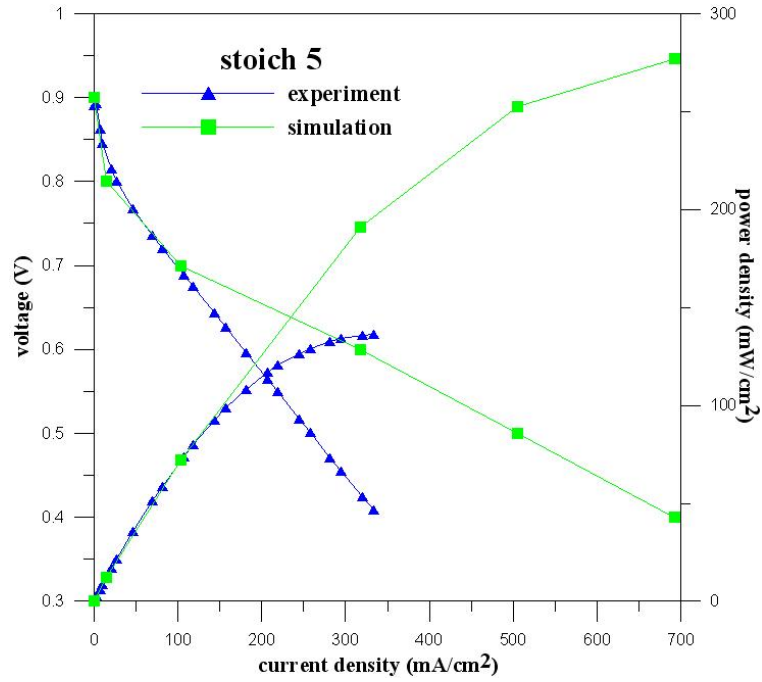


Fig. 4.16 Comparison of polarization curves with simulation and experiment (the flow rate of 5 times of reference flow rate)

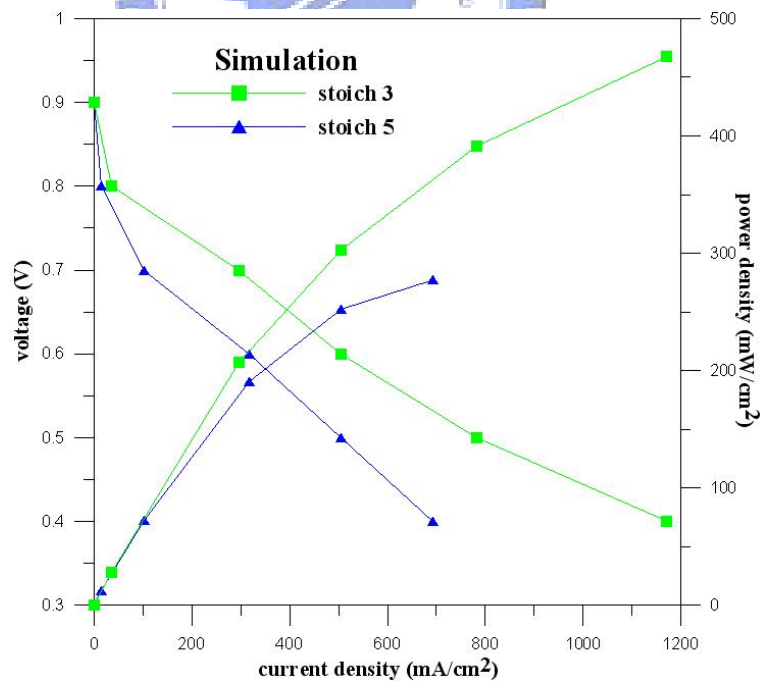


Fig. 4.17 Comparison of polarization curves at two different flow rates (simulation)

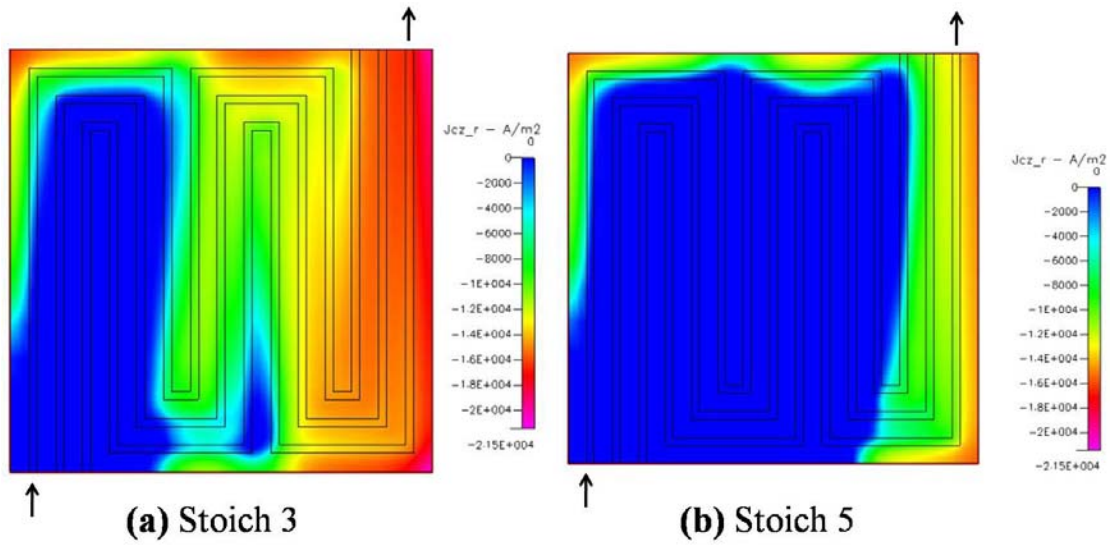


Fig. 4.18 Distributions of current density in the membrane at operation voltage 0.4 V: (a) the flow rate of 3 times of reference flow rate (b) the flow rate of 5 times of reference flow rate

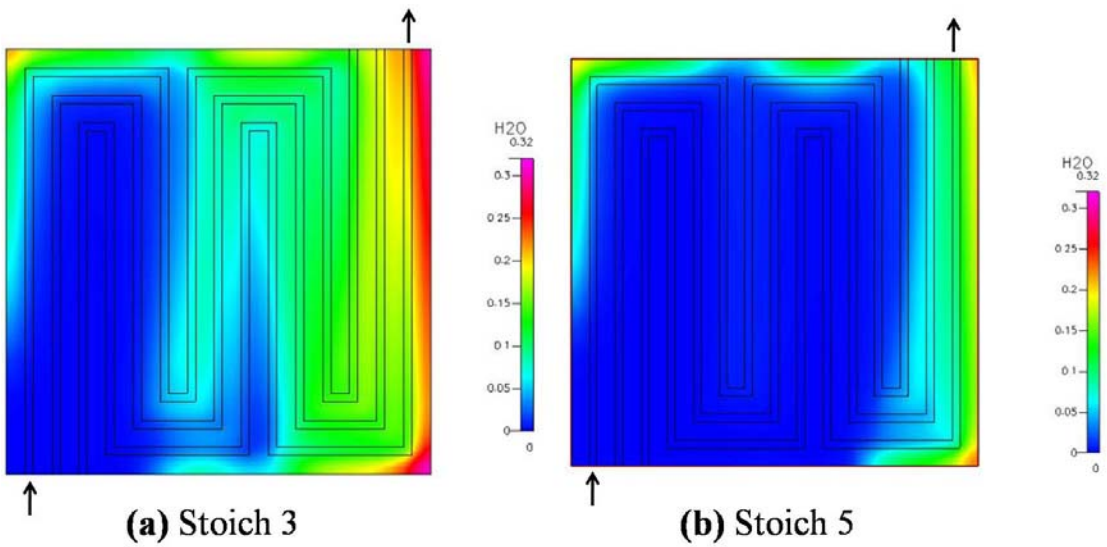
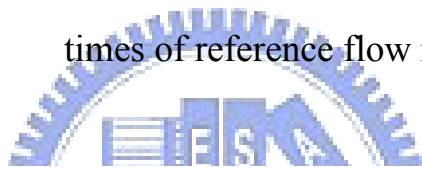


Fig. 4.19 Distributions of water in the membrane at operation voltage 0.4 V: (a) the flow rate of 3 times of reference flow rate (b) the flow rate of 5 times of reference flow rate

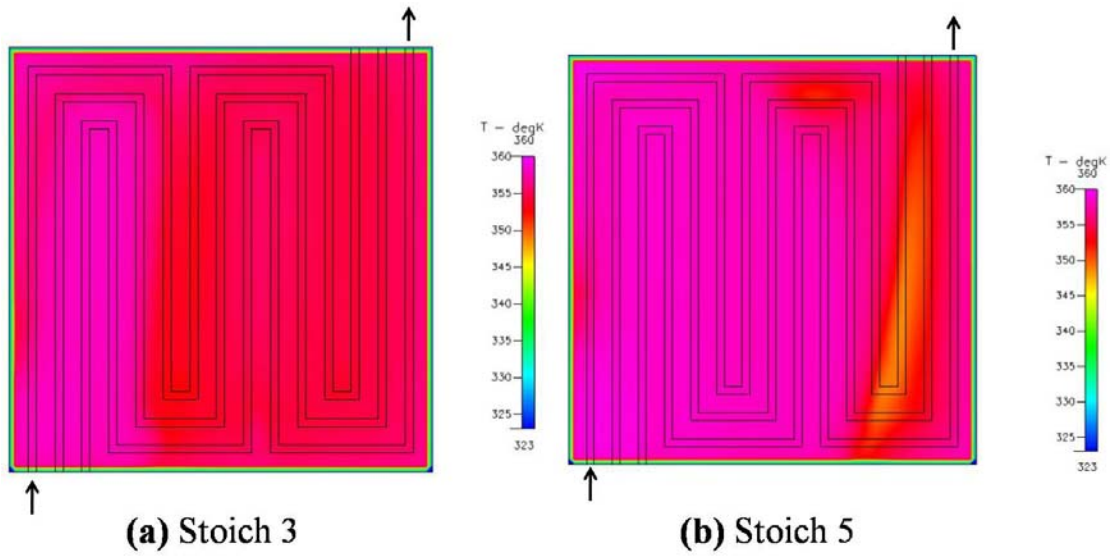


Fig. 4.20 Distributions of temperature in the membrane at operation voltage 0.4 V:

(a) the flow rate of 3 times of reference flow rate (b) the flow rate of 5 times of

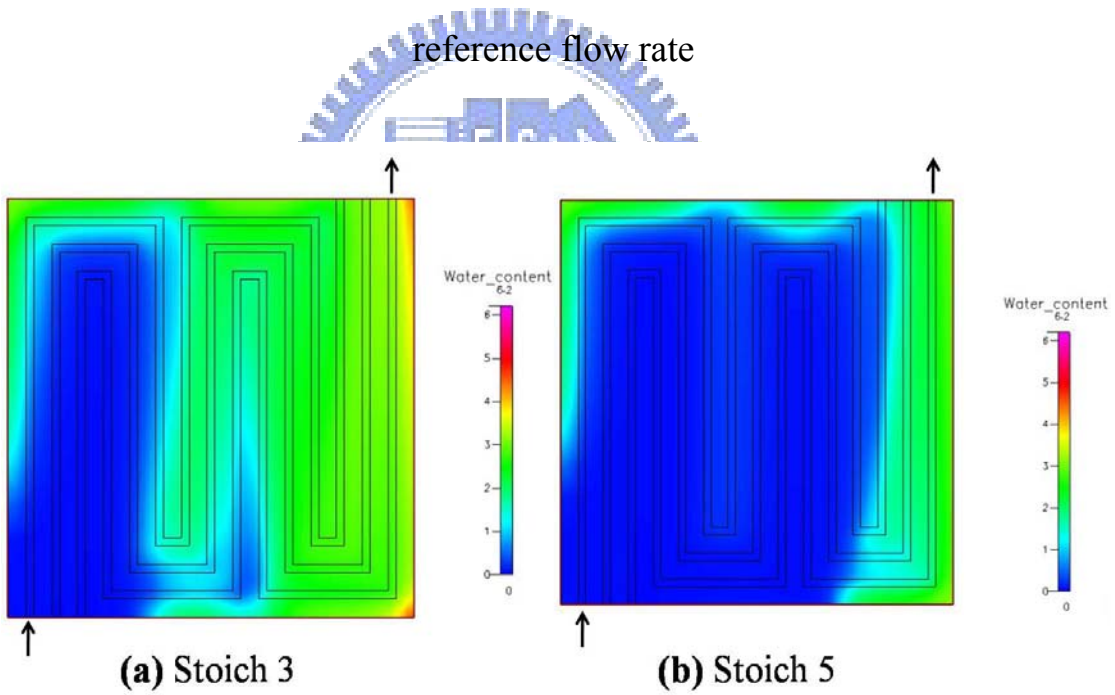


Fig. 4.21 Distributions of water content in the membrane at operation voltage 0.4

V: (a) the flow rate of 3 times of reference flow rate (b) the flow rate of 5 times of

reference flow rate

CHAPTER 5

CONCLUSIONS

The fluoride releasing rates are high when CO and air bleed are present together. Therefore, the dissertation investigates the effects of air bleeding with different frequencies in transient poisoning CO tests. With the continuous air bleeding applied to each CO concentration, the fuel cell can obtain the optimum CO tolerance. However, a dosing of air for 10 s in intervals of 10 s can also obtain effective CO tolerance. The injected O₂ is then more likely to be adsorbed on the surface of the catalyst, and the reaction rate of O₂ and CO is increased. The air bleeding frequency is a very important factor for the cell CO tolerance. A dosing of air for 10 s in intervals of 10 s is the optimum frequency of air bleeding and increases the cell performance recovery rate. In this situation, the injected O₂ has more chance to be adsorbed on the catalyst surface and then increase the reaction rate of O₂ and CO. Therefore, it costs a lower air bleeding ratio to get better CO tolerance performance by shorter air injection timing.

Portable consumer electronic devices require small, lightweight power supplies with high electricity capacity. Micro PEMFCs meet this requirement. The dissertation employs MEMS technology to etch flow field channels into a silicon substrate. The reaction area of this single micro PEMFC is 2.5 cm². A single micro PEMFC is successfully fabricated and favorable performance achieved. The micro PEMFC performance is validated with a three-dimensional mathematical model. The model simulates current density, water and temperature distributions at two different flow ratios. The simulation results show that the high current density distribution in the membrane at the flow rate of 3 times of reference flow rate, which can increase membrane water distribution,

perform uniform temperature distribution, and improve micro PEMFC performance.



REFERENCE

- [1] M. Watanabe, and S. Motoo, "Electrocatalysis by Ad-Atoms Part III. Enhancement of the Oxidation of Carbon Monoxide on Platinum by Ruthenium Ad-Atoms," *J. Electroanal. Chem.*, Vol. 60, pp. 275-283, 1975.
- [2] H. P. Dhar, L. G. Christner, A. K. Kush, and H. C. Maru, "Nature of CO Adsorption During H₂ Oxidation in Relation to Modeling for CO Poisoning of a Fuel Cell Anode," *J. Electrochem. Soc.*, Vol. 134, pp. 3021-3026, 1987.
- [3] H. A. Gastiger, N. Markovic, P. N. Ross Jr., and E. J. Cairns, "CO Electrooxidation on Well-Characterized Pt-Ru Alloys," *J. Phys. Chem.*, Vol. 98, pp. 617-625, 1994.
- [4] H. F. Oetjen, V. M. Schmidt, U. Stimming, and F. Trila, "Performance Data of a Proton Exchange Membrane Fuel Cell Using H₂/CO as Fuel Gas," *J. Electrochem. Soc.*, Vol. 143, pp. 3838-3842, 1996.
- [5] M. Watanabe, H. Igarashi, and T. Fujino, "Design of CO Tolerance Anode Catalysts for Polymer Electrolyte Fuel Cell," *Electrochim. Acta*, Vol. 67, pp. 1194-1196, 1999.
- [6] E. Christoffersen, P. Liu, A. Ruban, H. L. Skriver, and J. K. Nørskov, "Anode Materials for Low-Temperature Fuel Cells: A Density Functional Theory Study," *J. Catal.*, Vol. 199, pp. 123-131, 2001.
- [7] H. Yu, Z. Hou, B. Yi, and Z. Lin, "Composite Anode for CO Tolerance Proton Exchange Membrane Fuel Cells," *J. Power Sources*, Vol. 105, pp. 52-57, 2002.
- [8] D. C. Papageorgopoulos, M. P. de Heer, M. Keijzer, J. A. Z. Pieterse, and F. A. de Bruijn, "Nonalloyed Carbon-Supported PtRu Catalysts for PEMFC," *J. Electroanal. Chem.*, Vol. 151, pp. 763-768, 2004.

- [9] E. I. Santiago, M. S. Batista, E. M. Assaf, and E. A. Ticianelli, "Mechanism of CO Tolerance on Molybdenum-Based Electrocatalysts for PEMFC," *J. Electroanal. Chem.*, Vol. 151, pp. 944-949, 2004.
- [10] D. J. Ham, Y. K. Kim, S. H. Han, and J. S. Lee, "Pt/WC as an Anode Catalyst for PEMFC: Activity and CO Tolerance," *Catalyst Today*, Vol. 132, pp. 117-122, 2008.
- [11] S. Gottesfeld, and J. Pafford, "A New Approach to the Problem of Carbon Monoxide Poisoning in Fuel Cells Operating at Low Temperatures," *J. Electrochem. Soc.*, Vol. 135, pp. 2651-2652, 1988.
- [12] B. Rohland, and V. Plzak, "The PEMFC Integrated CO Oxidation-a Novel Method of Simplifying the Fuel Cell Plant," *J. Power Sources*, Vol. 84, pp. 183-186, 1999.
- [13] L. Gubler, G. G. Scherer, and A. Wokaun, "Effects of Cell and Electrode Design on the CO Tolerance of Polymer Electrolyte Fuel Cells," *Phys. Chem. Chem. Phys.*, Vol. 3, pp. 325-329, 2001.
- [14] A. T. Haug, R. E. White, J. W. Weidner, and W. Huang, "Development of a Novel CO Tolerant Proton Exchange Membrane Fuel Cell Anode," *J. Electrochem. Soc.*, Vol. 149, pp. 862-867, 2002.
- [15] A. T. Haug, R. E. White, J. W. Weidner, W. Huang, S. Shi, N. Rana, S. Grunow, and T. C. Stoner, "Using Sputter Deposition to Increase CO Tolerant in a Proton-Exchange Membrane Fuel Cell," *J. Electrochem. Soc.*, Vol. 149, pp. 868-872, 2002.
- [16] M. Murthy, M. Esayan, W. k. Lee, and J. W. Van Zee, "The Effect of Temperature and Pressure on the Performance of a PEMFC Exposed to Transient CO Concentrations," *J. Electrochem. Soc.*, Vol. 150, pp. 29-34, 2003.

- [17] J. J. Baschuk, and X. K. Li, "Modelling CO Poisoning and O₂ Bleeding in a PEM Fuel Cell Anode," *Int. J. Energ. Res.*, Vol. 27, pp. 1095-1116, 2003.
- [18] W. K. Lee, J. W. Van Zee, and M. Murthy, "A Method for Characterizing CO Transients in a PEMFC," *Fuel Cells*, Vol. 3, pp. 52-58, 2003.
- [19] F. A. Uribe, J. A. Valerio, F. H. Garzon, and T. A. Zawodzinski, "PEMFC Reconfigured Anodes for Enhancing CO Tolerance with Air Bleed," *Electrochem. Solid-State Lett.*, Vol. 7, pp. 376-379, 2004.
- [20] W. Y. Shi, M. Hou, Z. A. Shao, J. Hu, Z. J. Hou, P. W. Ming, and B. L. Yi, "A Novel Proton Exchange Membrane Fuel Cell Anode for Enhancing CO Tolerance," *J. Power Sources*, Vol. 174, pp. 164-169, 2007 .
- [21] H. S. Chu, F. Tsau, Y. Y. Yan, K. L. Hsueh, and F. L. Chen, "The Development of a Small PEMFC Combined Heat and Power System," *J. Power Sources*, Vol. 176, pp. 499-514, 2008.
- [22] W. Vielstich, A. Lamm, and H. A. Gasteiger, *Handbook of Fuel Cells*, Vol. 1, West Sussex, England, 2003.
- [23] S. J. J. Lee, S. W. Cha, Y. Liu, R. O'Hayre, and F. B. Prinz, "High Power-Density Polymer-Electrolyte Fuel Cells by Microfabrication," *Electrochemical Society Proceedings*, Spring 2000.
- [24] S. C. Kelley, G. A. Deluga, and W. H. Smyrl, "A Miniature Methanol/Air Polymer Electrolyte Fuel Cell," *Electrochem. Solid-State Lett.*, Vol. 3, pp. 407-409, 2000.
- [25] J. P. Meyers, and H. L. Maynard, "Design Considerations for Miniaturized PEM Fuel Cells," *J. Power Sources*, Vol. 109, pp. 76-88, 2002.
- [26] M. Muller, C. Muller, F. Gromball, M. Wolfle, and W. Menz, "Micro-Structured Flow Fields for Small Fuel Cells," *Microsystem Technologies*, Vol. 9, pp. 159-162, 2003.

- [27] R. O'Hayre, D. Braithwaite, W. Hermann, S. J. Lee, T. Fabian, S. W. Cha, Y. Saito, and F. B. Prinz, "Development of Portable Fuel Cell Arrays with Printed-Circuit Technology," *J. Power Sources*, Vol. 124, pp. 459-472, 2003.
- [28] R. Hahn, S. Wagner, A. Schmitz, and H. Reichl, "Development of a Planar Micro Fuel Cell with Thin Film and Micro Patterning Technologies," *J. Power Sources*, Vol. 131, pp. 73-78, 2004.
- [29] Y. Yohtaro, "Application of MEMS Technology to Micro Fuel Cells," *Electrochim. Acta*, Vol. 50, pp. 663-666, 2004.
- [30] S. S. Hsieh, J. K. Kuo, C. F. Hwang, and H. H. Tsai, "A Novel Design and Microfabrication for a Micro PEMFC," *Microsystem Technologies*, Vol. 10, pp. 121-126, 2004.
- [31] A. Schmitz, S. Wagner, R. Hahn, H. Uzun, and C. Hebling, "Stability of Planar PEMFC in Printed Circuit Board Technology," *J. Power Sources*, Vol. 127, pp. 197-205, 2004.
- [32] G. Q. Lu, C. Y. Wang, T. J. Yen, and X. Zhang, "Development and Characterization of a Silicon-Based Micro Direct Methanol Fuel Cell," *Electrochim. Acta*, Vol. 49, pp. 821-828, 2004.
- [33] H. Y. Cha, H. G. Choi, J. D. Nam, Y. K. Lee, S. M. Cho, E. S. Lee, J. K. Lee, and C. H. Chung, "Fabrication of All-Polymer Micro-DMFCs using UV-Sensitive Photoresist," *Electrochim. Acta*, Vol. 50, pp. 795-799, 2004.
- [34] R. Luharuka, C. F. Wu, and P. J. Hesketh, "Design, Fabrication, and Testing of a Near Constant Pressure Fuel Delivery System for Miniature Fuel Cells," *Sensors and Actuators*, Vol. 112, pp. 187-195, 2004.
- [35] S. S. Hsieh, C. F. Hwang, J. K. Kuo, H. H. Tsai, and S. H. Yang, "SU-8 Flow Field Plates for a Micro PEMFC," *J. Electrochem. Soc.*, Vol. 9, pp.

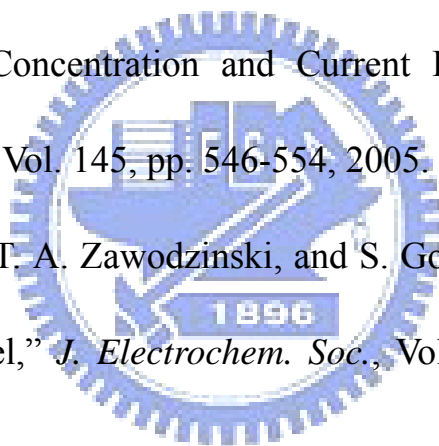
- 121-131, 2005.
- [36] S. H. Chan, N. T. Nguyen, Z. Xia, and Z. Wu, "Development of a Polymeric Micro Fuel Cell Containing Laser-Micromachined Flow Channels," *J. Micromech. Microeng.*, Vol. 161, pp. 138-142, 2005.
- [37] G. Lu, and C. Y. Wang, "Development of High Performance Micro DMFCs and a DMFC Stack," Third International Conference on Fuel Cell Science, Engineering and Technology, 2005.
- [38] S. Aravamudhan, A. R. A. Rahman, and S. Bhansali, "Porous Silicon Based Orientation Independent, Self-Priming Micro Direct Ethanol Fuel Cell," *Sensors and Actuators*, Vol. 123-124, pp. 497-504, 2005.
- [39] R. S. Jayashree, L. Ganes, E. R. Choban, A. Primak, D. Natarajan, L. J. Markoski, and P. J. A. Kenis, "Air-Breathing Laminar Flow-Based Microfluidic Fuel Cell," *Journal American Chemical Society*, Vol. 127, pp. 16758-16759, 2005.
- [40] S. W. Cha, R. O'Hayre, Y. I. Park, and F. B. Prinz, "Electrochemical Impedance Investigation of Flooding in Micro-Flow Channels for Proton Exchange Membrane Fuel Cells," *J. Power Sources*, Vol. 161, pp. 138-142, 2006.
- [41] J. Y. Kim, O. J. Kwon, S. M. Hwang, M. S. Kang, and J. J. Kim, "Development of a Miniaturized Polymer Electrolyte Membrane Fuel Cell with Silicon Separators," *J. Power Sources*, Vol. 161, pp. 432-436, 2006.
- [42] S. S. Hsieh, S. H. Yang, and C. L. Feng, "Characterization of the Operational Parameters of a H₂/Air Micro PEMFC with Different Flow Fields by Impedance Spectroscopy," *J. Power Sources*, Vol. 162, pp. 262-270, 2006.
- [43] S. S. Hsieh, C. L. Feng, and C. F. Huang, "Development and Performance

- Analysis of a H₂/Air Micro PEM fuel cell stack,” *J. Power Sources*, Vol. 163, pp. 440-449, 2006.
- [44] Z. Xiao, G. Yan, C. Feng, P. C. H. Chan, and I. M. Hsing, “A Silicon-Based Fuel Cell Micro Power System Using a Micro fabrication Technique,” *J. Micromech. Microeng.*, Vol. 16, pp. 2014-2020, 2006.
- [45] X. Yang, Z. Y. Zhou, H. J. Cho, and X. B. Luo, “Study on a PZT-Actuated Diaphragm Pump for Air Supply for Micro Fuel Cells,” *Sensors and Actuators*, Vol. 130-131, pp. 531-536, 2006.
- [46] S. C. Yao, X. Tang, C. C. Hsieh, Y. Alyousef, M. Vladimer, G. K. Fedder, and C. H. Amon, “Micro-Electro-Mechanical Systems (MEMS)-Based Micro-Scale Direct Methanol Fuel Cell Development,” *Energy*, Vol. 31, pp. 636-649, 2006.
- [47] T. Ito, K. Kimura, and M. Kunimatsu, “Characteristics of Micro DMFCs Array Fabricated on Flexible Polymeric Substrate,” *Electrochem. Commun.*, Vol. 8, pp. 973-976, 2006.
- [48] S. W. Lim, S. W. Kim, H. J. Kim, J. E. Ahn, H. S. Han, and Y. G. Shul, “Effect of Operation Parameters on Performance of Micro Direct Methanol Fuel Cell Fabricated on Printed Circuit Board,” *J. Power Sources*, Vol. 161, pp. 27-33, 2006.
- [49] N. T. Nguyen, and S. H. Chan, “Micromachined Polymer Electrolyte Membrane and Direct Methanol Fuel Cells-a Review,” *J. Micromech. Microeng.*, Vol. 16, pp. R1-R12, 2006.
- [50] C. Y. Lee, and C. W. Chuang, “A Novel Integration Approach for Combining the Components to Minimize a Micro-Fuel Cell,” *J. Power Sources*, Vol. 172, pp. 115-120, 2007.
- [51] C. Feng, P. C. H. Chan, and I. M. Hsing, “Catalyzed Microelectrode

- Mediated by Polypyrrole/Nafion Composite Film for Microfabricated Fuel Cell Applications,” *Electrochem. Commun.*, Vol. 9, pp. 89-93, 2007.
- [52] B. C. Seyfang, M. Kuhnke, T. Lippert, G. G. Scherer, and A. Wokaum, “A novel, Simplified Micro-PEFC Concept Employing Glassy Carbon Micro-Structures,” *Electrochem. Commun.*, Vol. 9, pp. 1958-1962, 2007.
- [53] M. Koc, and S. Mahabunphachai, “Feasibility Investigations on a Novel Micro-Manufacturing Process for Fabrication of Fuel Cell Bipolar Plates: Internal Pressure-Assisted Embossing of Micro- Channels with in-Die Mechanical Bonding,” *J. Power Sources*, Vol. 172, pp. 725-733, 2007.
- [54] S. S. Hsieh, and K. M. Chu, “Channel and Rib Geometric Scale Effects of Flowfield Plates on the Performance and Transient Thermal Behavior of a Micro-PEM Fuel Cell,” *J. Power Sources*, Vol. 173, pp. 222-232, 2007.
- [55] F. Y. Zhang, S. G. Advani, and A. K. Prasad, “Performance of a Metallic Gas Diffusion Layer for PEM Fuel Cells,” *J. Power Sources*, Vol. 176, pp. 293-298, 2008.
- [56] L. Renaud, C. Malhaire, P. Kleimann, D. Barbier, and P. Morin, “Theoretical and Experimental Studies of Microflows in Silicon Microchannels,” *Materials Science and Engineering C*, Vol. 28, pp. 910-917, 2008.
- [57] M. S. Chiang, and H. S. Chu, “Numerical Investigation of Transport Component Design Effect on a Proton Exchange Membrane Fuel Cell,” *J. Power Sources*, Vol. 160, pp. 340-352, 2006.
- [58] S. Shimpalee, and J. W. Van Zee, “Numerical Studies on Rib & Channel Dimension of Flow-Field on PEMFC Performance,” *Int. J. Hydrogen Energ.*, Vol. 33, pp. 842-856, 2007.
- [59] L. Matamoros, and D. Bruggemann, “Numerical Study on PEMFC’s Geometrical Parameters Under Different Humidifying Conditions,” *J.*

- Power Sources*, Vol. 172, pp. 253-264, 2007.
- [60] S. Shimpalee, S. Greenway, and J. W. Van Zee, "The Impact of Channel Length on PEMFC Flow-Field Design," *J. Power Sources*, Vol. 160, pp. 398-406, 2006.
- [61] X. Liu, W. Tao, Z. Li, and Y. He, "Three-Dimensional Transport Model of PEM Fuel Cell with Straight Flow Channels," *J. Power Sources*, Vol. 158, pp. 25-35, 2006.
- [62] R. W. Fox, and A. T. McDonald, "Introduction to Fluid Mechanics," John Wiley and Sons, Canada, 1994.
- [63] S. J. Kline, and F. A. McClintock, "Describing Uncertainties in Single-Sample Experiments," *Mech. Eng.*, Vol. 75, pp. 3-8, 1953.
- [64] S. Mazumder, and J. V. Cole, "Rigorous 3-D Mathematical Modeling of PEM Fuel Cells II Model Predictions with Liquid Water Transport," *J. Electrochem. Soc.*, Vol. 150 (11), pp. 1510-1517, 2003.
- [65] S. Kamarajugadda, and S. Mazumder, "On the Implementation of Membrane Models in Computational Fluid Dynamics Calculations of Polymer Electrolyte Membrane Fuel Cells," *Computers and Chemical Engineering*, Vol. 32, pp. 1650-1660, 2008.
- [66] D. M. Bernardi, and M. W. Verbrugge, "Mathematical Model of a Gas Diffusion Electrode Bonded to a Polymer Electrolyte," *AICHE J.*, Vol. 37, No. 8, pp. 1151-1163, 1991.
- [67] A. kumer, and R. G. Reddy, "Modeling of Polymer Electrolyte Membrane Fuel Cell with Metal form in the Flow-Field of the Bipolar/End Plates," *J. Power Sources*, Vol. 114, pp. 54-62, 2003.

- [68] W. Sun, B. A. Peppley, and K. Karan, "Modeling the Influence of GDL and Flow-Field Plate Parameters on the Reaction Distribution in the PEMFC Cathode Catalyst Layer," *J. Power Sources*, Vol. 144, pp. 42-53, 2005.
- [69] P. T. Nguyen, T. Berning, and N. Djilali, "Computational Model of a PEM Fuel Cell with Serpentine Gas Flow Channels," *J. Power Sources*, Vol. 130, pp. 149-157, 2004.
- [70] C. Y. Wang, "Fundamental Models for Fuel Cell Engineering," *Chem. Rev.*, Vol. 104, pp. 4727-4766, 2004.
- [71] F. B. Weng, A. Su, G. B. Jung, Y. C. Chiu, and S. H. Chan, "Numerical Prediction of Concentration and Current Distributions in PEMFC," *J. Power Sources*, Vol. 145, pp. 546-554, 2005.
- [72] T. E. Springer, T. A. Zawodzinski, and S. Gottesfeld, "Polymer Electrolyte Fuel Cell Model," *J. Electrochem. Soc.*, Vol. 138, No. 8, pp. 2334-2342, 1991.
- [73] H. Meng, and C. Y. Wang, "Electron Transport in PEFCs," *J. Electrochem. Soc.*, Vol. 151 (3), pp. A358-A367, 2004.



APPENDIX

PEMFC

The measuring uncertainty analysis of PEMFC voltage and current density are (U_v, U_I)

The minimum scale of measuring voltage in the apparatus=1 mV

The voltage of the largest power density $V=496$ mV

The measuring uncertainty analysis of voltage (U_v):

$$U_v = \pm \frac{0.5}{496} = \pm 0.001$$

The minimum scale of measuring current density in the apparatus=0.1 mA/cm²

The current density of the largest power density $I=1750.4$ mA/cm²

The measuring uncertainty analysis of current density (U_I):

$$U_I = \pm \frac{0.05}{1750.4} = \pm 0.00003$$

The measuring uncertainty analysis of fuel cell power density (U_p):

$$P=I \times V$$

$$U_p = \sqrt{(U_v)^2 + (U_I)^2}$$

$$U_p = \pm 0.001$$

Micro PEMFC

The measuring uncertainty analysis of micro PEMFC voltage and current density are (U_V, U_I)

The minimum scale of measuring voltage in the apparatus=1 mV

The voltage of the largest power density $V=347$ mV

The measuring uncertainty analysis of voltage (U_V):

$$U_v = \pm \frac{0.5}{347} = \pm 0.001$$

The minimum scale of measuring current density in the apparatus=0.1 mA/cm²

The current density of the largest power density $I=834.5$ mA/cm²

The measuring uncertainty analysis of current density (U_I):

$$U_I = \pm \frac{0.05}{834.5} = \pm 0.00005$$

The measuring uncertainty analysis of micro PEMFC power density (U_P):

$$P = I \times V$$

$$U_P = \sqrt{(U_V)^2 + (U_I)^2}$$

$$U_P = \pm 0.001$$

PUBLICATIONS

1. 直接甲醇自然進氣平板式燃料電池堆設計與性能分析，鍾振忠、鄭翔仁、邱彥樵、翁芳柏，第二十屆機械工程研討會，國立台灣大學，台灣，Dec. 5-6，2003.
2. PEMFC 三維質傳與電流密度數值分析，邱彥樵、鍾振忠、鄭翔仁、翁芳柏、蘇艾、詹世弘，中華民國第二十七屆全國力學會議，國立成功大學，台灣，Dec. 12-13，2003.
3. 直接甲醇平板式燃料電池堆設計與性能分析，鍾振忠、邱彥樵、鄭翔仁、杜承鑫、翁芳柏，中華民國第二十七屆全國力學會議，國立成功大學，台灣，Dec. 12-13，2003.
4. 四區域半透明質子交換膜燃料電池設計與性能分析，翁芳柏、鄭翔仁、鍾振忠、邱彥樵，中華民國第二十七屆全國力學會議，國立成功大學，台灣，Dec. 12-13，2003.
5. 直接甲醇平板式燃料電池堆，鍾振忠、翁芳柏、邱彥樵、鄭翔仁，2003年元智大學燃料電池中心研討會
6. PEMFC 氣體分佈與電流密度三維數值模擬分析，邱彥樵、鍾振忠、翁芳柏、蘇艾，2003年元智大學燃料電池中心研討會
7. 四區域質子交換膜燃料電池串並聯分析，鄭翔仁、鍾振忠、邱彥樵、翁芳柏，2003年元智大學燃料電池中心研討會

8. Design and Performance Analysis of Planar Direct Methanol Fuel Cell Stacks, Fang-Bor Weng, Chen-Chung Chung, Cheng-Hsin Tu, and Xiang-Ren Zheng, First International Conference on Fuel Cell Development and Deployment, Connecticut, U.S.A., Mar. 7-10, 2004.
9. Effect of Operating Parameters on the DMFC Performance and Methanol Crossover, Cheng-Hsin Tu, Ay Su, Guo-Bin Jung, and Chen-Chung Chung, First International Conference on Fuel Cell Development and Deployment, Connecticut, U.S.A., Mar. 7-10, 2004.
10. Design and Analysis of Four Segmented Semi-Opaque Proton Exchange Membrane Fuel Cells, Fang-Bor Weng, Hsiang-Jen Cheng, Chen-Chung Chung, Ay Su, and Yur-Tsai Lin, First International Conference on Fuel Cell Development and Deployment, Connecticut, U.S.A., Mar. 7-10, 2004.
11. Improvement of CO Tolerance of Proton Exchange Membrane Fuel Cell (PEMFC) by an Air-Bleeding Technique, Chen-Chung Chung, Chiun-Hsun Chen, Hsiang-Hui Lin, and Yi-Yie Yan, Proceedings of FUELCELL2005 The 3rd International Conference on Fuel Cell Science, Engineering and Technology, Ypsilanti Marriott Hotel at Eagle Crest-Ypsilanti, MI, May 23-25, 2005.
12. 二氧化碳對質子交換膜燃料電池性能的影響，陳俊勳、鍾振忠、顏貽乙、林祥輝、宋隆裕，第二十二屆機械工程研討會，國立中央大學，台灣，Nov. 25-26，2005
13. Design and Performance Analysis of Innovative Bipolar Direct Methanol Fuel Cell Stacks with 2D Planar Configuration, Guo-Bin Jung, Fang-Bor Weng, Ay Su, Chen-Chung Chung, Cheng-Hsin Tu, and Shih-Hun Chan, Journal of Fuel Cell Science and Technology, Vol. 3, No. 1, pp. 8-12, 2006.

14. Investigation of Cell Operation Conditions for CO Tolerance Improvement of PEMFC, Chen-Chung Chung, Chiun-Hsun Chen, Der-Cheng Weng, Yi-Yie Yan, and Hsiang-Hui Lin, Journal of the Chinese Society of Mechanical Engineers, Vol. 28, No. 6, pp. 563-569, 2007.
15. Improvement of CO Tolerance of Proton Exchange Membrane Fuel Cell by an Air-Bleeding Technique, Chen-Chung Chung, Chiun-Hsun Chen, Hsiang-Hui Lin, and Yi-Yie Yan, Journal of Fuel Cell Science and Technology, Vol. 5, pp. 014501-1-014501-5, 2008.
16. Development of an Air Bleeding Technique and Specific Duration to Improve the CO Tolerance of Proton-Exchange Membrane Fuel Cells, Chen-Chung Chung, Chiun-Hsun Chen, and De-Zheng Weng, Applied Thermal Engineering, Vol. 29, pp. 2518-2526, 2009.
17. Enhancement of Proton Exchange Membrane Fuel Cell Performance Using a Novel Tapered Gas Channel, Chen-Chung Chung, Chiun-Hsun Chen, and Ping-Ji Zhuang, Chinese Journal of Chemical Engineering, Vol. 17, No. 2, pp. 286-297, 2009.
18. Design and Performance Analysis of Micro Proton Exchange Membrane Fuel Cells, Chen-Chung Chung, Chiun-Hsun Chen, and Rong-Gui Peng, Chinese Journal of Chemical Engineering Vol. 17, No. 2, pp. 298-303, 2009.

VITA

姓名：鍾振忠 學號：9314815 性別：男

出生日期：67年11月23日

博士班資格考通過日期：97年1月29日

博士班論文口試日期：98年5月13日

論文指導教授：陳俊勳 教授

論文名稱：(中文)以週期性的空氣吹離法改善燃料電池一氧化碳毒化容忍

度與微型燃料電池設計與性能分析

(英文)Improvement of CO Tolerance of PEMFC by Periodic Air

Bleeding Technique & Design and Performance Analysis of
micro PEMFC

學歷：

91年6月，私立中華大學學士

93年6月，私立元智大學碩士

98年5月，國立交通大學博士

